



# **NAVAL POSTGRADUATE SCHOOL**

**MONTEREY, CALIFORNIA**

## **THESIS**

**WIRELESSLY NETWORKED DIGITAL PHASED ARRAY:  
DESIGN AND ANALYSIS OF A 2.4 GHZ DEMONSTRATOR**

by

Gert Burgstaller

September 2006

Thesis Advisors:

David Jenn  
Clark Robertson  
Richard Adler

**Approved for public release; distribution is unlimited**

THIS PAGE INTENTIONALLY LEFT BLANK

<b>REPORT DOCUMENTATION PAGE</b>			<i>Form Approved OMB No. 0704-0188</i>	
Public reporting burden for this collection of information is estimated to average 1 hour per response, including the time for reviewing instruction, searching existing data sources, gathering and maintaining the data needed, and completing and reviewing the collection of information. Send comments regarding this burden estimate or any other aspect of this collection of information, including suggestions for reducing this burden, to Washington headquarters Services, Directorate for Information Operations and Reports, 1215 Jefferson Davis Highway, Suite 1204, Arlington, VA 22202-4302, and to the Office of Management and Budget, Paperwork Reduction Project (0704-0188) Washington DC 20503.				
<b>1. AGENCY USE ONLY (Leave blank)</b>		<b>2. REPORT DATE</b> September 2006	<b>3. REPORT TYPE AND DATES COVERED</b> Master's Thesis	
<b>4. TITLE AND SUBTITLE:</b> Wirelessly Networked Digital Phased Array: Design and Analysis of a 2.4 GHz Demonstrator			<b>5. FUNDING NUMBERS</b>	
<b>6. AUTHOR(S)</b> Gert Burgstaller				
<b>7. PERFORMING ORGANIZATION NAME(S) AND ADDRESS(ES)</b> Naval Postgraduate School Monterey, CA 93943-5000			<b>8. PERFORMING ORGANIZATION REPORT NUMBER</b>	
<b>9. SPONSORING /MONITORING AGENCY NAME(S) AND ADDRESS(ES)</b> N/A			<b>10. SPONSORING/MONITORING AGENCY REPORT NUMBER</b>	
<b>11. SUPPLEMENTARY NOTES</b> The views expressed in this thesis are those of the author and do not reflect the official policy or position of the Department of Defense or the U.S. Government.				
<b>12a. DISTRIBUTION / AVAILABILITY STATEMENT</b> Approved for public release; distribution is unlimited			<b>12b. DISTRIBUTION CODE</b>	
<b>13. ABSTRACT (maximum 200 words)</b> <p>The wirelessly networked opportunistic digital array radar (WNODAR) system combines opportunistic phased array and aperstructure concepts. The array elements contain stand-alone transmit-receive (T/R) modules with no hardwire connections other than prime power and are wirelessly networked to a central controller and processor unit. A full-scale WNODAR operating in the VHF/UHF frequency bands (300 MHz) exhibits many favorable properties, which make the system suitable for ballistic missile defense (BMD) early warning radar (EWR) applications.</p> <p>In order to validate the WNODAR concepts, demonstration arrays consisting of T/R modules realized using field programmable gate array (FPGA) technology are developed. The demonstration units are frequency scaled from the projected VHF/UHF frequency range to S-band (2.4 GHz) to make use of the abundance of commercial off the shelf (COTS) wireless communication components.</p> <p>This research primarily relates to the development of a demonstration T/R module and the evaluation and characterization of component devices. Design, analysis and simulation of an eight-element demonstration array using MATLAB and CST Microwave Studio were conducted to examine expected array beam patterns.</p>				
<b>14. SUBJECT TERMS</b> Phased Array, Opportunistic Phased Array, Aperstructure, Radar, Transmitter, Receiver, COTS, Quadrature Modulator, Quadrature Demodulator, T/R Module, Demonstration Array			<b>15. NUMBER OF PAGES</b> 128	
			<b>16. PRICE CODE</b>	
<b>17. SECURITY CLASSIFICATION OF REPORT</b> Unclassified	<b>18. SECURITY CLASSIFICATION OF THIS PAGE</b> Unclassified	<b>19. SECURITY CLASSIFICATION OF ABSTRACT</b> Unclassified	<b>20. LIMITATION OF ABSTRACT</b> UL	

THIS PAGE INTENTIONALLY LEFT BLANK

**Approved for public release; distribution is unlimited.**

**WIRELESSLY NETWORKED DIGITAL PHASED ARRAY:  
DESIGN AND ANALYSIS OF A 2.4 GHZ DEMONSTRATOR**

Gert M. Burgstaller  
Commander, Swedish Armed Forces (Navy)  
M.S.E.E., Chalmers University of Technology, 1996

Submitted in partial fulfillment of the  
requirements for the combined degrees of

**MASTER OF SCIENCE IN ELECTRICAL ENGINEERING  
and  
ELECTRICAL ENGINEER**

from the

**NAVAL POSTGRADUATE SCHOOL  
September 2006**

Author: Gert Burgstaller

Approved by: David Jenn  
Thesis Advisor

Clark Robertson  
Thesis Advisor

Richard Adler  
Thesis Advisor

Jeffrey B. Knorr  
Chairman, Department of Electrical and Computer Engineering

THIS PAGE INTENTIONALLY LEFT BLANK

## **ABSTRACT**

The wirelessly networked opportunistic digital array radar (WNODAR) system combines opportunistic phased array and aperiodic structure concepts. The array elements contain stand-alone transmit-receive (T/R) modules with no hardwire connections other than prime power and are wirelessly networked to a central controller and processor unit. A full-scale WNODAR operating in the VHF/UHF frequency bands (300 MHz) exhibits many favorable properties, which make the system suitable for ballistic missile defense (BMD) early warning radar (EWR) applications.

In order to validate the WNODAR concepts, demonstration arrays consisting of T/R modules realized using field programmable gate array (FPGA) technology are developed. The demonstration units are frequency scaled from the projected VHF/UHF frequency range to S-band (2.4 GHz) to make use of the abundance of commercial off the shelf (COTS) wireless communication components.

This research primarily relates to the development of a demonstration T/R module and the evaluation and characterization of component devices. Design, analysis and simulation of an eight-element demonstration array using MATLAB and CST Microwave Studio were conducted to examine expected array beam patterns.

THIS PAGE INTENTIONALLY LEFT BLANK



## TABLE OF CONTENTS

<b>I.</b>	<b>INTRODUCTION.....</b>	<b>1</b>
A.	NATIONAL MISSILE DEFENSE.....	1
B.	THESIS MOTIVATION.....	2
C.	PREVIOUS WORK.....	7
D.	THESIS OBJECTIVE.....	8
E.	THESIS ORGANIZATION.....	9
<b>II.</b>	<b>SYSTEM LEVEL ARCHITECTURE OF THE WNODAR.....</b>	<b>11</b>
A.	WIRELESSLY NETWORKED OPPORTUNISTIC DIGITAL ARRAY RADAR.....	12
1.	Wireless Network.....	13
2.	Opportunistic Arrays.....	13
3.	Digital Antenna Arrays.....	14
B.	TRANSMIT/RECEIVE (T/R) MODULE.....	15
1.	LO Wireless Distribution.....	16
2.	LO Synchronization.....	16
3.	Element Geolocation.....	18
4.	Wireless Transmission Rates.....	18
5.	Further Challenges to be Addressed.....	20
C.	OTHER APPLICATIONS.....	21
1.	Military Applications.....	21
2.	Hastily Deployed Networks.....	22
3.	Commercial Applications.....	22
D.	SUMMARY.....	22
<b>III.</b>	<b>DESIGN CONSIDERATIONS FOR A DEMONSTRATION T/R MODULE....</b>	<b>23</b>
A.	PROPOSED SYSTEM LEVEL DEMONSTRATION DESIGN.....	23
B.	PROJECTED T/R MODULE COMPONENT LEVEL DESIGN.....	24
C.	MODULE COMPONENT CHARACTERIZATION.....	25
1.	LabVIEW.....	27
2.	FPGA Devices.....	27
3.	Modulator.....	29
4.	Low-Power Amplifier.....	38
5.	Circulator.....	43
6.	Dipole Antenna Element.....	47
7.	Low-Noise Amplifier.....	53
8.	Demodulator.....	58
9.	Voltage Controlled Oscillator.....	65
D.	SUMMARY.....	67
<b>IV.</b>	<b>DESIGN AND DEVELOPMENT OF A DEMONSTRATION ARRAY OPERATING AT 2.4 GHZ.....</b>	<b>69</b>
A.	PROPOSED SYSTEM LEVEL ARCHITECTURE.....	69

B.	DEMONSTRATION ARRAY DESIGN.....	70
1.	Demonstration T/R Module Mechanical Design.....	71
2.	Eight–element Array .....	74
3.	Initial Two-element Setup .....	77
C.	DEMONSTRATION ARRAY ANALYSIS.....	78
1.	Power Budget for Measurements .....	78
2.	Ground Plane Dimensions.....	85
D.	DEMONSTRATION ARRAY SIMULATIONS .....	86
1.	MATLAB Simulations.....	87
a.	<i>Element Factor</i> .....	87
b.	<i>Dipole over PEC</i> .....	88
c.	<i>Eight–element Array Factor</i> .....	88
d.	<i>Total Array Pattern</i> .....	89
e.	<i>MATLAB Coding and Plots</i> .....	90
2.	CST Microwave Studio Simulations .....	92
3.	Comparison MATLAB — CST MWS Simulations.....	93
E.	SUMMARY .....	95
V.	CONCLUSIONS AND RECOMMENDATIONS.....	97
A.	CONCLUSIONS .....	97
B.	RECOMMENDATIONS FOR FUTURE WORK.....	98
1.	Two–element Array .....	98
2.	Eight–element Array .....	98
3.	RF Leakage Cancellation .....	99
4.	Wireless LO and Data Distribution.....	99
APPENDIX A.	MATLAB SIMULATION PROGRAM.....	101
LIST OF REFERENCES	.....	103
INITIAL DISTRIBUTION LIST	.....	109

## LIST OF FIGURES

Figure 1.	Ballistic missile defense engagement sequence (From [4]).	3
Figure 2.	Two LPAR systems that constitute the UEWR components of the NMD (Courtesy of Boeing and Raytheon, respectively).	4
Figure 3.	Two classes of U.S. warships equipped with the radar system AN/SPY-1 (After [8]).	4
Figure 4.	Artist concept of the Zumwalt-class guided missile destroyer, DDG 1000 (Courtesy of Northrop Grumman).	5
Figure 5.	System level architecture for the WNODAR (After [20]).	12
Figure 6.	CAD model of Zumwalt-class sized ship with 1,200 randomly distributed integrated antenna elements (After [16]).	14
Figure 7.	Proposed system architecture of the T/R module (From [23]).	15
Figure 8.	Diagram of a synchronization circuit for one element (From [23]).	17
Figure 9.	Illustration of the brute force phase synchronization technique (After [23]).	17
Figure 10.	Proposed first phase airport network of the TINA project (From [25]).	19
Figure 11.	Block diagram of the final demonstration T/R module (From [23]).	23
Figure 12.	Simplified T/R module block diagram using hard-wired LO signal.	25
Figure 13.	Measured output power level of the VNA Port 1.	26
Figure 14.	Schematic model of the LabVIEW host interface.	28
Figure 15.	T/R module incorporated NI hardware (from [32]–[35]).	29
Figure 16.	AD8346EVAL wiring connections.	30
Figure 17.	Typical complex phasor plane.	30
Figure 18.	Measured phase error for four various differential amplitude settings.	34
Figure 19.	Modulator output power versus LO frequency.	35
Figure 20.	Modulator output power versus I/Q differential amplitude.	36
Figure 21.	Modulator output power for various LO drive levels.	37
Figure 22.	Low-power amplifier LPA-4-14 from RF Bay, Inc.	38
Figure 23.	Measured S-parameters of LPA-4-14 No. 1, SN 11062823.	40
Figure 24.	Measured S-parameters of LPA-4-14 No. 2, SN 11062824.	41
Figure 25.	DiTom single junction circulator D3C2040.	43
Figure 26.	Measured values of S21 and S12 for the two DiTOM D3C2040 circulators.	45
Figure 27.	Principal mechanical layouts of the circulator connections.	46
Figure 28.	Two dipole elements, of which one is mounted in a ground plane.	47
Figure 29.	Dipole element return loss ( $ S_{11} $ ) measured mounted in the ground plane.	49
Figure 30.	Reference horn pattern measurement (Narda 645).	51
Figure 31.	Dipole element pattern measurement measured at 2.40 GHz.	52
Figure 32.	Low-noise amplifier LNA-2700 from RF Bay, Inc.	53
Figure 33.	Measured S-parameters of LNA-2700 No.1, SN 12062858.	55
Figure 34.	Measured S-parameters of LNA-2700 No.2, SN 12062859.	56
Figure 35.	AD8347EVAL wiring connections and mode settings.	59

Figure 36.	AD8347 demodulator evaluation board schematic (From [46]).	60
Figure 37.	AD8347 Demodulator phase measurement setup.	61
Figure 38.	Plotted AD8347 demodulator phase characteristics.	63
Figure 39.	Characteristics of the two selected AD8347 demodulator boards.	64
Figure 40.	Z-Comm VCO V800ME10 mounted in a MINIEVAL evaluation board.	65
Figure 41.	System level architecture for the full-scale WNODAR (After [20]).	70
Figure 42.	System level architecture for the demonstration array (After [20]).	71
Figure 43.	CAD model of a demonstration T/R module mechanical layout inside a 2 x 4 x 8 [in <sup>3</sup> ] enclosure.	73
Figure 44.	Final demonstration T/R module mechanical layout (unwired).	74
Figure 45.	Block diagram of eight-element demonstration array.	76
Figure 46.	Block diagram of initial two-element demonstration array.	77
Figure 47.	Sketch of the NPS anechoic chamber (From [54]).	78
Figure 48.	Fundamental Rx measurement setup in the anechoic chamber.	79
Figure 49.	Block diagram of the array transmission measurement in the anechoic chamber.	82
Figure 50.	Simulated directivity of the eight-element demonstration array.	84
Figure 51.	Eight-element array over a ground plane.	85
Figure 52.	MATLAB plots of simulated antenna array beam steering.	91
Figure 53.	CST Microwave Studio model of eight dipole elements over a ground plane.	92
Figure 54.	CST Microwave Studio simulated sum patterns (eight-element array).	93
Figure 55.	Comparison between simulated results from CST MWS and MATLAB ( $\theta_s = 0^\circ$ ).	94
Figure 56.	Comparison between simulated results from CST MWS and MATLAB ( $\theta_s = 40^\circ$ ).	95
Figure 57.	RF leakage contributions (dashed lines).	99

## LIST OF TABLES

Table 1.	Instrumentation list. ....	25
Table 2.	Quadrature modulator input settings and resulting phase error for modulator board 1 with a differential amplitude of 2.0 V (sample table). ....	33
Table 3.	Subset of the LPA-4-14 specifications. ....	39
Table 4.	Specified and measured S-parameters for LPA-4-14. ....	42
Table 5.	LPA-4-14 power consumption. ....	43
Table 6.	Specified and measures parameters for D3C2040 circulator.....	44
Table 7.	Subset of the LNA-2700 specifications. ....	54
Table 8.	Specified and measured S-parameters for LNA-2700.....	57
Table 9.	Measured and calculated VSWR related parameters for LNA-2700.....	57
Table 10.	LPA-4-14 power consumption. ....	58
Table 11.	Procedure to operate the AD8347 demodulator in the VGIN mode.....	60
Table 12.	Demodulator phase measurement settings.....	62
Table 13.	Tabulated AD8347 phase characteristics.....	64
Table 14.	VCO evaluation board configuration.....	66
Table 15.	Minimum ground plane dimensions. ....	86

THIS PAGE INTENTIONALLY LEFT BLANK

## ACKNOWLEDGMENTS

First of all I want to express my gratitude to the Swedish Armed Forces for giving me, in stiff competition with capable colleagues back home, this splendid opportunity to study at Naval Postgraduate School. At NPS we truly find a unique blend of academic excellence and advanced research, all with a military foundation. I have tried to drink as much as possible from the vast well of knowledge during my stay here.

In this very inspiring surroundings in general, it has been a great pleasure for me to have been able to work with Professor David C. Jenn in particular. Thank you, Sir, for your guidance and invaluable support. Your door has always been open, for which I am very grateful.

I would like to direct a special thank you to Professor R. Clark Robertson and Professor Richard W. Adler. I appreciate that you so willingly took me on and agreed to guide me in this research as my Thesis Committee members.

I owe much gratitude to Mister Robert D. Broadston, Lab Director of the ECE Microwave Lab. Without your enthusiastic support and knowledge of great and small things within this technological field, many of the results in this work would not have been achieved.

Finally, I would like to thank my beloved wife Carolina and our dear son Hilmer for putting up with me during long periods of intensive studies at NPS. Thank you, Carolina, for the support and for all your sacrifices to be able to share this adventure with me. Thank you, Hilmer, for being such a ray of sunshine in our lives ever since you joined us here in Monterey on the 4th of July 2005.

THIS PAGE INTENTIONALLY LEFT BLANK



## **EXECUTIVE SUMMARY**

Phased array antennas are generally the antenna architecture of choice for most modern high performance radar systems. Traditionally, the elements are connected through a beamforming network of a system of microwave transmission lines and power dividers. A conventional phased array system consisting of thousands of elements is bulky, heavy and power demanding.

The wirelessly networked opportunistic digital array radar (WNODAR) concept aims at making the most of the technological advances within digital wireless communication. The radar system will be edified by a large number of transmit–receive (T/R) modules, which will be placed on any available space in the surface of the platform and, hence, form a thinned array system. The T/R modules are supposed to be stand–alone and will not have any wired connections other than prime power. All data to each module, including local oscillator (LO) signal, beamforming and synchronization information, as well as the radar return data from the modules will be conveyed wirelessly.

A WNODAR application has been studied at the NPS Microwave Lab for the past three years assigned by the Office of Naval Research (ONR). One objective of the present research at NPS is to develop a demonstration array operating at 2.4 GHz in order to verify some fundamental properties of the WNODAR concept.

Previous research has investigated the use of commercial quadrature modulator and demodulator boards, to be used in the T/R module transmission and reception systems, respectively. So far in the project, the devices have been examined separately. However, one objective of this thesis was to develop a demonstration T/R module with simultaneous Tx and Rx functionalities. In the demonstration array, the beamformer and controller functions are represented by National Instruments software application LabVIEW and NI field programmable gate array (FPGA) technology.

Key components in the module are the quadrature modulator AD8346 and the quadrature demodulator AD8347. These devices, mounted on evaluation boards, were re-characterized within the scope of this research. The devices were measured under various bias conditions and were characterized in terms of output/input power levels (RF and LO levels) and phase response. A calibration procedure was designed for the demodulator so that the calibration data can be used in the receive processing to correct the device phase errors.

To build the demonstration T/R module using commercial off the shelf (COTS) components, devices had to be evaluated, purchased and characterized (i.e., validated for this particular application). Chapter III in this report covers the characterization of all components constituting the projected T/R module.

The resulting data from the characterization was used to analyze a proposed demonstration array system. An eight–element demonstration array was developed based on the FPGA devices and will eventually be measured in the NPS anechoic chamber. Prior to that, a two–element demonstration array will be bench tested in order to establish simultaneous control of the transmit and receive functions.

A power budget analysis for an eight–element demonstration array was conducted in order to establish whether any additional amplification was needed in the T/R module for proper operation in the chamber. The power levels on both sides (for transmit as well as for receive) were found to be adequate, and no supplementary amplification is foreseen.

The eight–element demonstration array was modeled in two simulation software tool applications (MATLAB and CST Microwave Studio) in order to predict antenna patterns. The model incorporated in MATLAB used simple formulas given by linear array theory, whereas the Microwave Studio model is more complex and includes mutual coupling and edge effects. The two simulations showed good agreement.

## **I. INTRODUCTION**

In early July 2006, North Korea launched its latest series of missile tests, including a Taepodong-2 missile with a claimed range of nearly 9,000 miles. This range implies that the missile theoretically could reach mainland U.S.A. from East Asia. In the U.S., the question was raised as to whether the National Missile Defense (NMD) system [1] could have been able to deny a North Korean attack on crucial point targets in the U.S. The NMD program has been in development since President Ronald Reagan's administration and has so far cost some \$100 billion [2]. The Pentagon spends about \$8 billion to \$9 billion annually on the program, so the U.S. tax payers' concern about the expected security enhancement return is justified.

### **A. NATIONAL MISSILE DEFENSE**

On July 22, 1999, the National Missile Defense Act of 1999 (Public Law 106-38) was signed into law. This law [3] states,

It is the policy of the United States to deploy as soon as is technologically possible an effective National Missile Defense system capable of defending the territory of the United States against limited ballistic missile attack (whether accidental, unauthorized, or deliberate) with funding subject to the annual authorization of appropriations and the annual appropriation of funds for National Missile Defense.

The NMD system would be a fixed, land-based, non-nuclear missile defense system with a space-based detection system, consisting of five elements:

- Ground Based Interceptors (GBIs)
- Battle Management, Command, Control, and Communications (BMC3), which includes:
  - Battle Management, Command, and Control (BMC2), and
  - In-Flight Interceptor Communications System (IFICS)
- X-Band Radars (XBRs)
- Upgraded Early Warning Radar (UEWR)

- Defense Support Program Satellites/Space-Based Infrared System (SBIRS)

All elements of the NMD system must work together to respond to a ballistic missile directed against the United States. The entire program implies a series of policy-related as well as technological challenges. This research focuses on the Early Warning Radar (EWR) aspect.

## **B. THESIS MOTIVATION**

In years since the end of the Cold War, the increased proliferation of ballistic missile systems and weapons of mass destruction has raised the importance of developing and fielding a capable Ballistic Missile Defense (BMD) system, as a number of potentially hostile countries and possibly even terrorist organizations have acquired these dangerous capabilities. The post-Cold War era offers new threats significantly different from the old Soviet Union threat. The fundamental goal of the planned United States BMD is building a layered defense to defend the United States and its forces, territories, allies and friends. Since the enemies and the courses of attack today are less defined, the U.S. Homeland Defense System must comprise a larger number of small, mobile, and dispersed units ready to be detached globally to potential trouble spots.

All ballistic missiles share a fundamental characteristic. They follow a trajectory which includes three flight phases: boost, midcourse and terminal. By fielding a layered defense system and attacking the missile in all phases of flight, the idea behind BMD is to exploit opportunities to increase the effectiveness of ballistic missile defense.

The engagement sequence of the BMD is depicted in Figure 1. A crucial part of the system is the UEWR, i.e., the function to detect launch and perform long-range surveillance and tracking for the ballistic missile. Navy ships can be forward deployed close to an adversary's suspected launch sites. If the ships are equipped with large phased array radars (LPAR) with thousands of active array elements, they can detect and discriminate missile targets from thousands of miles away. The early and accurate tracking information during the ballistic missile's boost phase is vital in the system to accommodate a GBI launch in order to intercept the missile mid-course.

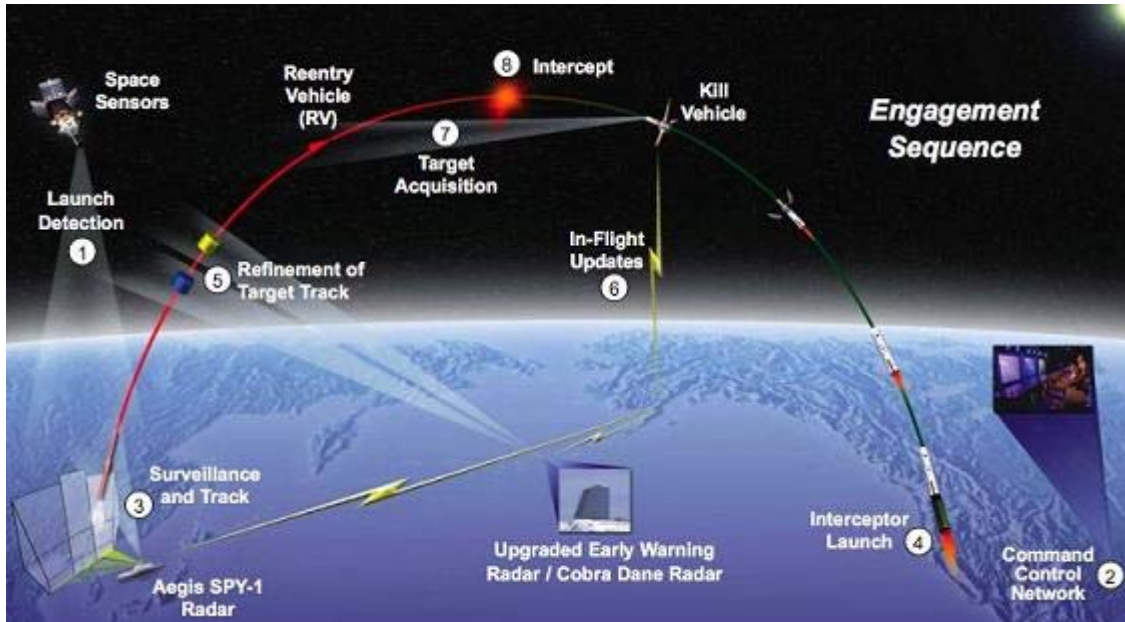


Figure 1. Ballistic missile defense engagement sequence (From [4]).

Today, the U.S. early warning radars (EWR) are land-based phased-array surveillance radars used to detect and track ballistic missiles targeted at the United States. Among the systems used for the NMD Program are the PAVE PAWS [5] (AN/FPS-115; PAVE is a U.S. Air Force program name for electronic systems, while PAWS stands for the Phased Array Warning System) and the aging Cobra Dane (AN/FPS-108) [6]. The latter system was developed mid 1970s and was deployed in 1977. It operates in the L band at frequencies between 1,215 — 1,400 MHz using a 29 meter phased array antenna. These two land-based LPAR systems are shown in Figure 2.

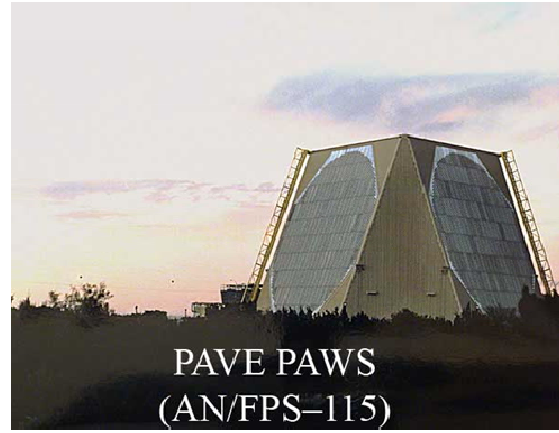
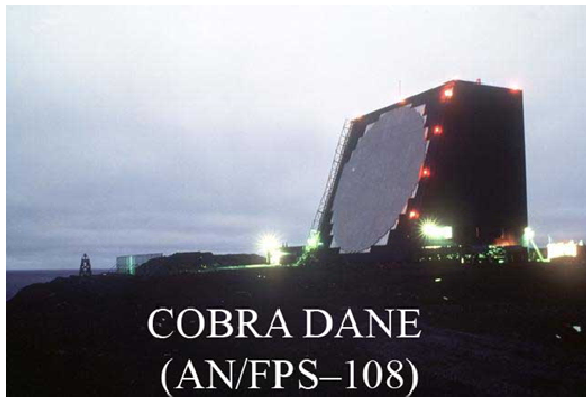


Figure 2. Two LPAR systems that constitute the UEWB components of the NMD (Courtesy of Boeing and Raytheon, respectively).

The U.S. Navy currently has an Aegis fleet for possible forward deployment. The Aegis concept was designed and developed as a complete system, including the capable radar system AN/SPY-1 [7]. This radar system is a conventional Phased Array Radar system with four fixed antenna arrays mounted on the superstructures of the Ticonderoga (CG 47) and Arleigh Burke (DDG 51)–class warships, see Figure 3.

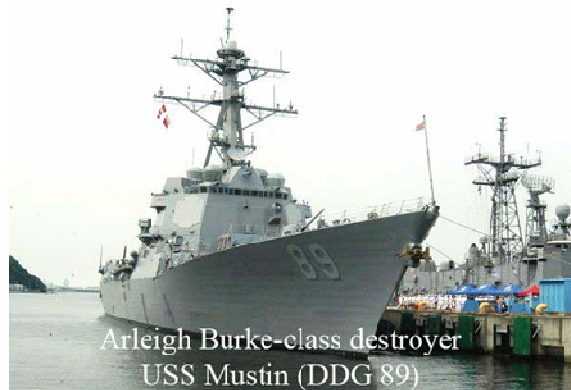


Figure 3. Two classes of U.S. warships equipped with the radar system AN/SPY-1 (After [8]).

The U.S. Navy recently announced that the first of the next-generation DD(X) destroyer will be designated DDG 1000 [9], see Figure 4. These Zumwalt-class destroyers will be equipped with Dual Band Radars [10], combining the functionalities of

the AN/SPY-3, a high frequency, multi-function horizon search and fire control radar (Multi-Function Radar, MFR) at X-band with that of a lower frequency Volume Search Radar (VSR) at L-band. Three X-band apertures and three L-band apertures are controlled by a single target tracker. This next-generation multi-mission surface combatant is tailored for land attack and littoral dominance, with capabilities designed to defeat current and projected threats.

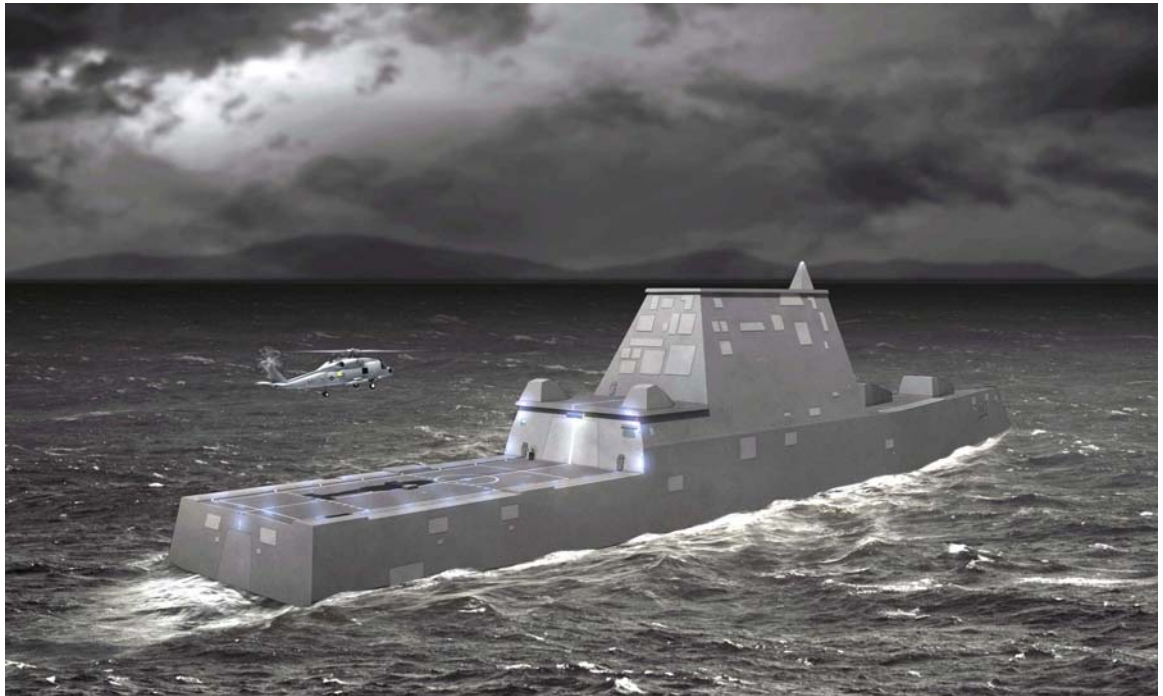


Figure 4. Artist concept of the Zumwalt-class guided missile destroyer, DDG 1000 (Courtesy of Northrop Grumman).

It is desirable to use ship based BMD EWR systems for rapid deployment to any hot spot that might unfold globally. Both the present AN/SPY-1 and the near future AN/SPY-3 systems, however, are currently overloaded with various functionalities, and would not be able to also handle the EWR function. Furthermore, these two radar systems have operating frequencies (X-band), which due to propagation losses will not be able to exhibit the necessary range coverage required for a BMD EWR application. A secondary radar system would be desired to fulfill the EWR requirements [11].

Recently, the Systems Engineering and Analysis Cohort Nine (SEA-9) was given the task to examine future surface combatant operations in terms of their conduct and support of current and emerging sea-based Theater Ballistic Missile Defense (TBMD) missions. The considered timeframe was 20 to 25 years into the future, and the group analyzed existing and emerging sensors and interceptors. Regarding the required sensor suite for the future surface combatant, the project group foresees the use of a combination of a Multifunction Phased Array Radar (MFPAR) as well as a Skin of the Ship Radar (SOTSR) [11].

Even though the phased array radar concept offers several benefits on the system performance, it also entails some drawbacks, especially for large arrays for ship-borne applications. The conventional phased array antenna approach with a microwave beam former with analog components is bulky, costly, power-consuming and heavy. With the desire to place this main sensor as high as possible for maximized range coverage, a ship designer ends up with the undesired trade-off of a top-heavy design versus performance reduction. Large cutouts in the ship surface for insertion of the arrays weaken the structure and complicate the mechanical design of the ship.

As a representative of future generations of U.S. surface warships, the Zumwalt-class destroyer is offering opportunities for further improvements of radar performance. For instance, this can be achieved by employing a novel opportunistic array concept, currently under development at the Naval Postgraduate School. Antenna elements with their separate Transmit/Receive (T/R) modules can occupy any available surface of the ship's superstructure and hull, offering a 3-D thinned phased array antenna covering the entire length, beam and height of the ship. An antenna array with these dimensions permits the radar to operate at VHF/UHF and still meet the system performance specifications. The "aperstructure" concept developed by the Office of Naval Research (ONR) can be used, i.e., the elements can be integrated into the platform superstructure. Furthermore, the individual T/R modules can be wirelessly and digitally controlled and require no hardware connections other than prime power.



This ongoing research project at NPS is designated as a Wirelessly Networked Opportunistic Digital Array Radar (WNODAR) and is discussed in further detail in Chapter II.

### **C. PREVIOUS WORK**

The research at NPS on radar applications based on opportunistic arrays has been in progress for three years. The work is described in seven Master Theses [12 through 18].

The concept of Genetic Algorithm (GA), a simulation tool for random and aperiodic arrays, was used to model and test designs of phased array radars in [12]. The project foundations, and the keys to making the WNODAR concept practical, are the digital array architecture and the low-cost commercial off-the-shelf (COTS) hardware. For demonstration purposes, a test-bed transmit array antenna consisting of 24 elements using commercial modulator boards was designed and evaluated. Simulated results using GA and the Method of Moments (MM) were compared with measured data achieved in the NPS anechoic chamber.

In [13], the architecture of the complementary receive array was examined using commercial demodulator boards. The demodulators were characterized and demonstrated suitable for the receive application. Another result presented in this report, however, is that the particular demodulator board does not possess instantaneous wideband phase characteristics.

The research was continued in [14], where the commercial-off-the-shelf component characterization was refined. A preliminary laboratory transmit setup was introduced incorporating commercial modulator and Direct Digital Synthesizer (DDS) boards. The mixing function of the particular modulator was found incapable of sufficiently suppressing the image signal, which implies that a bandpass filtering function is required. This problem was later solved in the succeeding research [15].

Concepts for synchronization and radio frequency (RF) synthesis were examined in [15]. The prospect of using DDS in digital radar applications was studied, and more

precisely, frequency up-conversion, waveform generation and synchronization issues of multiple synthesizers were addressed.

One of the subjects presented in [16] was of a system level tradeoff study to verify that a WNODAR onboard a Zumwalt-class sized ship can achieve the necessary detection and tracking ranges for a shipborne BMD application using the UHF/VHF frequency bands. A MATLAB based system study regarding the radar performance of the aperstructure and opportunistic array concepts versus the number of antenna elements was conducted. Finally, a U-slot microstrip patch antenna design was completed, and its characteristics were validated using the simulation tool CST Microwave Studio.

The challenge of distributing the radar system's local oscillator (LO) signal was addressed in [17]. A strict and controlled synchronization of the antenna elements is essential in order to achieve the necessary coherent operation. Another aspect discussed in this report is wireless distribution of data and control signals between the beamforming unit and the individual T/R modules.

The research presented in [18] covers several areas of study. The phase synchronization of the antenna elements is possible using a simple synchronization circuit and with little affect on the radar performance. The consequences on the array element positions due to the hull's dynamic deflections were analyzed. No correction was deemed necessary for a WNODAR system operating in the VHF/UHF frequency bands. Finally, a design of a demonstration T/R module using commercially available components was proposed in order to validate the basic concepts of a WNODAR.

#### **D. THESIS OBJECTIVE**

This thesis describes the architecture of the final WNODAR and some of the remaining technological challenges are addressed. The emphasis is on the design of a demonstrator Transmit-Receive (T/R) module and component characterization, as well as the design of a demonstration array that operates at 2.4 GHz. The objectives of this thesis are threefold:

1. Characterization of critical COTS devices.
2. Development of a demonstration T/R module.
3. Design and simulation of a demonstration array operating at 2.4 GHz.

## **E. THESIS ORGANIZATION**

The research presented in this thesis carries on the work performed in [12—18]. Chapter II deals with design elements of the proposed WNODAR system.

Chapters III and IV present the work regarding the development and design of the T/R Module and a two–element demonstrator. The final WNODAR will operate in either the UHF or the VHF frequency band; however, the demonstration array will operate in the Industrial, Scientific and Medical (ISM) radio band around 2.4 GHz to reduce size as well as take advantage of readily available components from the cellular communications field.

Finally, Chapter V summarizes the research presented and the conclusions made in this work. The reader also finds some recommendations for the follow–on study toward realization of a full–scale WNODAR.

THIS PAGE INTENTIONALLY LEFT BLANK

## II. SYSTEM LEVEL ARCHITECTURE OF THE WNODAR

This chapter discusses the research at NPS related to a WNODAR. It is a summary of the current status of the development and the long-term goals of the research.

Modern solid state phased array antennas are the preferred design for any high-performance radar application. Using this kind of antenna system, the transmitter and receiver functions are composed of numerous small T/R modules. The antenna elements are fixed, and feature many advantages over mechanically scanned antennas. The advantages include very fast scanning rate (micro-seconds), longer range due to its ability for longer dwell-time on a single target, capability of tracking a higher number of targets due to multiple agile beams, and a low probability of intercept (LPI). The architecture is well suited for surface integrated antenna elements, which implies the prospect of a low radar cross section (RCS).

A conventional beamforming network can be physically large and consequently heavy, as some of the applications tend to consist of several thousands of elements that are spaced about half a wavelength at the operating frequency. For example, the Cobra Dane LPAR [19] in Figure 2 operates at L-band (at 1,215—1,400 MHz) and the 15,360 active and 19,408 passive elements together form a 29 m diameter array antenna of circular shape. The radar generates 15.4 MW of peak RF power from 96 traveling wave tube (TWT) amplifiers. The radar system can locate an object 0.1 m in diameter at a range of 2,000 nautical miles with an accuracy of 5 m.

The idea of the WNODAR is to utilize any available space on the ship's hull and superstructure as a location for an array element. In this manner, a thinned phased array will be formed with a seemingly random placement of the elements. Every element consists of a separate T/R module, and if a large enough number of these modules is being employed, the total output power of the array can be comparable to a ground based BMD radar.

### A. WIRELESSLY NETWORKED OPPORTUNISTIC DIGITAL ARRAY RADAR

A simplified block diagram of the proposed WNODAR system architecture is presented in Figure 5. For clarity, only one array element with its T/R module is depicted. The radar system comprises a central digital beamformer and controller unit that communicates wirelessly with hundreds or even thousands of array elements. The system central unit would be located in a suitable apparatus room on board, whereas the array elements are scattered apparently randomly over the ship's hull and superstructure, preferably surface-integrated for lower signature, as previously mentioned.

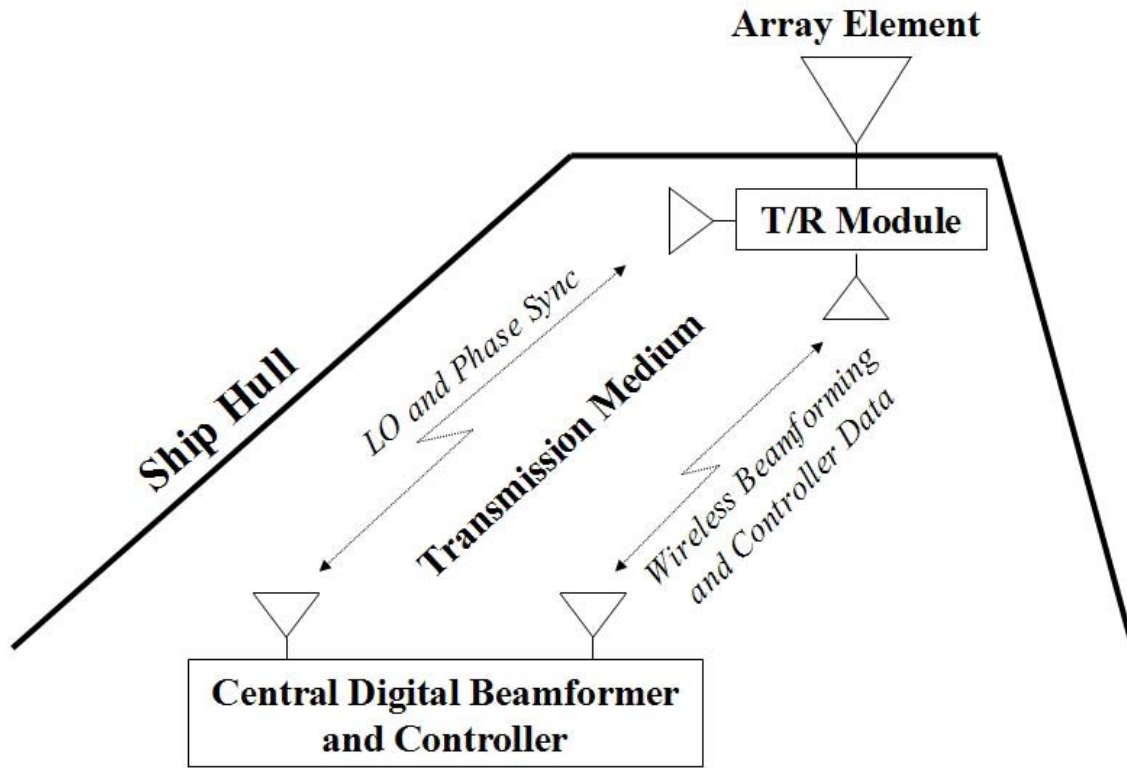


Figure 5. System level architecture for the WNODAR (After [20]).

The WNODAR approach combines a series of concepts which are concurrently under development. A brief survey of each of the comprising components follows.

## **1. Wireless Network**

Advances in wireless communication have enabled the generation of low-cost, low-power and technologically capable sensor nodes that are small in size. The major driver for this development is the commercial cellular technology, which is making great advances globally. In a shipborne application, every contained Transmit/Receive module with its antenna element could be regarded as a separate sensor node in a larger network. The communication of the local oscillator RF as well as the beamshaping control signals and the preprocessed receive signals would be carried out wirelessly to and from each module and a central signal processing unit. Several wireless sensor network architectures have been proposed in the literature, and there has been a substantial amount of research conducted in this field at NPS [21].

## **2. Opportunistic Arrays**

The concept of opportunistic arrays implies that any available open area of the platform will be occupied by an array element. The elements could be several hundreds or even thousands in number and would cover the entire length, beam and height of the platform. The key aspect of the design is modularity — the array constitutes of self-standing digital T/R modules with no hardwire connection other than prime power.

An opportunistic array spread over an entire ship offers a long array base in physical dimensions as well as length in terms of wavelength. This has a positive impact on the resulting overall antenna array characteristics such as narrow beams and longer radar range. For illustration purposes, Figure 6 displays a Zumwalt-class sized ship with 1,200 elements randomly distributed on its superstructure and hull.

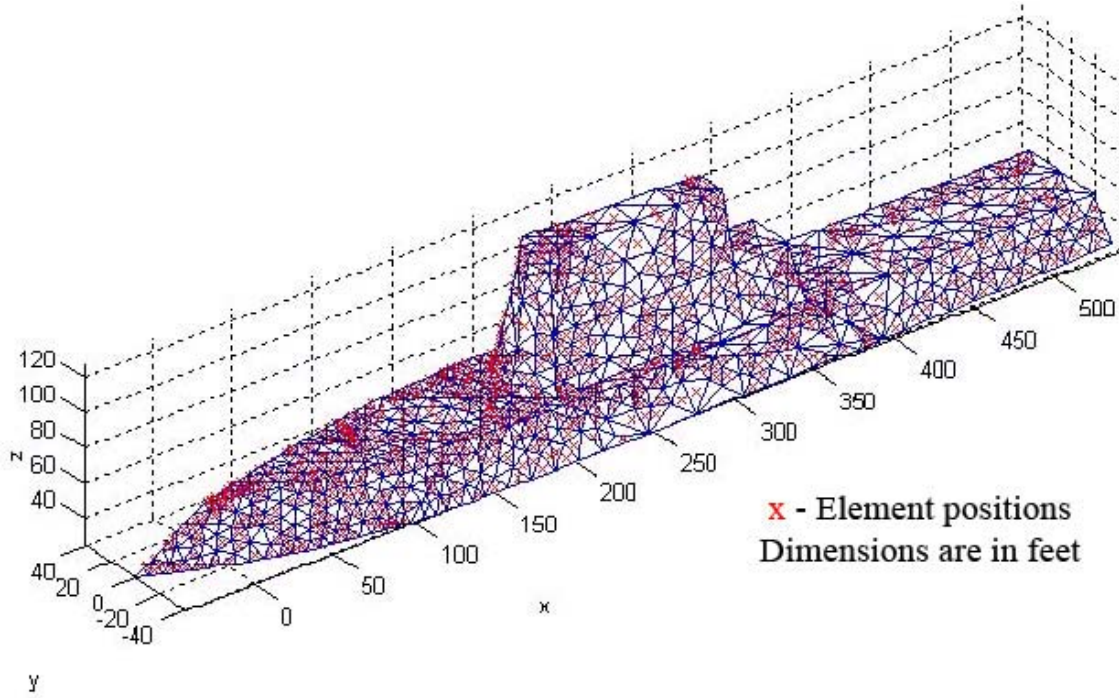


Figure 6. CAD model of Zumwalt-class sized ship with 1,200 randomly distributed integrated antenna elements (After [16]).

### 3. Digital Antenna Arrays

In a digital antenna system, the beamforming control signals to the modules, as well as the resulting return signals, are sampled and processed digitally. Digital architecture offers many advantages over the traditional analog technology [22]. Digital signals are easily regenerated; hence, this technique is less subject to distortion and interference than are analog systems. Other advantages to a digital system are more reliable circuits, less costly manufacturing, and more flexible applications.

Other positive aspects of a digital antenna array are that it can achieve flexible waveforms and processing, making the system capable of sustaining multi-function operation. Using distributed elements, the antenna system is reconfigurable and shows high survivability with graceful degradation when losing elements for any reason.

Not long ago, regarding electronic circuits and radar systems in particular, military applications were moving the technological frontiers further. Today, and especially within the field of digital communications, the commercial market has in many ways taken the lead and provides a tremendous thrust to research and the subsequent



technological advances. The proposed NPS concept benefits from this development and the realization of a WNODAR is technologically achievable.

## B. TRANSMIT/RECEIVE (T/R) MODULE

The T/R module operating in the upper VHF or the lower UHF frequency band will have a proposed design as shown in Figure 7. The digital baseband signal is generated by the direct digital synthesizer (DDS) at each array element using the central digital beamformer and controller data. The digital signal is modulated onto the operating frequency and power amplified prior to transmission. On receive, the RF signal is low-noise amplified before demodulation and A/D conversion. The resulting in-phase and quadrature (I/Q) information is transferred wirelessly for signal processing by the central control unit. The local oscillator (LO) signal is distributed wirelessly together with necessary phase synchronization data to each individual element.

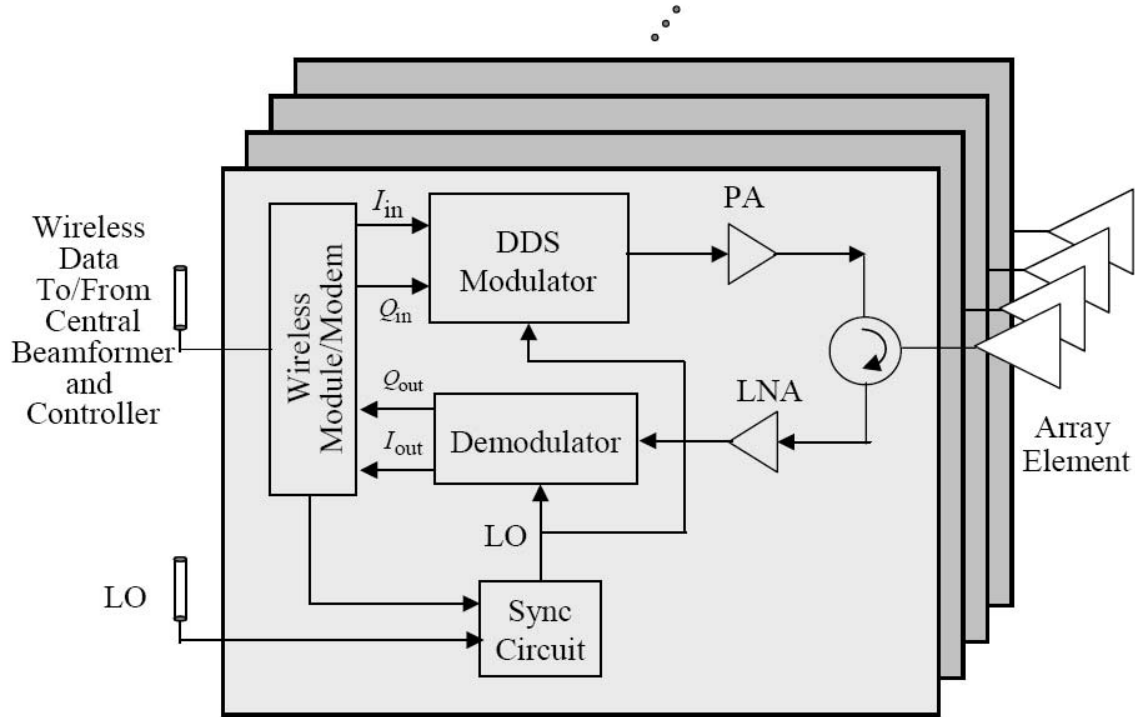


Figure 7. Proposed system architecture of the T/R module (From [23]).

An overview of some of the currently addressed technological challenges of the WNODAR concept follows.

## **1. LO Wireless Distribution**

The WNODAR application is expected to comprise hundreds to thousands of elements dispersed on the surface of the ship [23]. A traditional approach using wired connections to all elements would not be feasible; hence, the desire for a wireless system.

For coherent operation of the radar system, each element must be synchronized to time and phase references. The synchronization is essential to scan the beam and perform coherent detection and integration. A demonstration to prove the principles of wireless LO distribution has been conducted for a two-element transmit array [17]. The study involved a comparison between a wired and a wireless arrangement, and it showed good agreement in expected received LO power and phase.

## **2. LO Synchronization**

An algorithm and circuitry is required to continuously synchronize the LO signals in real time. This function is shown as one of the components of the T/R module in Figure 7.

In [18], a study regarding two different synchronization techniques is presented. A “Brute Force” synchronization technique is compared with a more efficient “Beam Tagging” method. However, the “Brute Force” procedure is simple and can easily be implemented with a synchronization circuit in each individual element and in the central beamformer and control unit. A possible realization of the element synchronization circuit is shown in the diagram in Figure 8.

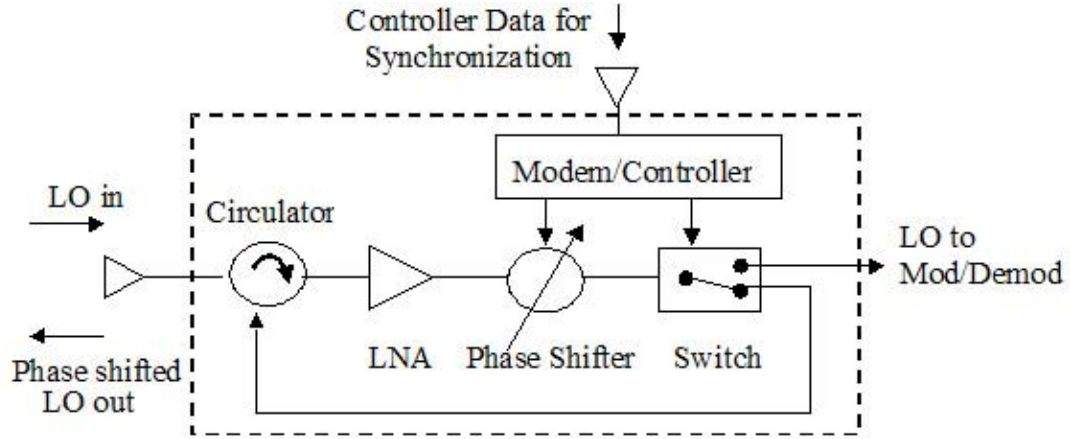


Figure 8. Diagram of a synchronization circuit for one element (From [23]).

The controller synchronization data contains the required phase setting for each element. One element will be set as reference (i.e., it will experience no additional phase shift), whereas the other elements will be phase shifted according to the difference in the channel path lengths. The synchronization is performed periodically as required by the transmission channel. The synchronization principle, shown for the reference element and element  $n$ , is depicted in Figure 9.

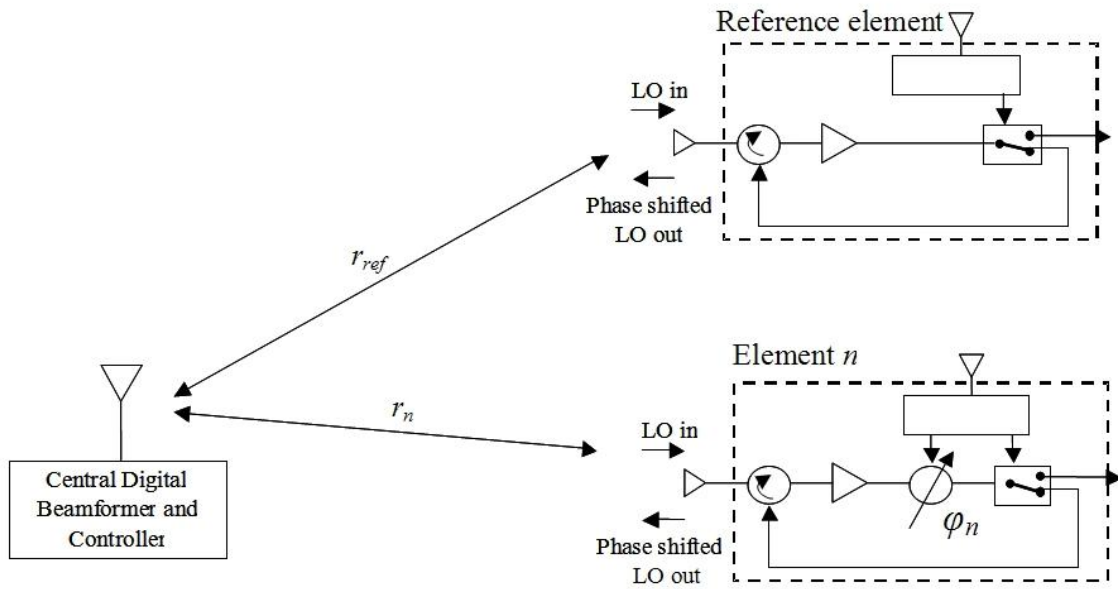


Figure 9. Illustration of the brute force phase synchronization technique (After [23]).

### **3. Element Geolocation**

Another challenge for the realization of a WNODAR system is tracking of the elements exact locations. As mentioned above, it is crucial to know the elements' relative path lengths versus a reference element in order for the controller to provide each of them with accurate phase information to scan the beam. Element geolocation, i.e., knowledge of the element positions, is desirable for digital beamforming. A ship sometimes operates in harsh environments, where the hull is deflected mechanically in all six degrees of freedom due to the effects of the prevailing sea state. The radar system must know the element positions within a fraction of wavelength to compensate for varying phase errors in order to avoid degraded performance in sidelobe levels, gain and beam pointing.

A survey of several available state-of-the-art means of measuring element geolocation was executed in [18], resulting in some possible commercial solutions. Furthermore, the effects on WNODAR performance due to hull deflection were examined. For the final radar system operating around 300 MHz, the effects were found to be negligible for a tolerable position error limit of  $0.1\lambda$  (i.e., 0.1 m).

### **4. Wireless Transmission Rates**

The wireless opportunistic digital array concept requires very high data rate communication. The central beamforming and controller units continuously communicate synchronization and beam control information wirelessly with hundreds or even thousands of individual T/R modules, which in turn transmit digitized radar return signals to the controller. The commercial market has driven a recent development of low-cost, high performance wireless communication systems, which will facilitate the digital radar application.

The current IEEE wireless local area network (WLAN) standard family 802.11 offers a peak data rate of 54 Mb/s operating at both 2.4 GHz and at 5 GHz. The standards are restricted to the ISM frequency bands, which in most countries can be used without license. Since higher bit rates can require higher transmission bandwidth, there are efforts to next exploit the ISM band around 60 GHz for WLAN applications [24]. However,

transmissions around this frequency experience large atmospheric attenuation due to absorption by water vapor. The novel WLAN application around 60 GHz offers approximately a 7 GHz unlicensed bandwidth, which makes a very high data-rate (i.e., above 1 Gb/s) wireless transmission possible, but with a limited range.

Other related research to develop a next generation advanced wireless network is The INtelligent Airport (TINA) conducted by University of Cambridge with a grant from the U.K. EPSRC [25]. The Engineering and Physical Sciences Research Council is the U.K. Government's leading funding agency for research and training in engineering and the physical sciences [26]. The project aims at an upgradeable and secure wireless system that will support an assumed aggregate peak rate transmission of 100 Gb/s using self-organizing networks using a Passive Optical Network (PON) and an infrastructure consisting of a number of standard commercial sub-WLANs, as in Figure 10.

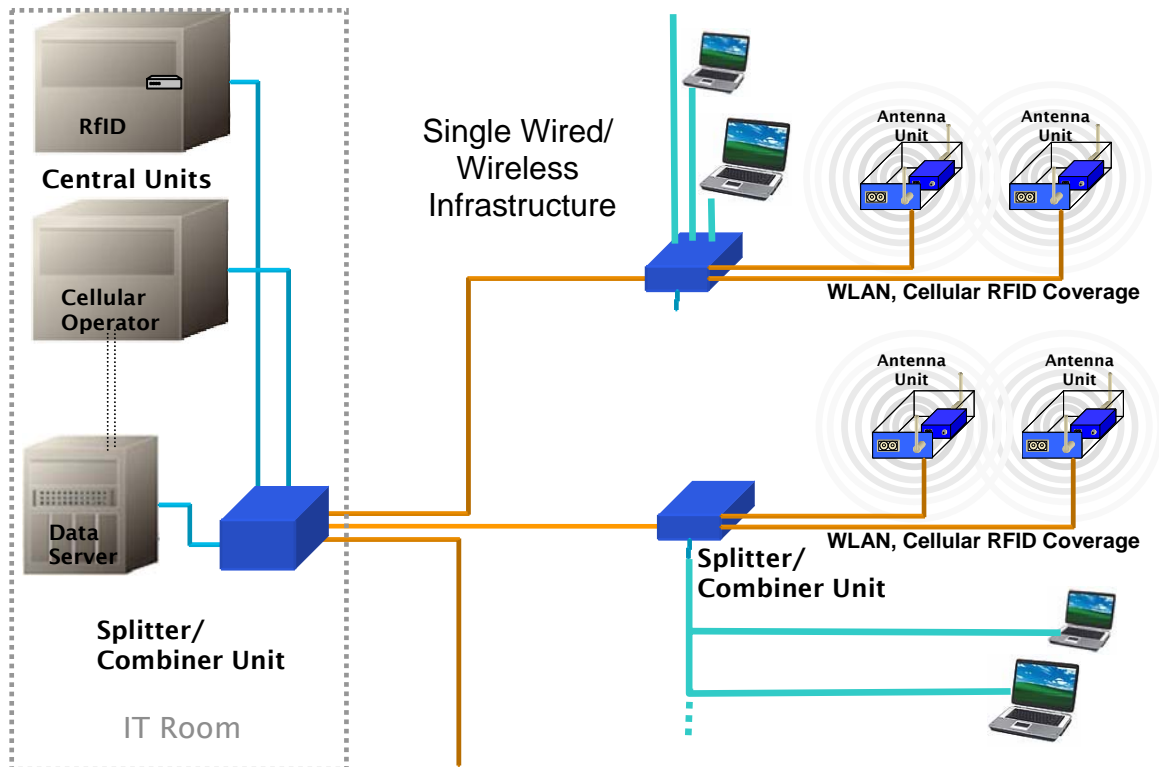


Figure 10. Proposed first phase airport network of the TINA project (From [25]).

TINA is an example of a combined wired/wireless infrastructure system. The central control unit communicates on optical fibers to a number of splitter/combiner units, which in their turn support several antenna units. Eventually this combined wired/wireless approach might be considered for the WNODAR realization. Based on the large number of antenna elements and the amount of information sent between the central unit and the many elements, estimated at 3.7 Gb/s data transmission rate [18], the system would benefit from the capability of optical fiber communications.

In the WNODAR application, a wireless system similar to the TINA approach has advantages over a wireless system operating at 60 GHz. Higher frequencies will have more difficulty in penetrating the hull and decks, hence, requiring a non-feasible line-of-sight (LOS) transmission system to all elements in the opportunistic array. Other proposed solutions to the harsh propagation environment onboard a ship are the use of an integrated ship transmission system [17] and through-bulkhead relay antennas.

## **5. Further Challenges to be Addressed**

The stand-alone approach of the WNODAR implies new design and new technology challenges, some of which are covered above. In addition to these, there are other technological issues still to be addressed in future research efforts within this field, including:

- How to provide prime power to each element.
- Study of the element radiation patterns in the local environment.
- Study of the element coupling to near-field objects.
- Realization analysis regarding antenna element locations and hull penetrations for feed lines.

## C. OTHER APPLICATIONS

The concept of a wireless distributed antenna array is not new. In September 1999, *Business Week* predicted networked sensor technology to be a key technology for the future [27]. On-going research is exploring the utility for smart disposable microsensors that can be deployed in the battlefield, on the ground, in the air, underwater, in vehicles, inside buildings and even on human bodies [28]. According to this paper, each sensor node will have embedded processing capability and will potentially be equipped with multi-band sensors. The gathered and initially processed data will be transmitted wirelessly to a central processing unit.

The development of WNODAR employs many of the same principles. A number of (randomly) distributed sensors will gather information, which will be combined and processed in a central control computer. Providing the elements of the known locations with appropriate phase information together with the common LO signal will facilitate the system to point the transmitted radiation in the desired direction.

The concept of the WNODAR can be utilized in a wide range of applications. The most obvious, since this research is founded from this field, is a long-range ship-borne application with similar performance specifications used in a forward layer of the U.S. NMD. Some other possible applications are reviewed below.

### 1. Military Applications

The opportunistic and modular architecture of the WNODAR is well suited to be employed by any service in any environment. Existing buildings or a hillside could serve as the array “backplane,” over which the elements would be dispersed. The elements could be scattered under the cover of night or be dropped from a UAV, as suggested by the parallel research presented in [21].

The fact that these elements are dispersed, capable of operating under degraded conditions and quickly repaired, makes them highly resilient to attacks, even from anti-radiation missiles or artillery barrages [16].

## **2. Hastily Deployed Networks**

Moreover, this method is applicable to the field of emergencies and disaster relief. The modular layout of the system makes it suitable for rapid deployment where and when needed. For instance, following the tsunami catastrophe in the Indian Ocean in December 2004, one main reason for the initial difficulties in bringing in sufficient aid and supplies to the region was the lack of air traffic control functions and communication links in the aftermath of the waves. One possible solution to a similar situation is systems based on the opportunistic array approach, using buildings or the terrain as the base for a radar and/or communications applications.

## **3. Commercial Applications**

As foreseen in [27], the concepts of wirelessly networked sensor technology will be used in numerous applications in various frequency bands in the future. Once the technology is mature, these arrays may be applied in any surveillance and tracking system as well as in communication applications.

## **D. SUMMARY**

This chapter has dealt with the WNODAR system level architecture and the comprised T/R module. Some currently addressed technological key issues were described, while previous work was reviewed. The succeeding chapters discuss the design and analysis of a demonstration array operating at 2.4 GHz. Chapter III covers design considerations for the T/R module, including characterization of its components. Chapter IV deals with the development of an array demonstrator employing initially two, and later eight elements in a linear array.



### III. DESIGN CONSIDERATIONS FOR A DEMONSTRATION T/R MODULE

In order to validate the WNODAR concept presented in Chapter II, the next step is to develop a demonstration array consisting of a number of T/R modules. The demonstrator is down-scaled in size and will operate at 2.4 GHz, in contrast to the proposed full-scale WNODAR system operating at approximately 300 MHz. There are various reasons for choosing this particular frequency in S-band (2 – 4 GHz). It operates in the unrestricted ISM frequency band, the components are smaller in size due to the shorter wavelength, and there are an abundance of available integrated circuits from the commercial cellular market. The demonstrator utilizes field programmable gate array (FPGA) technology, which duplicates the functionality of the central Beamformer and Controller unit (see the system level demonstrator design in Figure 11).

This chapter introduces the system level design of the 2.4 GHz demonstration array. The succeeding sections deal with electrical design of the demonstration T/R module, and the chapter concludes by characterization of the hardware components.

#### A. PROPOSED SYSTEM LEVEL DEMONSTRATION DESIGN

A block diagram of the demonstration T/R module using wireless LO distribution is depicted in Figure 11. The main goal with the demonstrator is to validate some fundamental properties and the general practicality of the T/R module concept.

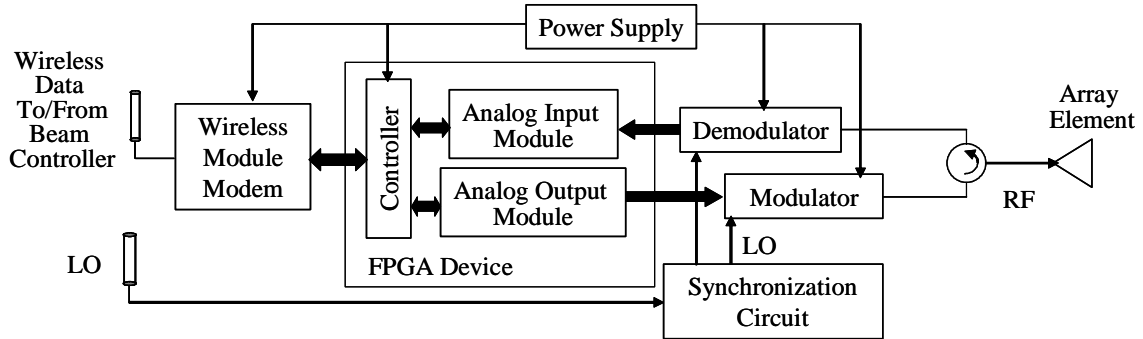


Figure 11. Block diagram of the final demonstration T/R module (From [23]).

The module will be running a National Instruments CompactRIO (cRIO) programmable automation controller (PAC), which is a low-cost reconfigurable control and acquisition hardware line. The cRIO is powered by reconfigurable I/O (RIO) FPGA technology [29]. An FPGA is basically a semiconductor device containing programmable logic components and programmable interconnects. Due to the flexibility of the FPGA function, the down-scaled demonstrator of a full-scale WNODAR is realized using a handful of components. The initial projected T/R module design, as well as the key components together with their characterization, are described in the subsequent sections.

## **B. PROJECTED T/R MODULE COMPONENT LEVEL DESIGN**

The T/R module demonstrator will utilize a wireless LO distribution. As mentioned previously, the validity of this approach was demonstrated in [17]. At this stage of the project, the aim is to verify some of the fundamental properties of an array of individual T/R modules using commercially available RF components. To facilitate this purpose, the initial demonstrator architecture will substitute a hard-wired LO distribution for a wireless one.

Figure 12 displays a simplified schematic of the module using a wired LO channel. At first, the T/R module is operated using a CW signal. Eventually, more complex waveforms will be employed.

The key components in the module are described in the order of signal flow, starting with the National Instruments software application LabVIEW and the FPGA devices.

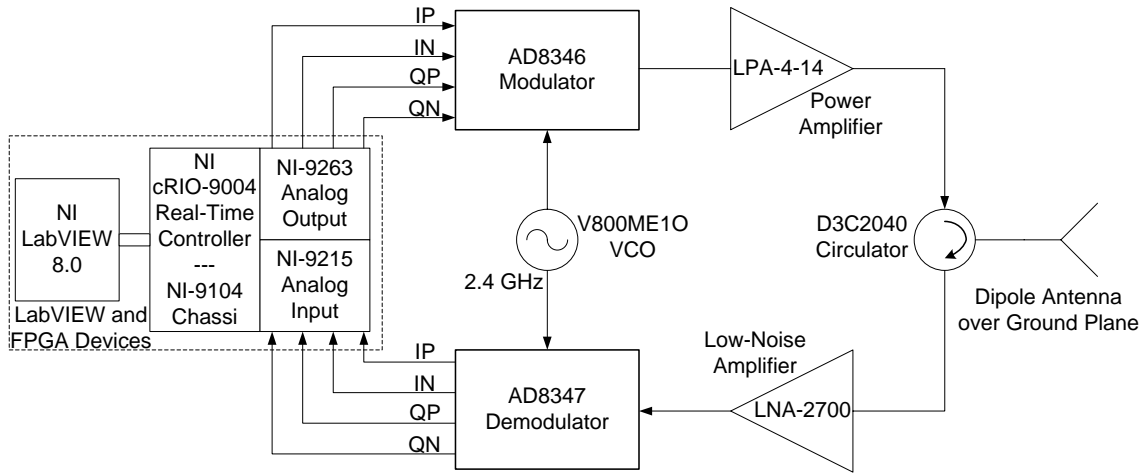


Figure 12. Simplified T/R module block diagram using hard-wired LO signal.

### C. MODULE COMPONENT CHARACTERIZATION

All the components in the proposed demonstration module were first evaluated from the vendor specifications and subsequently purchased. In order to verify specifications and to investigate the devices' utility in the set-up, they were all validated by vector network analyzer (VNA) measurements. The validations were conducted in ECE Microwave Laboratory using the test equipment listed in Table 1.

Measuring Instrument	Model	Serial No.
Vector Network Analyzer	HP-8510C	3031A07050
S-parameter Test Set	HP-8517A	3032A00244
Power Meter	HP-436A	1803A02957
Power Sensor Head	HP-8484A	1528A00556
Reference Attenuator 30 dB	HP-11708A	19764
Microwave Frequency Counter	HP-5342A	2109A04273
Digital Multimeter	Tektronix DMM916	149756
Data Acquisition and Control	NI LabVIEW 8.0	Installed July 2006

Table 1. Instrumentation list.

A crucial instrument for most of the characterization efforts was the Hewlett-Packard vector network analyzer. In order to fully evaluate the component characterization data, the available VNA performance was calibrated during the course of this research. Some of the components in the prototype module are rated for operating

frequencies between 0.8 – 2.5 GHz; hence, a measurement of the VNA Port 1 output power versus frequency was performed over this range. The VNA port 1 was set for three different output power levels (0, +3 and +6 dBm, respectively), and the actual output level was measured using a Hewlett–Packard power meter with a low-noise sensor head and a 30 dB reference attenuator. Figure 13 presents the measured power.

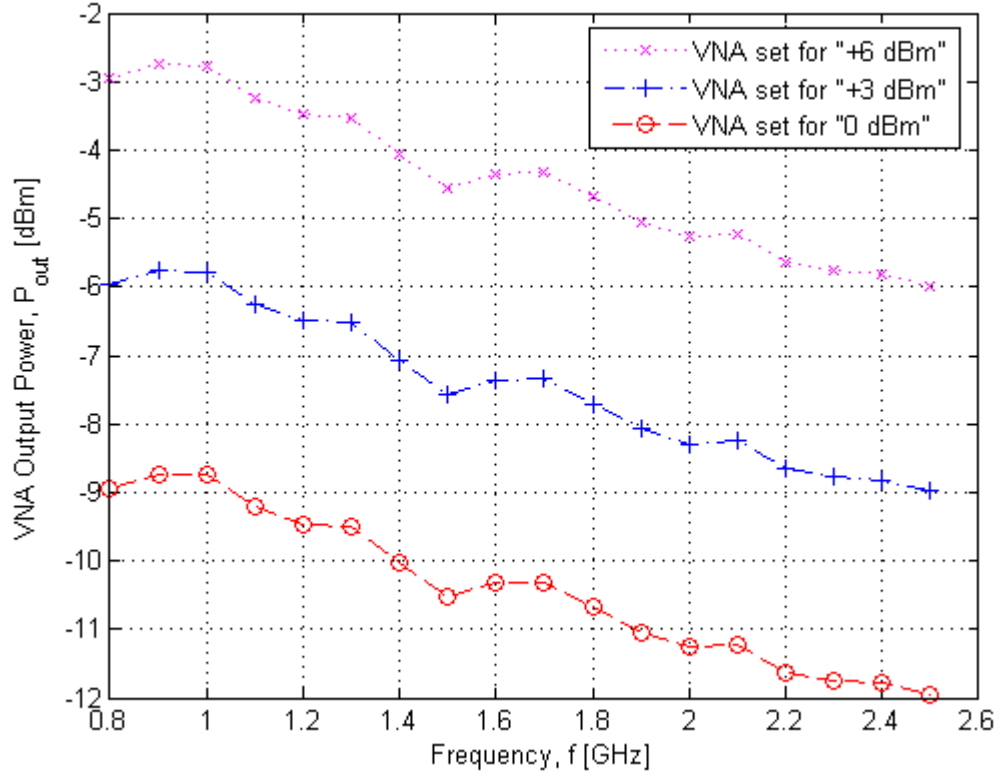


Figure 13. Measured output power level of the VNA Port 1.

Notable is that the VNA output power levels at the frequency for the T/R module (i.e., at 2.4 GHz) are approximately 12 dB below the programmed power levels on the VNA. This fact was to be considered when the components' proper operating conditions were applied in the characterization process.

## **1. LabVIEW**

National Instruments (NI) has been selected as both a hardware and software vendor for the WNODAR demonstration module. Along with their hardware modules, several standard LabVIEW software applications were delivered for controlling purposes.

NI LabVIEW is an industry leading software tool for designing test, measurement, and control systems [30].

## **2. FPGA Devices**

Field programmable gate arrays (FPGAs) are silicon chips with unconnected logic gates. The functionality of the FPGA can be defined by using software to configure the FPGA gates. Due to their versatility and relative low cost, FPGAs are suitable for use as processing components in low to medium volume electronics or where the time and cost of developing and fabricating an applications specific integrated circuit (ASIC) is too expensive. The NI LabVIEW FPGA Module allows LabVIEW to target FPGAs on NI Reconfigurable I/O hardware so engineers can take advantage of the performance and flexibility of FPGAs without needing to learn any low-level design tools [30].

There are two main parts in a LabVIEW FPGA System: the LabVIEW FPGA Module and the cRIO hardware. The LabVIEW FPGA Module extends the LabVIEW environment to develop virtual instruments (VIs) to be implemented as hardware in the FPGA on cRIO hardware. Using LabVIEW is an intuitive way to represent the timing, concurrency and parallelism of FPGA hardware. This was one of the technological challenges when operating several modules from the same VI application, and it will be addressed in Chapter IV.

In order to properly operate the FPGA devices, it is necessary to create the host interface for the FPGA VI. This host interface is built using a small set of VIs from the NI cRIO driver which seamlessly integrates the FPGA hardware with the rest of the measurement and control system. The FPGA interface exchanges information from the LabVIEW VI running in Windows or LabVIEW Real-Time with the front panel controls and indicators on the LabVIEW FPGA VI. The LabVIEW version 8.0 software

applications are, in this case, running on a Windows-based computer and are controlling the FPGA devices as illustrated in Figure 14.

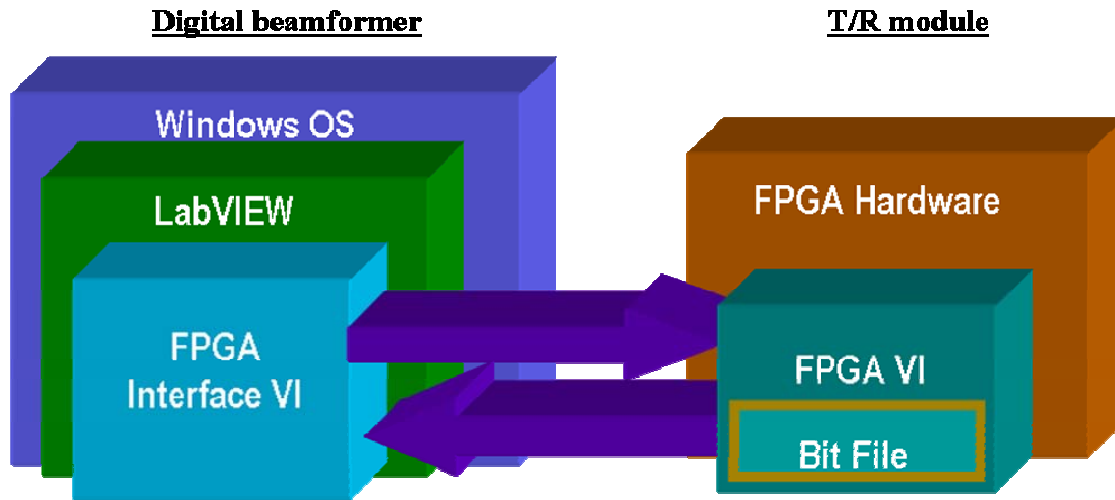


Figure 14. Schematic model of the LabVIEW host interface.

The T/R module in the present configuration consists of the following NI FPGA components shown in Figure 15:

- NI cRIO-9004 Real-Time Controller with 64 MB DRAM, 512 MB CompactFlash [32],
- NI cRIO-9104 8-Slot, 3 M Gate CompactRIO Reconfigurable Embedded Chassi [33],
- NI-9263 4-Channel, 100 kS/s, 16-bit,  $\pm 10$  V, Analog Output Module [34],  
and
- NI-9215 4-Channel, 100 kS/s, 16-bit,  $\pm 10$  V Simultaneous Sampling Analog Input Module [35].



Figure 15. T/R module incorporated NI hardware (from [32]–[35]).

### 3. Modulator

The Analog Devices AD8346 is a silicon quadrature modulator that is normally used as the transmit modulator in digital systems such as code division multiple access (CDMA) and global satellite mobile (GSM) transceivers [36]. The modulator is designed to be used from 800 MHz to 2.5 GHz and is optimized for low power applications.

The modulator mounted in an evaluation board is shown in Figure 16. This configuration has been used in the preceding phase of this project. The previous measurements of AD8346 are covered in [12]–[13]. The device specifications appear in [37] and the evaluation set-up is described in [38].

The purpose of the measurements was to verify the possibility of using this commercially available component for phase shifting the RF signal. Figure 17 displays the typical complex phasor plane, where the in-phase ( $I$ ) and quadrature ( $Q$ ) signals each consist of two differential inputs ( $IP$ ,  $IN$ ,  $QP$  and  $QN$ , respectively).

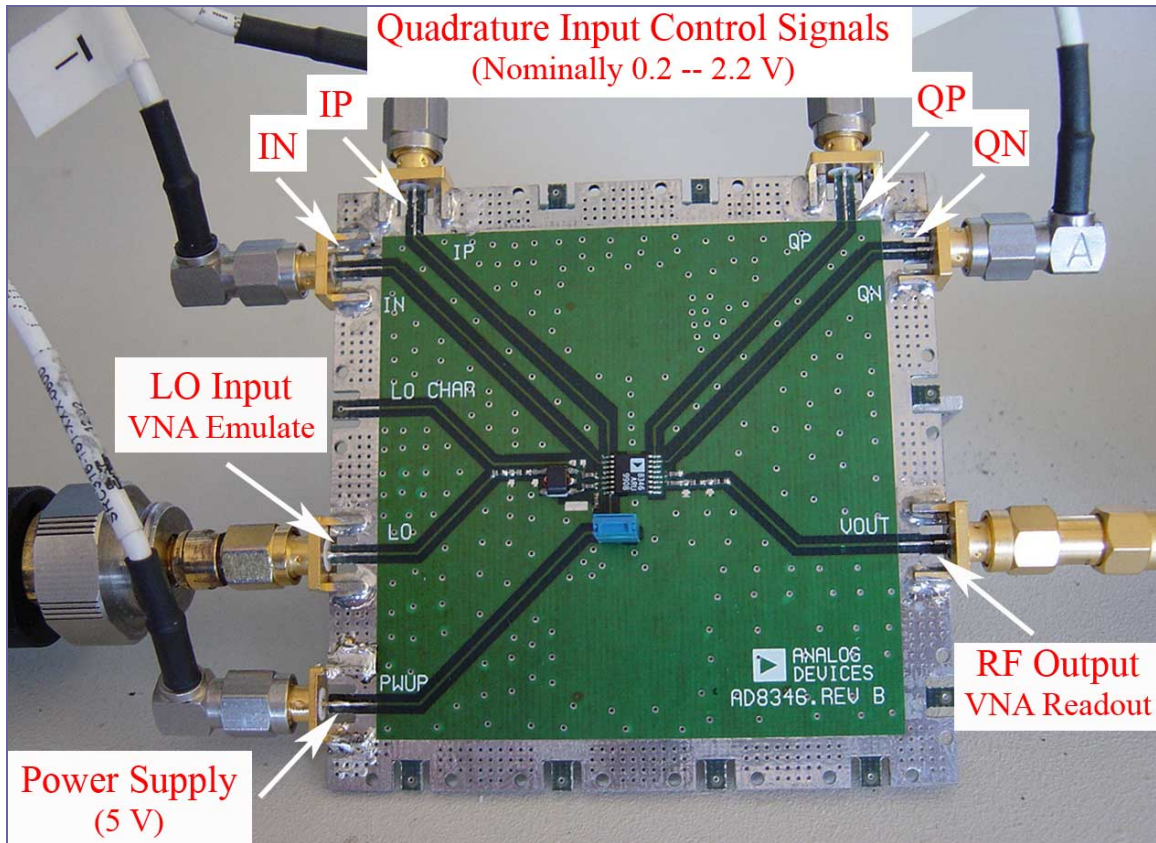


Figure 16. AD8346EVAL wiring connections.

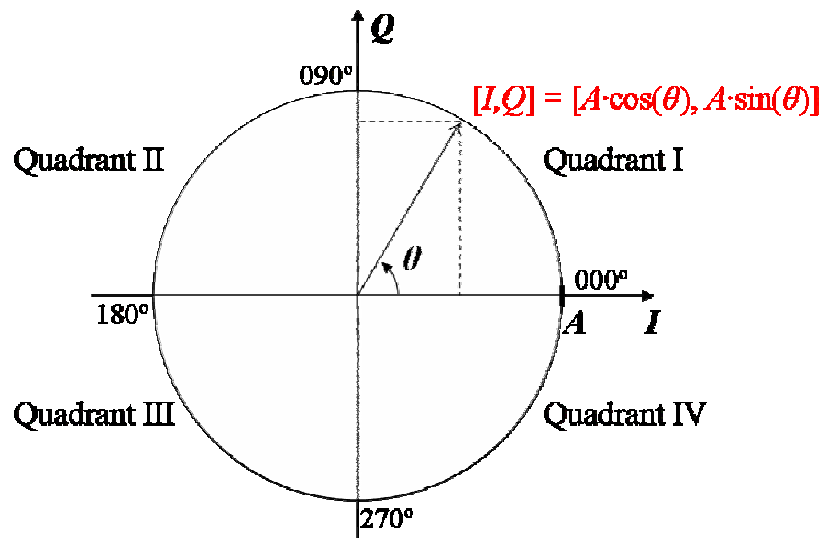


Figure 17. Typical complex phasor plane.



The phase shifting properties have been proven in both [12] and [13], however, the device was not set to operate in an optimal state, since two of the four quadrature input control signals were set to zero volts. According to [36], the modulator differential control signals should be dc-biased to approximately 1.2 V. The  $I$  and  $Q$  control signals are derived from Figure 17,

$$\begin{aligned} I(\theta) &= A \cos(\theta) \\ Q(\theta) &= A \sin(\theta) \end{aligned} \quad [V], \quad (1)$$

where  $A$  is the I/Q circle radius (i.e., the I/Q amplitude) and  $\theta$  is the desired phase setting. The modulator specification sheet in [36] states that the differential I/Q channel baseband inputs should be non-negative and have a maximum input of 2.5 V. Incorporating a dc-bias of 1.2 V, the differential I/Q channel baseband inputs were calculated using the following relations,

$$\begin{aligned} IP(\theta) &= 1.2 + \frac{1}{2} I(\theta), \\ IN(\theta) &= 1.2 - \frac{1}{2} I(\theta), \\ QP(\theta) &= 1.2 + \frac{1}{2} Q(\theta), \\ QN(\theta) &= 1.2 - \frac{1}{2} Q(\theta), \end{aligned} \quad [V] \quad (2)$$

where  $I(\theta)$  and  $Q(\theta)$  are given by Equations (1). Using the relations given in Equations (2), the maximum differential input is 2.4 V for an I/Q circle radius of 1.2 V.

In preparation for using the components in the two initial T/R demonstration modules, two of the individual AD8346 boards were characterized using the quadrature input settings dc-biased to 1.2 V. A LabVIEW VI was created to calculate the quadrature baseband input values using Equations (1) – (2) and also to provide the device under test

the accurate input values dependent on the chosen I/Q differential amplitude. Table 2 displays a sample data set for an I/Q differential input values for 2.0 V, the corresponding modulator output phase measurements, and the subsequent measured phase error for modulator board 1.

The measurements for four differential amplitude settings resulted in the phase deviations presented in Figure 18 for the two modulator boards.

Desired Phase, $\theta_{set}$ [°]	$I(\theta)$ [V]	$Q(\theta)$ [V]	$IP(\theta)$ [V]	$IN(\theta)$ [V]	$QP(\theta)$ [V]	$QN(\theta)$ [V]	Measured Phase $\theta_{meas}$ [°]	Phase Error $\Delta\theta$ [°]
0	2.000	0.000	2.200	0.200	1.200	1.200	0.0	0.0
10	1.970	0.347	2.185	0.215	1.374	1.026	9.8	-0.2
20	1.879	0.684	2.140	0.260	1.542	0.858	19.5	-0.5
30	1.732	1.000	2.066	0.334	1.700	0.700	29.2	-0.8
40	1.532	1.286	1.966	0.434	1.843	0.557	38.9	-1.1
50	1.286	1.532	1.843	0.557	1.966	0.434	48.7	-1.3
60	1.000	1.732	1.700	0.700	2.066	0.334	58.5	-1.5
70	0.684	1.879	1.542	0.858	2.140	0.260	68.6	-1.4
80	0.347	1.970	1.374	1.026	2.185	0.215	78.8	-1.2
90	0.000	2.000	1.200	1.200	2.200	0.200	89.3	-0.7
100	-0.347	1.970	1.026	1.374	2.185	0.215	100.0	0.0
110	-0.684	1.879	0.858	1.542	2.140	0.260	110.8	0.8
120	-1.000	1.732	0.700	1.700	2.066	0.334	121.7	1.7
130	-1.286	1.532	0.557	1.843	1.966	0.434	132.5	2.5
140	-1.532	1.286	0.434	1.966	1.843	0.557	143.2	3.2
150	-1.732	1.000	0.334	2.066	1.700	0.700	153.6	3.6
160	-1.879	0.684	0.260	2.140	1.542	0.858	163.8	3.8
170	-1.970	0.347	0.215	2.185	1.374	1.026	173.7	3.7
180	-2.000	0.000	0.200	2.200	1.200	1.200	-176.7	3.3
190	-1.970	-0.347	0.215	2.185	1.026	1.374	-167.3	2.7
200	-1.879	-0.684	0.260	2.140	0.858	1.542	-158.1	1.9
210	-1.732	-1.000	0.334	2.066	0.700	1.700	-149.1	0.9
220	-1.532	-1.286	0.434	1.966	0.557	1.843	-140.1	-0.1
230	-1.286	-1.532	0.557	1.843	0.434	1.966	-131.0	-1.0
240	-1.000	-1.732	0.700	1.700	0.334	2.066	-121.8	-1.8
250	-0.684	-1.879	0.858	1.542	0.260	2.140	-112.4	-2.4
260	-0.347	-1.970	1.026	1.374	0.215	2.185	-102.7	-2.7
270	0.000	-2.000	1.200	1.200	0.200	2.200	-92.7	-2.7
280	0.347	-1.970	1.374	1.026	0.215	2.185	-82.4	-2.4
290	0.684	-1.879	1.542	0.858	0.260	2.140	-72.0	-2.0
300	1.000	-1.732	1.700	0.700	0.334	2.066	-61.4	-1.4
310	1.286	-1.532	1.843	0.557	0.434	1.966	-50.9	-0.9
320	1.532	-1.286	1.966	0.434	0.557	1.843	-40.5	-0.5
330	1.732	-1.000	2.066	0.334	0.700	1.700	-30.1	-0.1
340	1.879	-0.684	2.140	0.260	0.858	1.542	-19.9	0.1
350	1.970	-0.347	2.185	0.215	1.026	1.374	-9.9	0.1
360	2.000	0.000	2.200	0.200	1.200	1.200	0.0	0.0

Table 2. Quadrature modulator input settings and resulting phase error for modulator board 1 with a differential amplitude of 2.0 V (sample table).

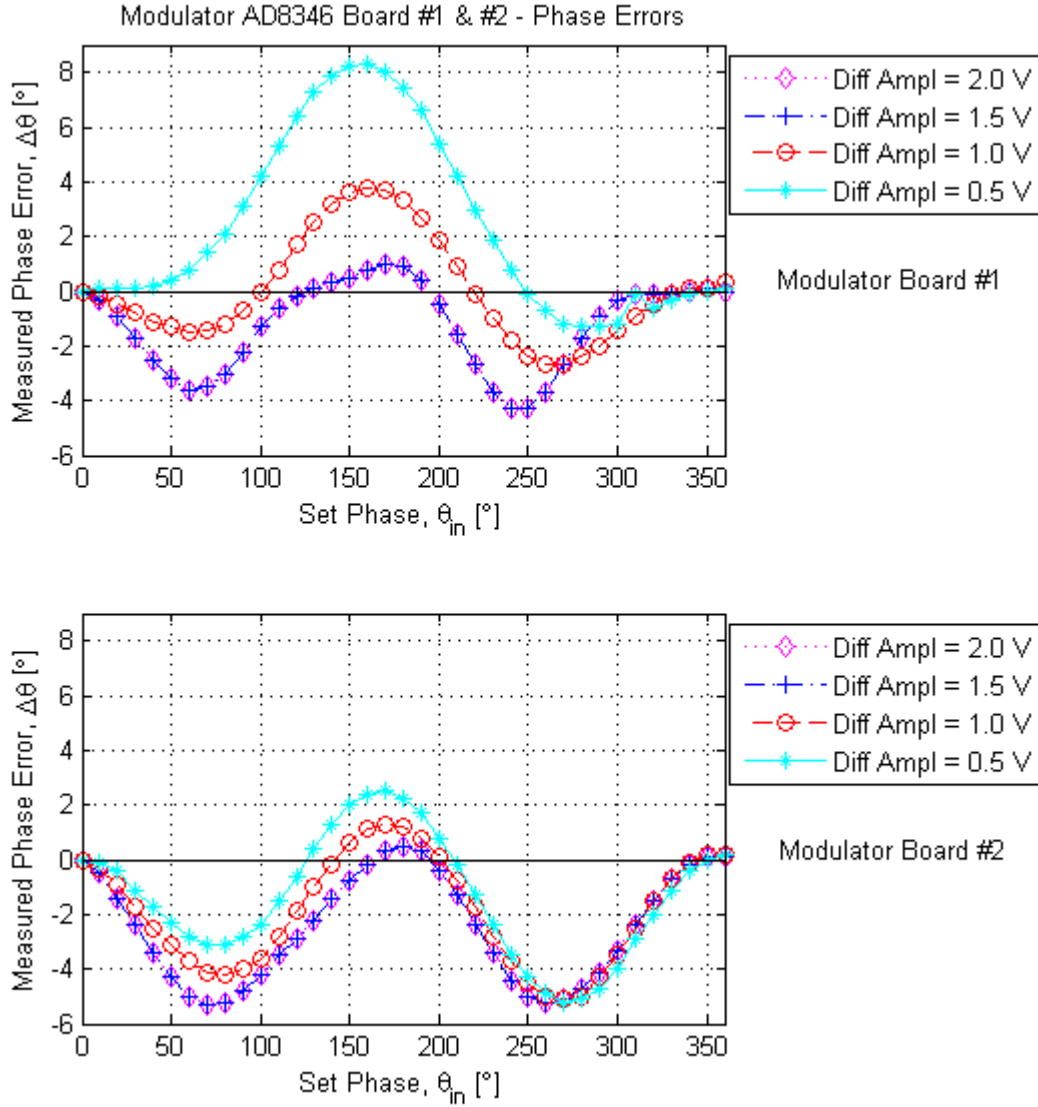


Figure 18. Measured phase error for four various differential amplitude settings.

Considering the data presented in Figure 18, no conclusion can be made as to whether the modulator phase error decreases inversely with the differential amplitude. However, for both modulator boards 1 and 2, for higher settings (i.e., 1.5 V and 2.0 V) of differential amplitudes, the resulting phase error was identical. The modulator average phase accuracy is deemed sufficient for the initial demonstration module application [39]. When measuring the remaining six boards for the complete 8-element demonstration

array, this requires a follow-up in order to establish the correct phase error versus differential amplitude relation.

The next parameter to be examined was the modulator RF output power and, more specifically, its relation to the input LO frequency, the set differential inputs, and the LO input power. Figure 19 is a representation of the device output power for five sets quadrature baseband inputs over the frequency range of 0.8 – 2.5 GHz. The modulator boards were supplied an in-phase set of differential inputs with  $Q(\theta)$  set to zero volts (i.e., with  $\theta$  equal to zero degrees) and a case of quadrature inputs with both  $I(\theta)$  and  $Q(\theta)$  being non-zero. This was to investigate whether the modulator RF output level is dependent on the I/Q settings.

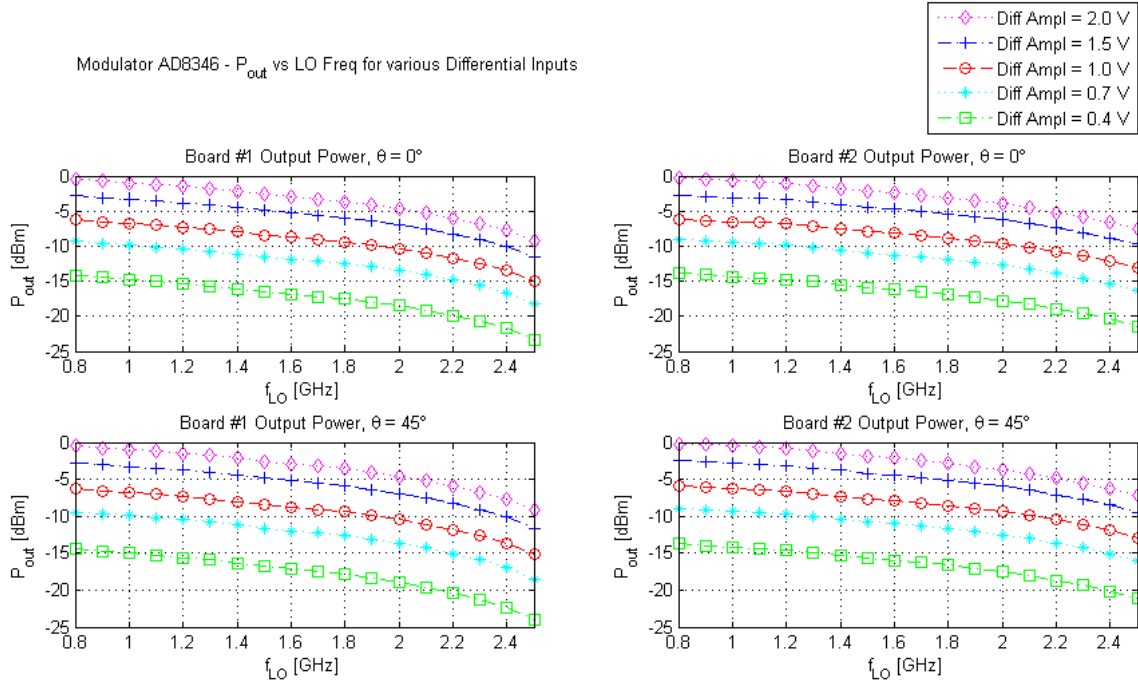


Figure 19. Modulator output power versus LO frequency.

As mentioned previously, the main point is the device response around 2.4 GHz. The measurements presented in Figure 19 indicate the modulator output power is dependent on the operating (LO) frequency, as well of the magnitude of the supplied

quadrature baseband inputs. However, there is no evidence of a dependency of the modulator operating point on the I/Q phase,  $\theta$ . For operation at 2.4 GHz, the expected modulator output, according to Figure 19, is around  $-10$  dBm for an I/Q magnitude of 1.5 V.

The modulator output power characteristics were also examined for a range of differential I/Q inputs at a set of fixed LO frequencies. In the data shown in Figure 20, the device's dependence on the I/Q magnitude appears more clearly. The LO frequencies were selected to represent the low, middle and high frequency regions for the modulator. The device, as mentioned before, is specified to operate within the range of 0.8 – 2.5 GHz. For this characterization, the frequencies were chosen as 1.0 GHz, 1.9 GHz (which reflects the operating conditions given in the specification sheet [36]), and 2.4 GHz, respectively.

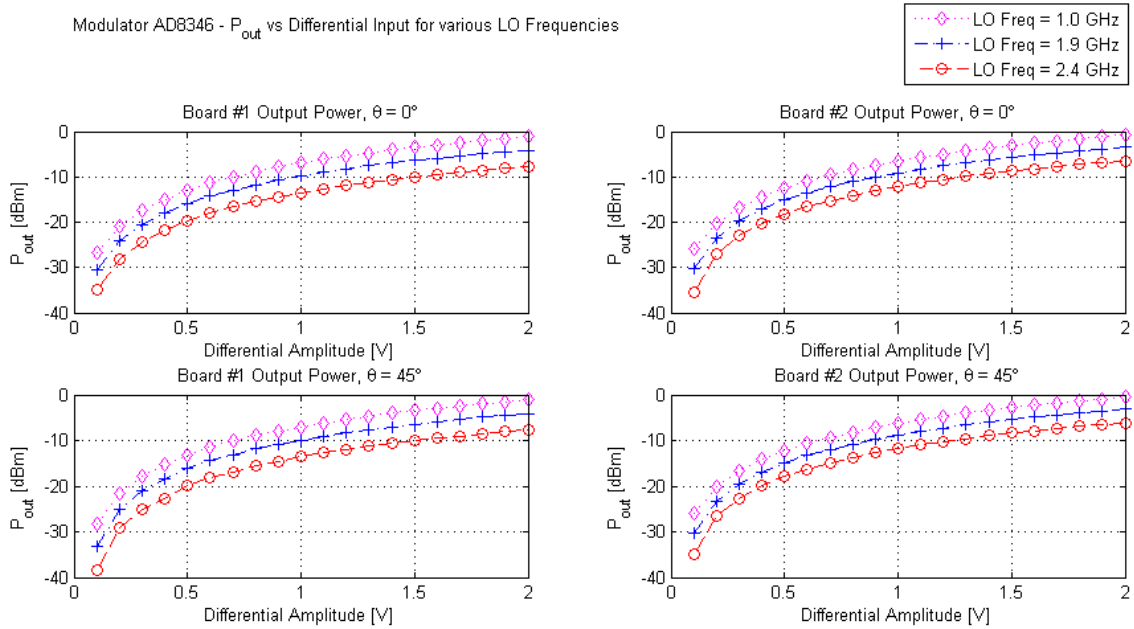


Figure 20. Modulator output power versus I/Q differential amplitude.

The modulator RF output level versus the differential amplitude is shown in Figure 20. From the graphs, there is apparently a fairly strong dependence of about 3.5 dBm/0.1 V<sub>DiffAmpl</sub> for I/Q magnitudes of below 0.5 V, whereas above 1.0 V the

dependence is weaker, at approximately 0.7 dBm/0.1 V<sub>DiffAmpl</sub>. Notably, when comparing the graphs in Figures 19 and 20, the modulator output power level differs 13 dB between differential amplitudes of 0.4 V and 2.0 V, regardless of the LO frequency. It is obvious that the AD8346 modulator should be set with differential amplitudes of more than 1.0 V. Again, the device output power operating at 2.4 GHz is given at about –10 dBm for an I/Q magnitude of 1.5 V.

The modulator output power as a function of the LO power was investigated. In Figure 21, the modulator RF output power is plotted versus the I/Q magnitude again, however, the graph shows the characteristics for a single LO frequency (2.4 GHz) and for four LO power levels. According to the AD8346 specification sheet [37], the LO drive level is specified as –12 to –6 dBm, with a maximum rating of +10 dBm. Figure 21 shows the output levels for three LO drive levels within the operating specification (–11.79 dBm, –8.82 dBm and –6.05 dBm), as well as one at the maximum power level the VNA can deliver at 2.4 GHz (which is –2.8 dBm at the VNA power output setting “+9 dBm”). This measurement was only conducted for one of the two modulator boards (board 1).

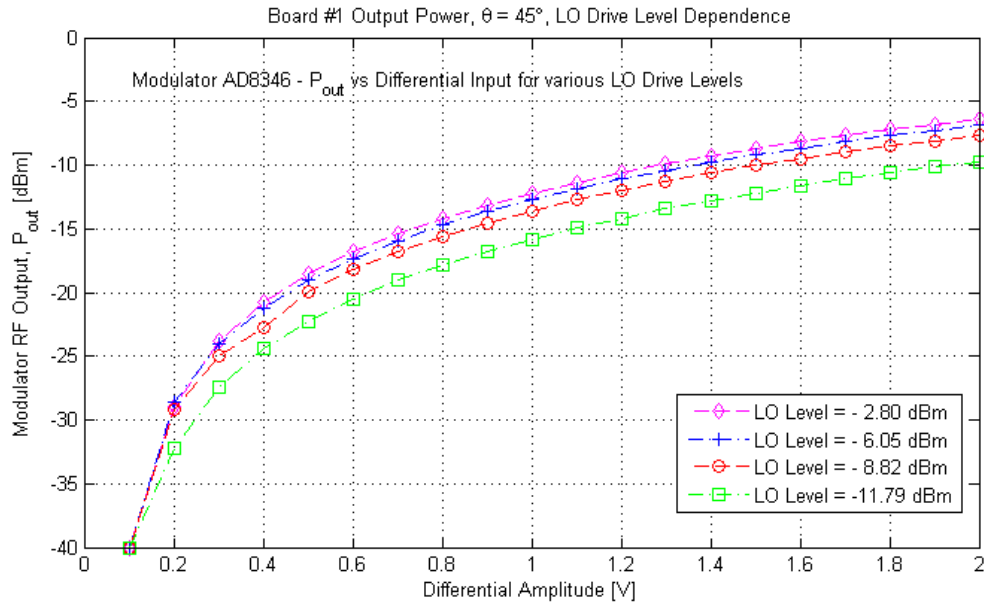


Figure 21. Modulator output power for various LO drive levels.

From the plot in Figure 21, it is evident that there is approximately 6 dB higher RF output when operating the device in the upper region of the specified LO drive level range. The 6 dB difference is present regardless of the magnitude of the differential inputs. In order to guarantee maximum RF output power from the AD8346 modulator, the device has to be fed with a sufficiently strong LO signal.

#### 4. Low-Power Amplifier

The Low-Power Amplifier (LPA) and the Low-Noise Amplifier (LNA) described later in this chapter are from RF Bay, Inc. In addition to complying with the electrical requirements, they also feature the benefit of the mechanical design of the demonstration T/R module, which is having the same physical size and shape.

The selected LPA model, LPA-4-14, is depicted in Figure 22, and its main specifications are listed in Table 3 [40].



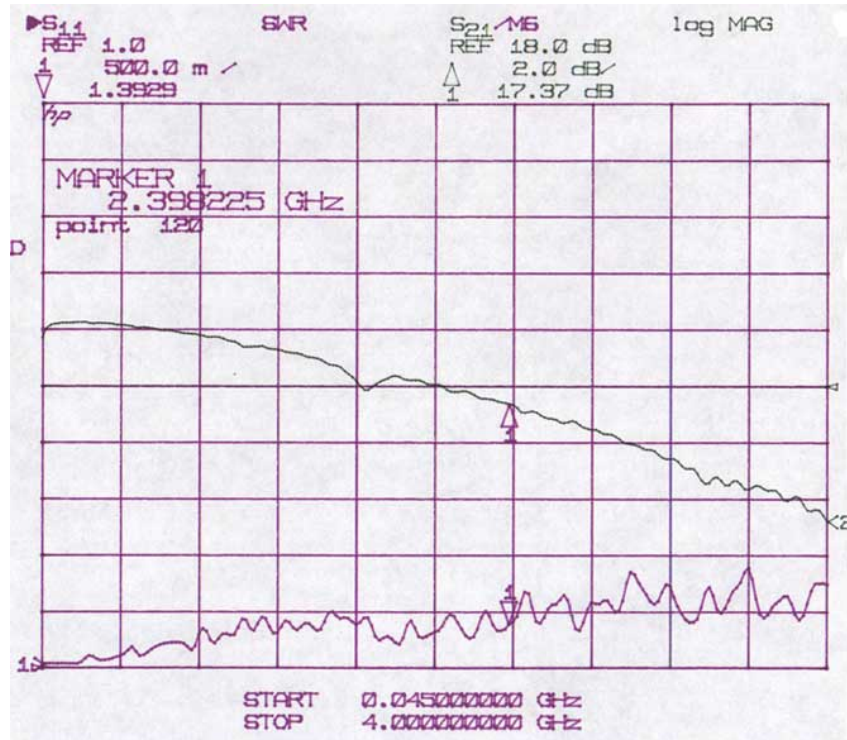
Figure 22. Low-power amplifier LPA-4-14 from RF Bay, Inc.



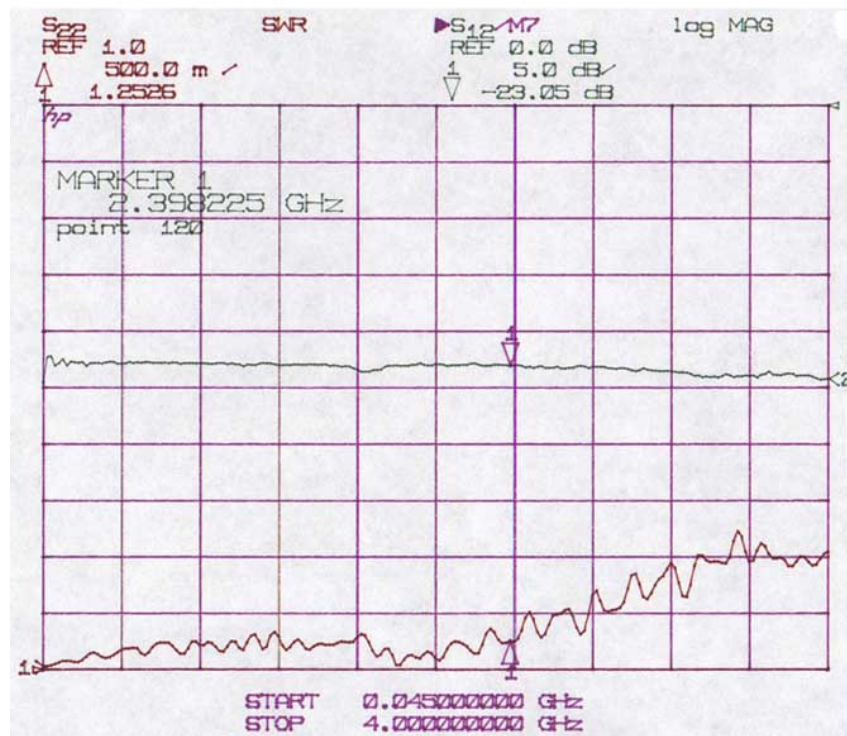
Parameter	Specification	Unit	Comments
Frequency Range	10 – 4,000	MHz	--
Gain, S21	18.0	dB	From graph, at 2.4 GHz
P1dB	+18.5	dBm	At 2,000 MHz
Noise Figure	+3.5	dB	At 2,000 MHz
Isolation, S12	–22.8	dB	From graph, at 2.4 GHz
Input VSWR, S11	1.3:1	--	From graph, at 2.4 GHz
Output VSWR, S22	1.4:1	--	From graph, at 2.4 GHz
RF Input Power	+15	dBm	Absolute Maximum Rating

Table 3. Subset of the LPA-4-14 specifications.

The verification of the device performance is limited to measuring the S-parameters. The device was connected to the VNA S-parameter test set, and read-outs for the two initially purchased amplifiers are presented in Figures 23 and 24, respectively.

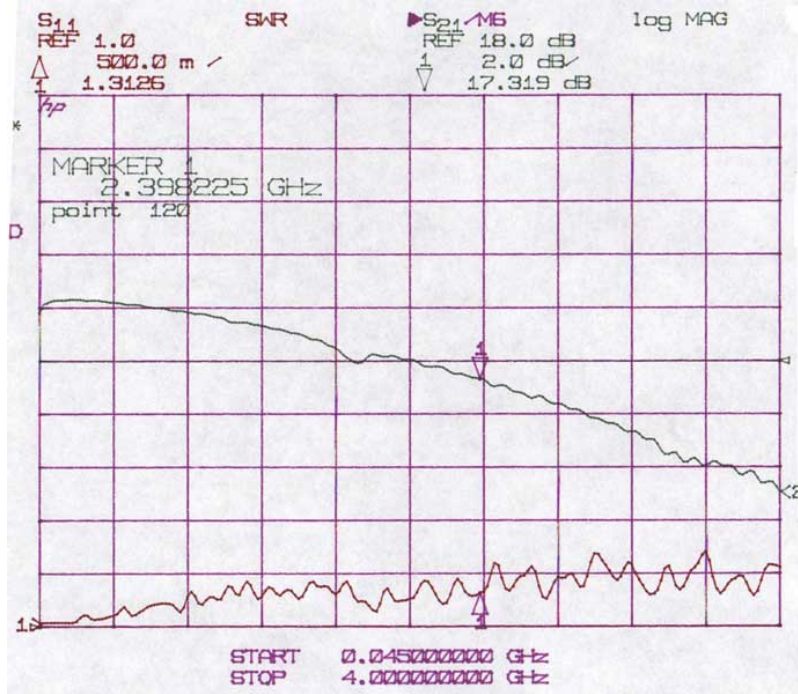


(a) Input Reflection Coefficient ( $S_{11}$ )  
Forward Transmission Gain ( $S_{21}$ )

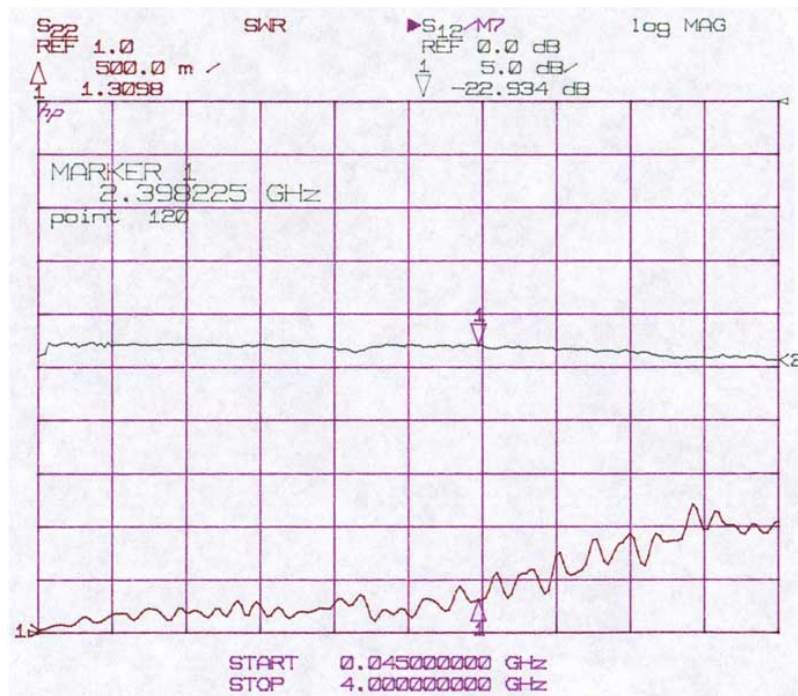


(b) Output Reflection Coefficient ( $S_{22}$ )  
Reverse Transmission Gain ( $S_{12}$ )

Figure 23. Measured S-parameters of LPA-4-14 No. 1, SN 11062823  
(a)  $S_{11}$  and  $S_{21}$  (b)  $S_{22}$  and  $S_{12}$ .



(a) Input Reflection Coefficient (S11)  
Forward Transmission Gain (S21)



(b) Output Reflection Coefficient (S22)  
Reverse Transmission Gain (S12)

Figure 24. Measured S-parameters of LPA-4-14 No. 2, SN 11062824  
(a) S11 and S21 (b) S22 and S12.

In the plots, the markers are set to the operating frequency of the T/R module (2.4 GHz). The measured S-parameter values and the specified values from the manufacturer are listed in Table 4.

Parameter	Specified	Measured at 2.4 GHz		Unit	Comparison vs. specification
		SN 11062823	SN 11062824		
S11, Input Reflection Coeff.	1.3:1	1.39	1.31	--	<b>0.09/0.01 above</b>
S21, Forward Transm. Coeff.	17.5	17.37	17.32	dB	<b>0.13/0.18 dB below</b>
S12, Reverse Transm. Coeff.	-22.8	-23.05	-22.93	dB	Exceeds spec
S22, Output Refl. Coeff.	1.4:1	1.25	1.31	--	Exceeds spec

Table 4. Specified and measured S-parameters for LPA-4-14.

The LPA device will be used on the transmit side of the T/R module; hence, the noise figure is not as critical as it would be on the sensitive receiving end. The amplifier has a wide bandwidth (10 – 4,000 MHz), and the specifications at the operating point (2.4 GHz) have to be estimated from the graphs in [40]. Neither of the two individual LPA devices fulfilled the specified values for S11 or S21 (marked with **bold red text** in Table 4), however in both cases the performance is deemed sufficient for the initial experiments.

The chosen low-power amplifier circuit is optimized for small signals. The P1 value (i.e., the power level where device no longer is capable of providing a linear amplification) is specified as 20 dBm. This limit is not significant in the T/R module application since the modulator output power at 2.4 GHz is limited to about -6 dBm (see Figures 19 – 20).

Another characteristic of interest regarding any amplifier is the amount of power dissipated. In the demonstration application, the LPA will be mounted to the wall on the inside of the T/R module enclosure. The enclosure is an aluminum box that will act as a heat sink, but since no other cooling function is being considered at this point, the power dissipated (i.e., the heat generated) by the LPA is especially crucial. The voltage

specified for this device is at +12 V. The measured currents and the corresponding power consumption are listed in Table 5.

Parameter	SN 11062823	SN 11062824
Voltage [ $V_{dc}$ ]	+12	+12
Current [ $mA_{dc}$ ]	88	91
Total Power consumed [W]	1.056	1.092

Table 5. LPA-4-14 power consumption.

The measured amplifier power consumption is at a level that will not affect the other module components negatively. The module chassis is intended to transfer most of the heat generated inside; hence, the inter-module spacing must be sufficient to allow air flow. This issue will be addressed in a later section.

## 5. Circulator

The circulators for the T/R modules were obtained from DiTom Microwave, Inc. The D3C2040 circulator, depicted in Figure 25, is a single junction device specified for an octave frequency band at 2– 4 GHz [41].

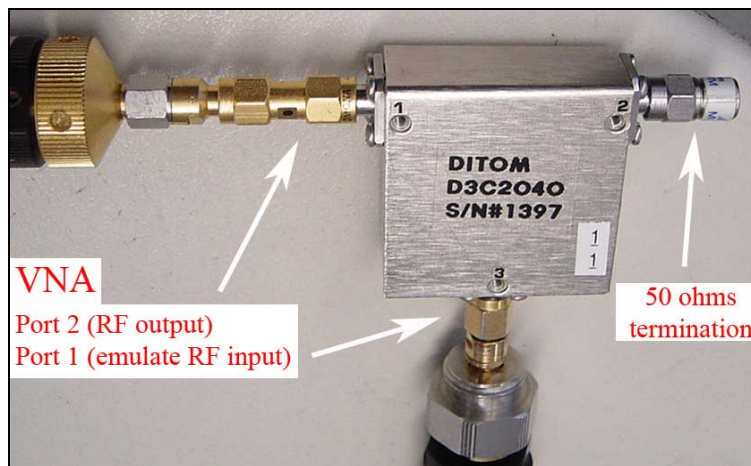


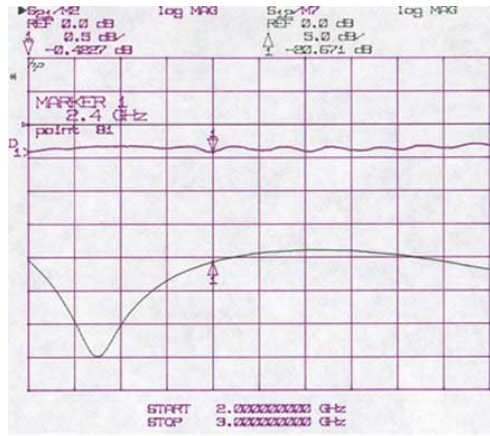
Figure 25. DiTom single junction circulator D3C2040.

The circulator insertion loss and the isolation were measured using the VNA S-parameter test set with the third circulator port terminated in a  $50\ \Omega$  load. Figure 25 shows the case of measuring from circulator port 3 to port 1, with port 2 terminated in a matched load. A list of the device specifications and the measured data can be found in Table 6. The plots for all three port configurations appear in Figure 26, where the plotter marker was set at 2.4 GHz.

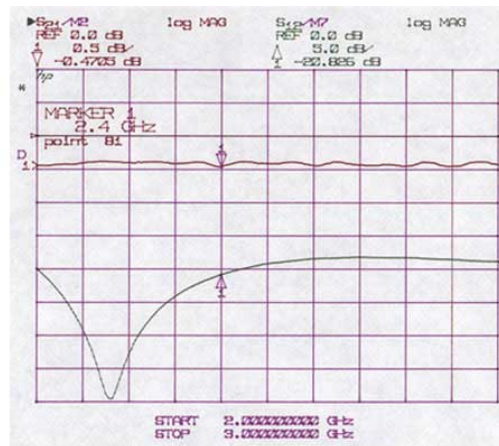
Parameter	Specified	Measured at 2.4 GHz				Unit
		Circ#	Port 1 $\rightarrow$ 2	Port 2 $\rightarrow$ 3	Port 3 $\rightarrow$ 1	
Isolation ( $-S_{12}$ )	20 Typically	1	<b>20.671</b>	20.644	20.558	dB
	18 Minimum	2	<b>20.826</b>	20.027	18.907	
Insertion Loss ( $-S_{21}$ )	0.40 Typically	1	0.423	0.433	0.397	dB
	0.50 Maximum	2	0.471	0.463	0.465	

Table 6. Specified and measures parameters for D3C2040 circulator (**bold blue text** highlights the highest obtained isolation for each circulator).

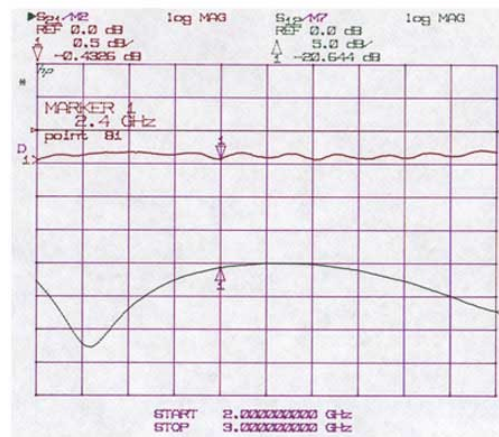




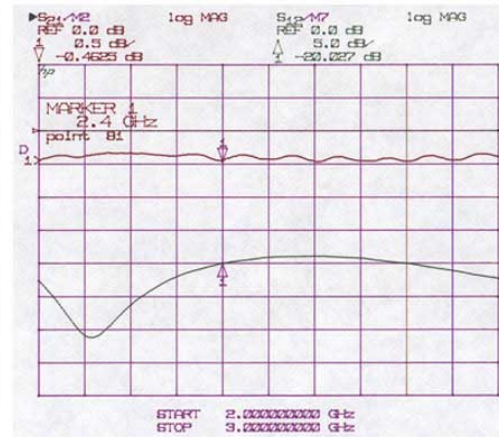
(a) Circulator 1, Port 1 → 2



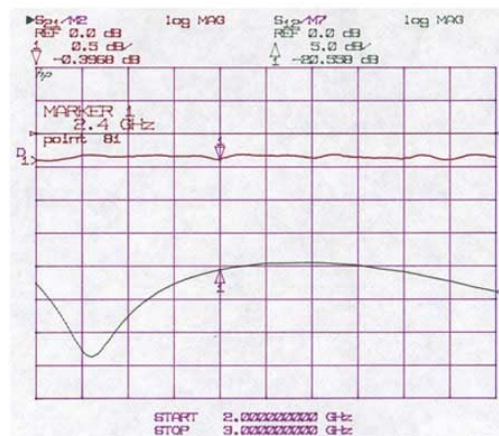
(d) Circulator 2, Port 1 → 2



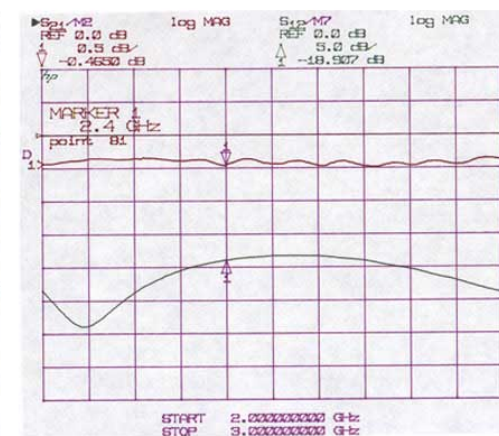
(b) Circulator 1, Port 2 → 3



(e) Circulator 2, Port 2 → 3



(c) Circulator 1, Port 3 → 1



(f) Circulator 2, Port 3 → 1

Figure 26. Measured values of S<sub>21</sub> and S<sub>12</sub> for the two DiTOM D3C2040 circulators.

A review of the measured data displayed in Figure 26 and Table 6, confirms that all data are within the vendor specifications of the device. For the T/R module, as for any radar application, a major concern regarding the circulator is keeping the isolation as high as possible from the transmitter to the receiver side of the radar system. Low isolation can cause problems on the receive side when the leakage signal from the transmitter masks a weak received RF signal.

A very high isolation between the two ports is not only difficult and expensive to achieve, but often will not suffice alone for a normal radar system, since there generally are several orders of magnitude difference between signal levels on the transmit (Tx) and receive (Rx) sides. Other than employing two separate antennas with high isolation between Tx and Rx, some type of software or hardware cancellation function will be needed. This problem is addressed further in the proposed future work in Chapter V.

For both the circulators at hand and as highlighted with **bold blue text** in Table 6, the highest isolation was acquired from port 2 into port 1. From a mechanical perspective, this is favorable since the T/R module layout to and from the antenna element will be simplified with symmetry between the transmit and receive signals wiring, as in Figure 27.

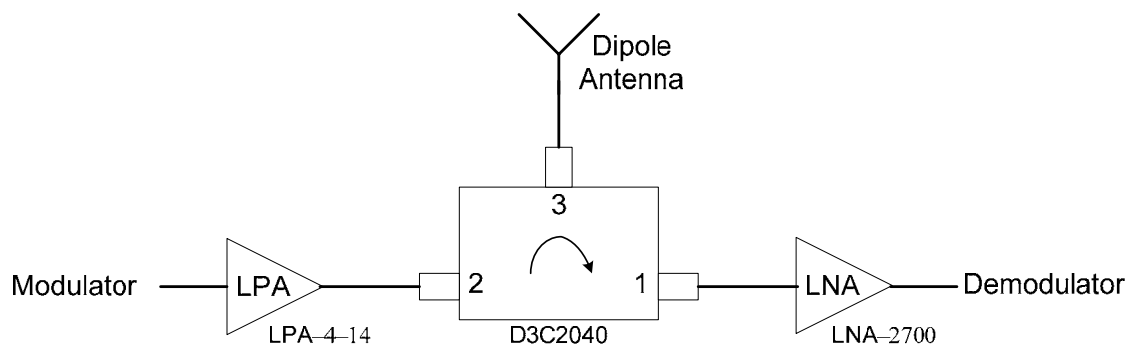


Figure 27. Principal mechanical layouts of the circulator connections.

In conclusion, the circulators exceed the vendor specification both in terms of insertion loss and, more important, isolation. The circulator labeled as “1” (DiTom serial



number 1397) has an isolation of 20.7 dB, whereas circulator “2” (S/N#1396) it is 20.8 dB.

## 6. Dipole Antenna Element

The T/R modules will utilize printed circuit dipole antennas developed previously for a related project. The microstrip dipoles were custom designed by Prof. D. C. Jenn and fabricated by Cirexx Corporation with a nominal operating frequency of 2.4 GHz and a return loss of over 15 dB. A dipole mounted in a ground plane and one standing alone is shown in Figure 28.



Figure 28. Two dipole elements, of which one is mounted in a ground plane.

The dipoles were originally used for a twenty-four element array antenna presented in [12], where the elements were characterized by return loss, i.e., a measure of the antenna match to the 50  $\Omega$  impedance of the system. The next step is the analysis of these figures using definitions of some fundamental microwave parameters such as voltage standing wave ratio (VSWR), reflection coefficients ( $\Gamma$ ,  $\rho$ ,  $S_{ii}$ ), return loss (RL) and mismatch loss (ML) given in [42] and [43]. The parameter definitions are:

$$\Gamma = \frac{E_r}{E_i}, \quad (3)$$

$$\rho = |S_{ii}| = |\Gamma|, \quad i \in [1, 2], \quad (4)$$

$$\text{VSWR} = \frac{|E_{\max}|}{|E_{\min}|} = \frac{1 + \rho}{1 - \rho}, \quad (5)$$

$$\rho = \frac{\text{VSWR} - 1}{\text{VSWR} + 1}, \quad (6)$$

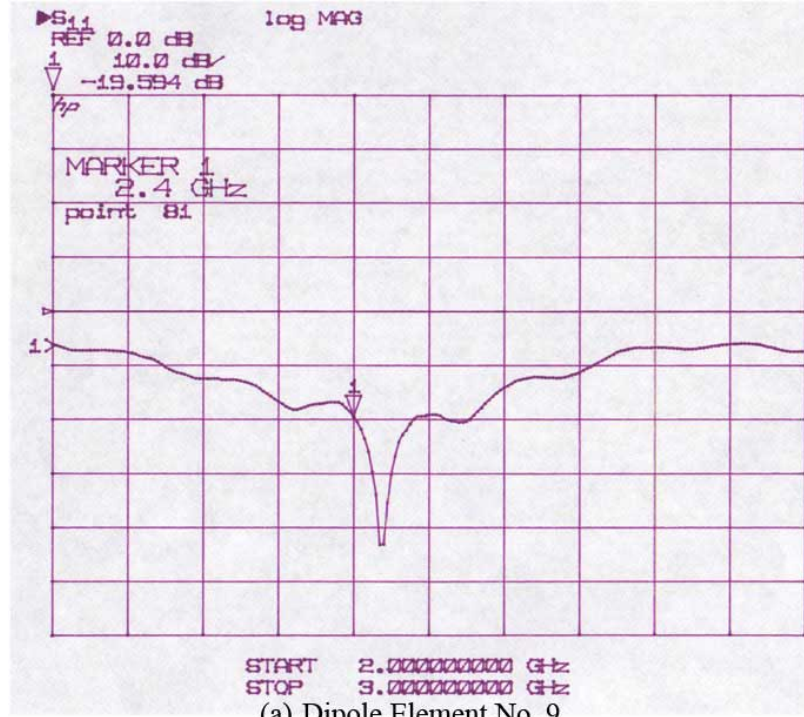
$$\text{RL} = -20 \cdot \log_{10}(\rho), \quad (7)$$

and finally

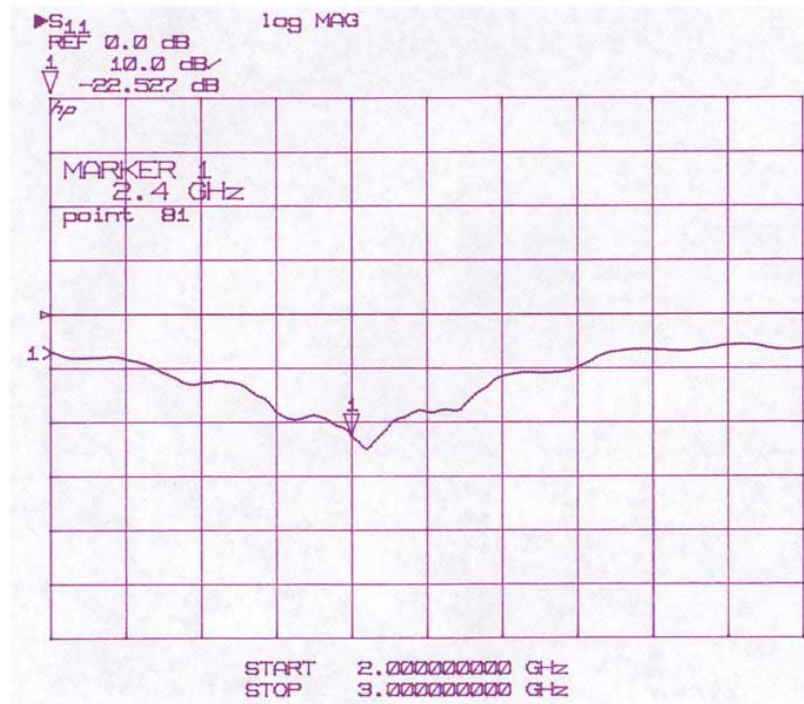
$$\text{ML} = -10 \cdot \log_{10}(1 - \rho^2), \quad (8)$$

where  $E_i$  is the incident and  $E_r$  the reflected phasor fields, and  $E_{\max}$  and  $E_{\min}$  the maximum and minimum voltages of the standing wave, respectively.

Two of the dipole elements (initial element identification numbers 9 and 22) were dismantled from the original project's random antenna array. The two dipoles were re-measured (verifying the previous results) for return loss (RL) using the VNA S-parameter test set. When conducting the measurement, the dipole elements were mounted in the original machined 1/4 in thick aluminum ground plane. The resulting S11 data is displayed in Figure 29.



(a) Dipole Element No. 9



(b) Dipole Element No. 22

Figure 29. Dipole element return loss ( $|S_{11}|$ ) measured mounted in the ground plane.

The marker is set at 2.4 GHz and  $|S_{11}|$  is presented in dB (the return loss according to Equation (7) above). The return loss is 19.6 dB for dipole element number 9 and 22.5 dB for number 22. From Equation (7), the reflection coefficient,  $\rho$ , is 0.105 and 0.075, respectively. From Equation (8), the corresponding mismatch loss (i.e., the ratio reflected power) of the two antenna elements is 0.05 dB and 0.03 dB, in that order. Both elements exceed the dipole design criteria of  $RL = 15$  dB, which is equivalent to  $\rho = 0.18$  dB and  $ML = 0.14$  dB. The values of  $RL$  and the subsequent mismatch loss are more than sufficient for the demonstration application.

Individual element 9 was measured twice for  $S_{11}$  to investigate ground plane effects. In the first measurement, the dipole was mounted in a simple ground plane as shown in Figure 28, followed by a test with no ground plane. The return loss was 23.4 dB and 20.8 dB, corresponding to a reflected power at the dipole input of 0.02 dB and 0.04 dB, respectively. Thus, both these dipole configurations had lower return loss than when the element was mounted in the original ground plane presented in [12]. These results are attributed to the width of the ground plane slot. A thin slot is desirable for mounting purposes, but a thin slot also disturbs the field in the space above the microstrip lines.

The dipole antenna element pattern, and consequently the gain are of interest in the demonstration radar system power budget analysis. The power budget calculation, together with a description of the NPS anechoic chamber, is covered in Section IV C1.

The element gain,  $G_{dipole}$ , was measured in the chamber using a comparative method. When the two antennas, the reference transmitting antenna and the device under test (DUT), have mainlobes aligned maximum power is received. Prior to illuminating the printed circuit dipole element mounted in a ground plane (see Figure 28), the receiving antenna is substituted by another reference horn antenna (Narda 645) with a known gain.

The element patterns for vertical and horizontal polarizations shown in Figure 30(a) apply to the calibration set-up at 2.40 GHz. In Figure 30(b), the reference feed horn gain is 17.12 dB.

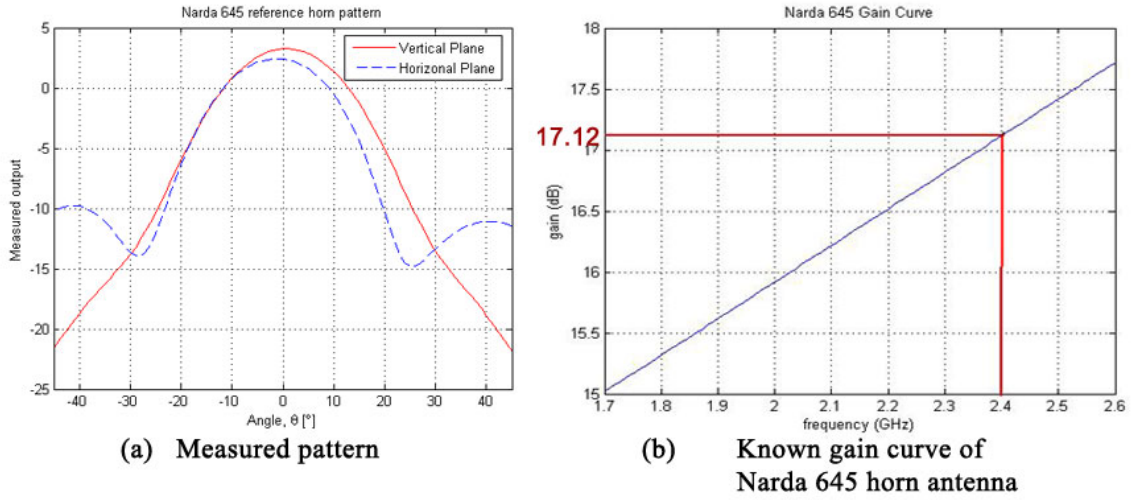


Figure 30. Reference horn pattern measurement (Narda 645).

The recorded maximum system transmission losses (S21) were 2.42 dB for vertical and 3.27 dB for horizontal polarization, respectively. The average maximum value for the transmission loss using the reference horn antenna for the two polarizations is

$$\frac{2.42 + 3.27}{2} = 2.85 \text{ dB} . \quad (9)$$

This value corresponds to the 17.12 dB gain of the reference horn element.

The procedure was then repeated using the dipole element over a ground plane mounted on the rotating receiver pedestal. The printed dipole element was measured for frequencies 2.40, 2.45, and 2.50 GHz, with only a six tenths of a dB difference in measured average maximum values (−7.72 dB, −7.49, and −7.13 dB, respectively).

The measured element patterns for the printed dipole antenna mounted in a ground plane at 2.40 GHz are displayed in Figure 31.

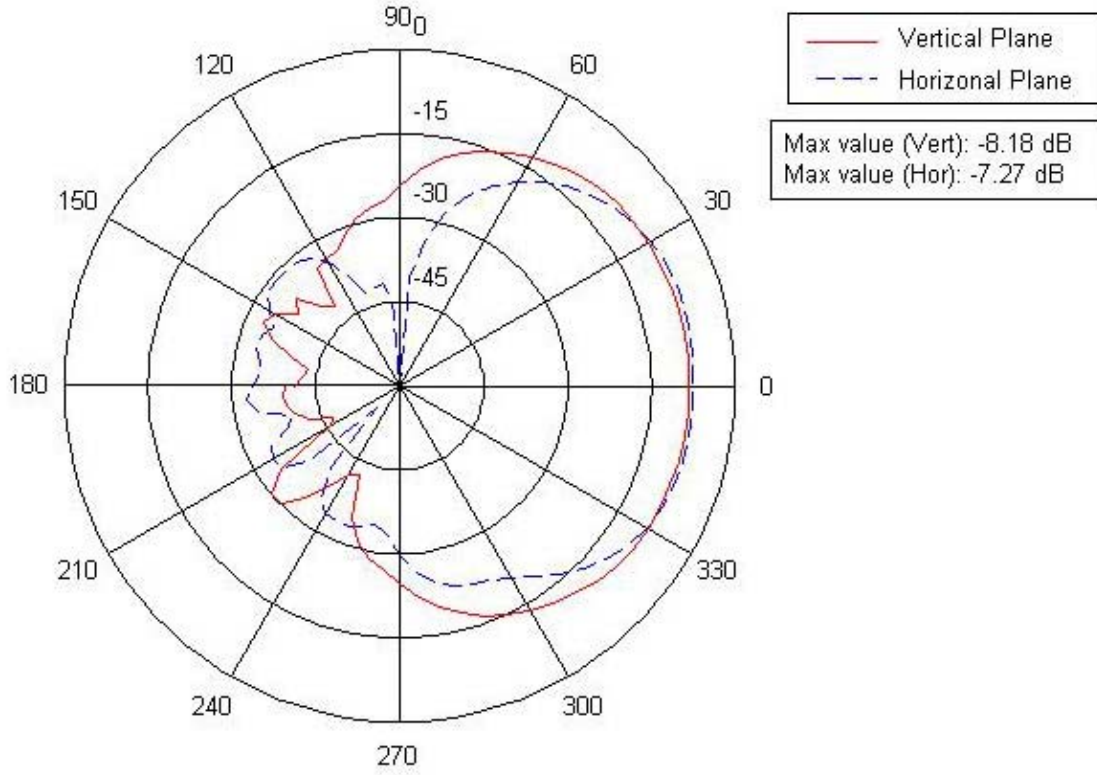


Figure 31. Dipole element pattern measurement measured at 2.40 GHz.

The average maximum pattern value for the received power for the two polarizations is

$$\frac{(-8.18) + (-7.27)}{2} = -7.72 \text{ dB} . \quad (10)$$

The gain of the printed circuit dipole antenna mounted in the ground plane compares to the reference measurement by

$$2.85 - (-7.72) = 17.12 - G_{dipole} , \quad (11)$$

and finally the dipole element gain is established at

$$G_{dipole} = 17.12 - 2.85 - 7.72 = 6.55 \text{ dB} . \quad (12)$$

## 7. Low-Noise Amplifier

The low-noise amplifier (LNA) was acquired from the same vendor as the LPA. The chosen model, LNA-2700, is displayed in Figure 32, and specifications are listed in Table 7 [44].



Figure 32. Low-noise amplifier LNA-2700 from RF Bay, Inc.

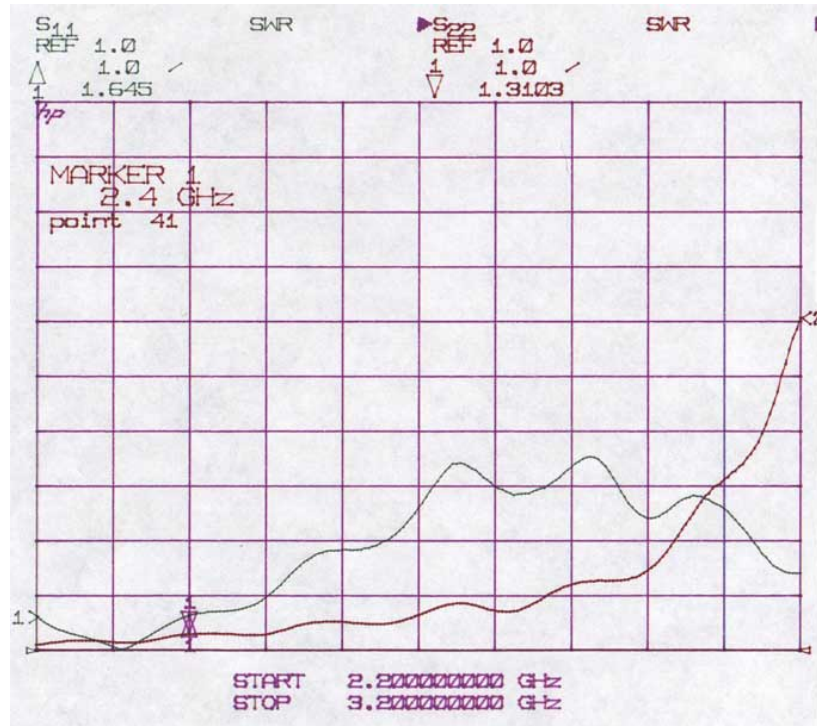
Parameter	Specification	Unit	Comments
Frequency Range	2.2 – 3.2	GHz	
Gain, S21	23	dB	From graph <sup>*</sup> , at 2.4 GHz
P1dB	+10	dBm	Over entire frequency range
Noise Figure	+1.7	dB	From graph <sup>*</sup> , at 2.4 GHz
Isolation, S12	–56	dB	From graph <sup>*</sup> , at 2.4 GHz
Input VSWR, S11	2.5:1	--	1.3:1 from graph <sup>*</sup> , at 2.4 GHz
Output VSWR, S22	1.5:1	--	1.2:1 from graph <sup>*</sup> , at 2.4 GHz
RF Input Power	+13	dBm	Absolute Maximum Rating

<sup>\*</sup>From graphs presented in [44]

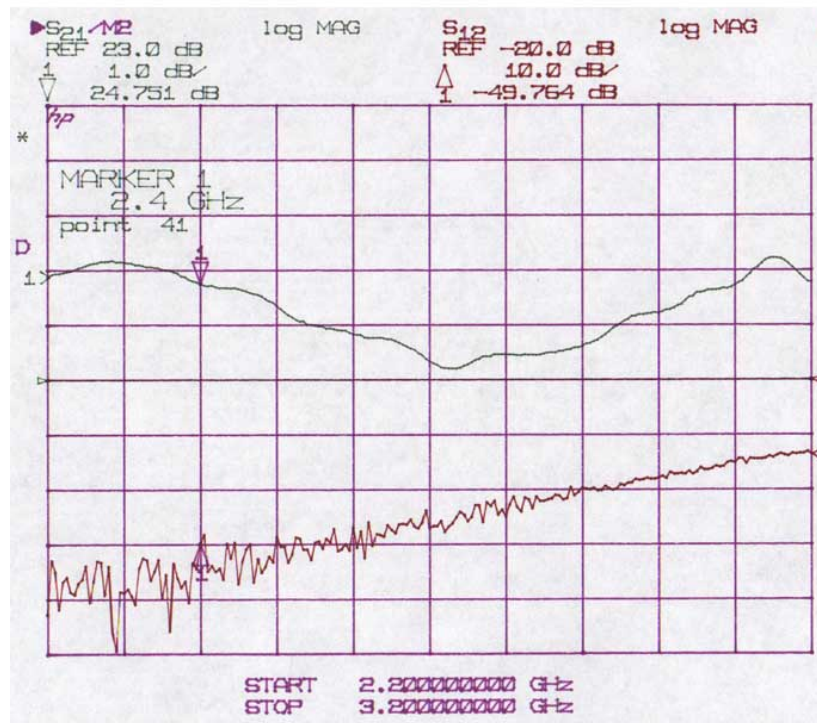
Table 7. Subset of the LNA–2700 specifications.

The verification of the LNA was conducted similarly to that for the LPA, and the resulting S–parameter plots for the two devices are displayed in Figures 33 and 34, respectively. The plotter marker is set to the intended operating frequency at 2.4 GHz.



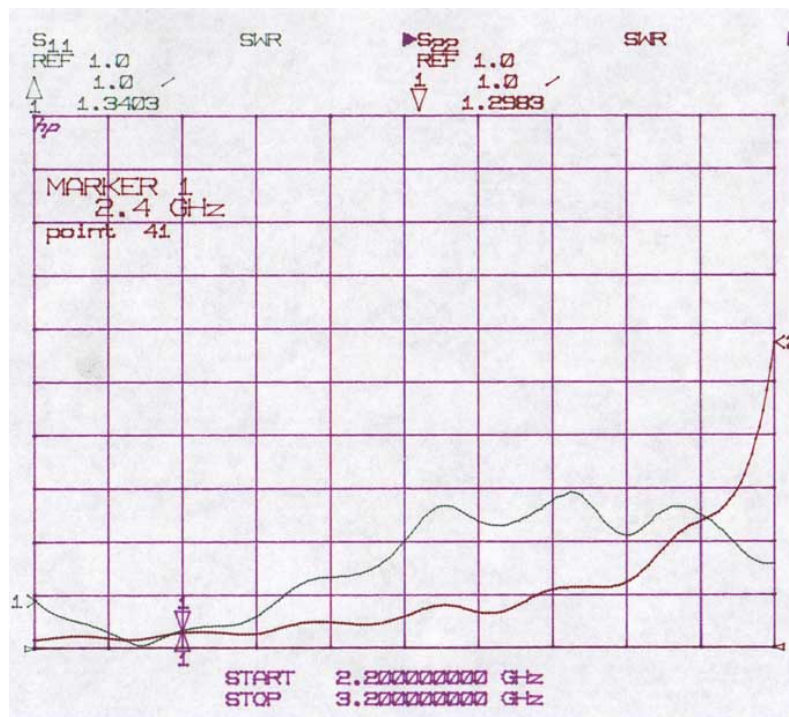


(a) Input Reflection Coefficient ( $S_{11}$ )  
Output Reflection Coefficient ( $S_{22}$ )

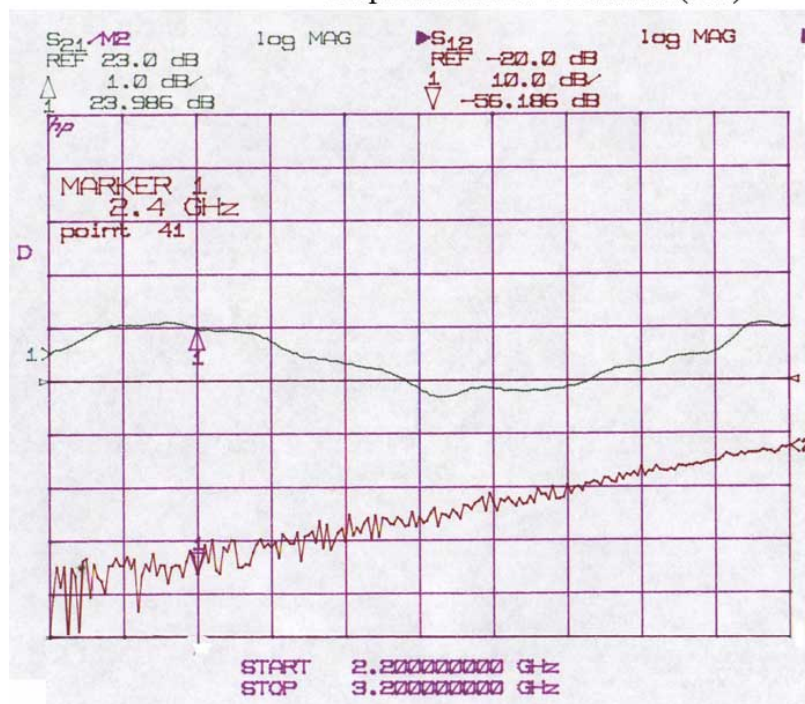


(b) Forward Transmission Gain ( $S_{21}$ )  
Reverse Transmission Gain ( $S_{12}$ )

Figure 33. Measured S-parameters of LNA-2700 No.1, SN 12062858  
(a)  $S_{11}$  and  $S_{22}$  (b)  $S_{21}$  and  $S_{12}$ .



(a) Input Reflection Coefficient ( $S_{11}$ )  
Output Reflection Coefficient ( $S_{22}$ )



(b) Forward Transmission Gain ( $S_{21}$ )  
Reverse Transmission Gain ( $S_{12}$ )

Figure 34. Measured S-parameters of LNA-2700 No.2, SN 12062859  
(a)  $S_{11}$  and  $S_{22}$  (b)  $S_{21}$  and  $S_{12}$ .

The specified ([44], see Table 7) and measured parameters of interest for the LNAs are summarized in Table 8.

Parameter	Spec.	Measured at 2.4 GHz		Unit	Comparison vs. specification
		SN 12062858	SN 12062859		
Input VSWR	2.5:1	1.645	1.340	--	Exceeds spec
Output VSWR.	1.5:1	1.310	1.298	--	Exceeds spec
S21, Forward Transm. Coeff.	23	24.75	23.99	dB	Exceeds spec
S12, Reverse Transm. Coeff.	-56	-49.76	-56.19	dB	6.24 above/Exceeds

Table 8. Specified and measured S-parameters for LNA-2700.

The measured values of the input VSWR, calculated and related parameters are listed in Table 9.

Amplifier/Parameter	Input VSWR	Reflection Coefficient Equation (6)	Return Loss Equation (7)	Mismatch Loss Equation (8)
SN 12062858	1.645 [-]	0.244 [-]	12.3 [dB]	0.27 [dB]
SN 12062859	1.340 [-]	0.145 [-]	16.8 [dB]	0.09 [dB]

Table 9. Measured and calculated VSWR related parameters for LNA-2700.

The LNA component will be situated on the receive side of the T/R module and will normally be handling low power RF signals. Thus, the device input VSWR must be low to maximize the power input to the amplifier. From Table 9, the corresponding mismatch loss for the two amplifiers is 0.27 dB and 0.09 dB, respectively. For the demonstration module with a CW signal, the LNA VSWR level will suffice.

The noise figure was not measured, but according to the data sheet [44], the typical noise figure of the device at 2.4 GHz is about 1.7 dB.

The chosen low-noise amplifier circuit is optimized for lower signals than the LPA-4-14 described previously. The P1 value for the LNA-2700 is specified as +10 dBm, with an absolute maximum RF input power rating of +13 dBm.

The supply voltage of the low-noise amplifier is specified at +12 V. The measured current draw and the corresponding power consumptions of the two LNAs are listed in Table 10. The power consumption of the LNA will add to the overall heat generated inside the T/R module.

Parameter	SN 12062858	SN 12062859
Voltage [ $V_{dc}$ ]	12	12
Current [ $mA_{dc}$ ]	55	46
Total Power consumed [W]	0.66	0.55

Table 10. LPA-4-14 power consumption.

## 8. Demodulator

The Analog Devices AD8347 demodulator evaluation board has previously been investigated and incorporated in the initial set-up leading to the demonstration study [13, 14, 17]. The AD8347 is a broadband (0.8–2.7 GHz) direct quadrature demodulator and is capable of direct down conversion of an RF signal to I/Q baseband components by mixing with the LO signal. The demodulator mounted on an evaluation board is displayed in Figure 35, and the specifications of device and the evaluation board are accessible at the Analog Device's website [45]–[46].



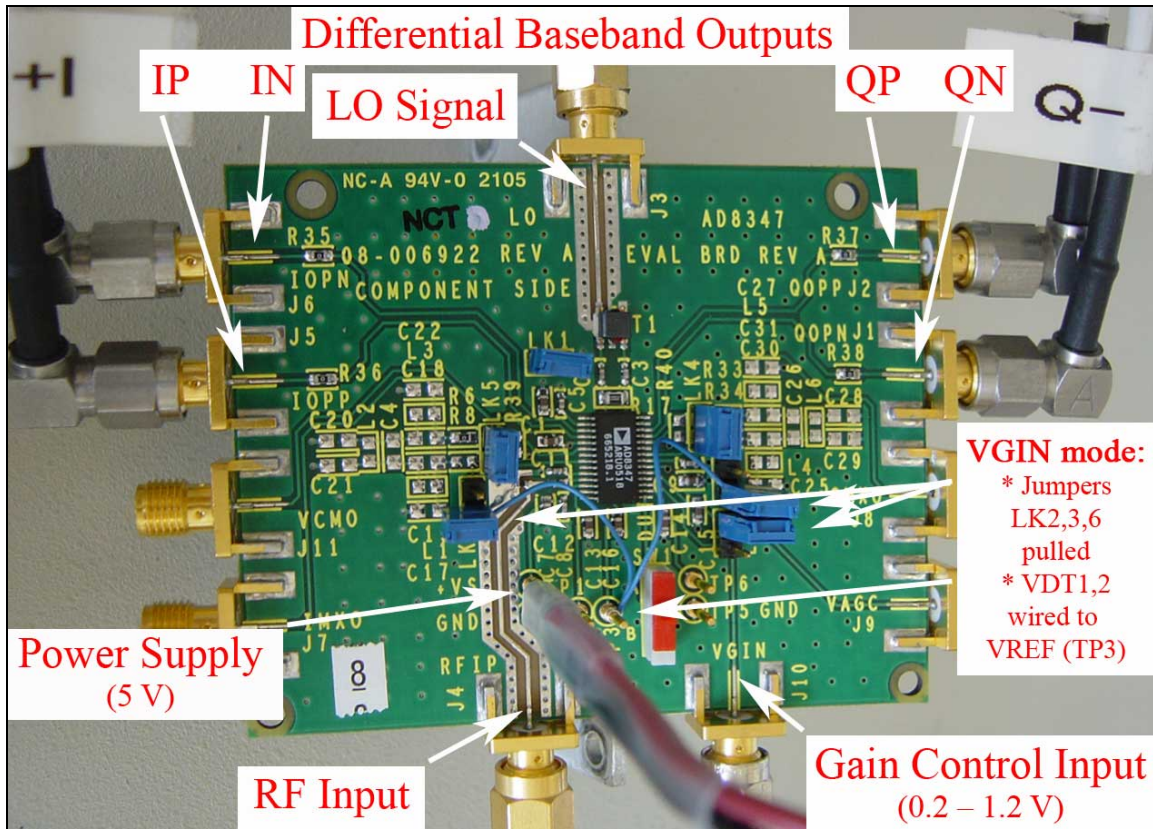


Figure 35. AD8347EVAL wiring connections and mode settings.

The demodulator is equipped with RF and baseband automatic gain control (AGC) amplifiers, and is suitable for use in communications receivers. The analysis of the device indicated that in the AGC mode, the I/Q-channel differential baseband output tended to quantize the phase to values on the axes instead of spreading them evenly around the I/Q circle, when the phase is altered. This behavior is likely attributed to the fact that the device originally was designed for communication applications, and more specifically for some quadrature phase-shift keying (QPSK) implementation.

The demodulator evaluation board (EVAL-AD8347EB) schematic is shown in Figure 36. In order to operate the demodulator with a linear phase response, the device had to be set for VGIN mode at values presented in Table 11, which all are displayed in Figure 35.

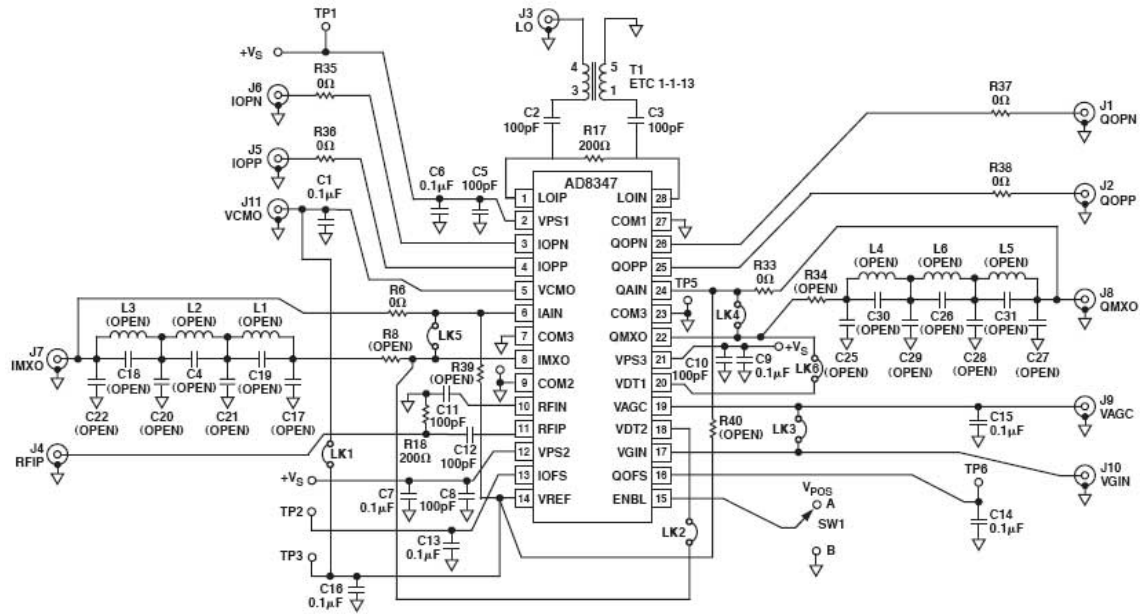


Figure 36. AD8347 demodulator evaluation board schematic (From [46]).

Parameter	Measures taken	Comments
Jumper LK2	Opened	Disconnecting the I-channel baseband mixer/VGA output (IMXO, pin 8) from device on-board detector input (VDT2, pin 18)
Jumper LK3	Opened	Disconnecting the internally generated automatic gain control voltage output (VAGC, pin 19) from the demodulator gain control voltage input (VGIN, pin 17)
Jumper LK6	Opened	Disconnecting the Q-channel baseband mixer/VGA output (QMXO, pin 22) from the other on-board detector input (VDT1, pin 20)
VDT1&2	Wired	Both detector input voltages (pin 20 & 18) are connected (seen as the blue wire in Figure 35) to the chip's internally created reference voltage output of 1.0 V (VREF, pin 14)

Table 11. Procedure to operate the AD8347 demodulator in the VGIN mode.

Simultaneously with this research on development of a radar demonstration T/R module, another project requiring an eight element direction finding (DF) receive antenna is in progress [47]. The AD8347 demodulator is also being implemented in that project,

so the combined device characterization consisted of ten demodulator boards. A setup shown in Figure 37 was utilized to measure the demodulator phase characteristics.

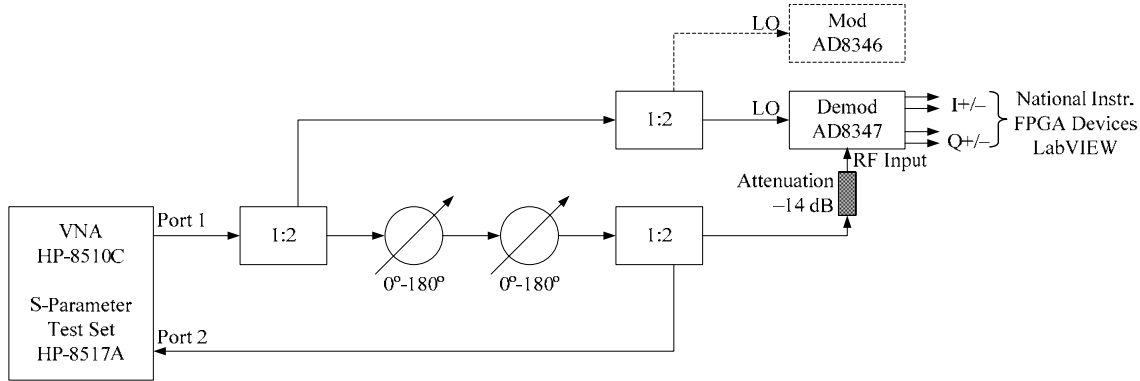


Figure 37. AD8347 Demodulator phase measurement setup.

The VNA port 1 is set for 2.4 GHz CW signal at the device default output level setting of +6 dBm. From Figure 13, the actual output from port 1 was measured at -5.8 dBm. The VNA output is split to create both LO and RF signals to feed the demodulator board. The LO signal, in turn, is split again to furnish both the transmit (modulator) and receive (demodulator) boards. The LO drive level for the AD8347 demodulator was set at -8.8 dBm.

The demodulator RF input is phase shifted using two cascaded Sage mechanically adjustable phase shifters (model 6708). Sage Laboratories was acquired in 1998 by the company Filtronic plc, which now markets the product. The phase shifter is rated for frequencies from dc – 8 GHz with a maximum insertion loss of 0.7 dB per stage [48]. The phase shifted RF signal is also split again. One output supplies the demodulator RF input after 14 dB attenuation in order to establish a proper operating point for the device. The other output is fed back to VNA port 2 for phase reference. In this manner the relative phase difference between the LO and RF inputs are controlled, and the demodulator output readings can be interpreted. The phase can be shifted over 360° using the two cascaded Sage components.

Operating in VGIN mode, the demodulator gain (i.e., the amplitude of the resulting I/Q circle) is set manually by a dc voltage between 0.2–1.2 V to the VGIN input (pin 17). The voltage on this pin controls the gain on the RF and baseband VGAs, and the gain control is applied in parallel to all VGAs. A lower applied VGIN value corresponds to a higher demodulator gain. The phase measurements were preceded by gauging for the optimal VGIN control voltage. The results indicated that a VGIN set to 0.38 V provided the largest I/Q circles without distorting the differential outputs.

The equipment settings and readouts for the operating point are summarized in Table 12.

Parameter	Setting/Value	Comments
Operating mode	VGIN	See Table 11
Operating frequency	2.4 GHz CW	Demodulator LO and RF inputs
VGIN	0.38 V	Specified between 0.2–1.2 V, with the lower limited providing the highest gain [45]
VNA output	–5.8 dBm	VNA port 1 set for an output of “+6 dBm” at 2.4 GHz CW, see Figure 13
RF pre–attenuation	14 dB	Create a sufficient level separation between the LO and RF signals
RFIN	–26 dBm	RF input levels are shown in graph down to –70 dBm, maximum rating is +10 dBm [45]
LO drive level	–8.8 dBm	Recommended at about –8 dBm [45]

Table 12. Demodulator phase measurement settings.

The demodulator quadrature outputs are subsequently fed to the NI–9215 analog input module, and the differential analog voltages are displayed by LabVIEW. The recorded values were listed in spread sheets, and then the I/Q circle plots were generated.

Figure 38 displays phase data for the ten AD8347 demodulator boards. Figure 38(a) shows the actual I/Q response of the ten demodulators, and it is evident that each board has an individual dc offset.



Figure 38(b) shows the same I/Q data centered at origin by simply subtracting the circle center values. This circle offset must be corrected in the  $I$  and  $Q$  processing. Each individual demodulator board must be calibrated and its resulting I/Q data digitally centered using an adaptive MATLAB script in LabVIEW.

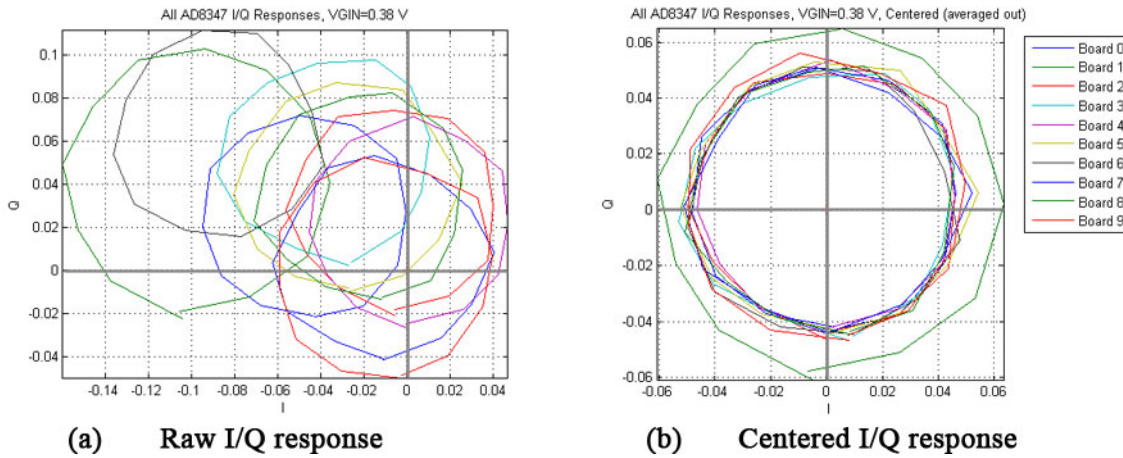


Figure 38. Plotted AD8347 demodulator phase characteristics.

Table 13 tabulates the phase characterization (i.e., the circle offset data) for the ten AD8347 demodulator boards. Boards number three and eight were chosen by reason of comparable I/Q circle radii for the two-element demonstrator array presented in this report. The corresponding I/Q circles for the chosen boards are depicted in Figure 39.

Board No.	Diameter $\Delta I/\Delta Q$ [mV]	Off-center $I_0/Q_0$ [mV]	
0	$\Delta I$ 94.4 / $\Delta Q$ 93.5	$I_0$ -46.5 / $Q_0$ +21.2	
1	$\Delta I$ 124.0 / $\Delta Q$ 125.6	$I_0$ -99.3 / $Q_0$ +38.5	
2	$\Delta I$ 96.2 / $\Delta Q$ 95.4	$I_0$ -6.1 / $Q_0$ +25.9	
<b>3</b>	<b><math>\Delta I</math> 98.4 / <math>\Delta Q</math> 95.3</b>	<b><math>I_0</math> -35.0 / <math>Q_0</math> +49.2</b>	*
4	$\Delta I$ 92.1 / $\Delta Q$ 98.0	$I_0$ +1.1 / $Q_0$ +17.7	
5	$\Delta I$ 106.4 / $\Delta Q$ 97.5	$I_0$ -28.5 / $Q_0$ +34.4	
6	$\Delta I$ 97.6 / $\Delta Q$ 95.6	$I_0$ -86.4 / $Q_0$ +60.4	
7	$\Delta I$ 103.2 / $\Delta Q$ 94.9	$I_0$ -11.4 / $Q_0$ +2.7	
<b>8</b>	<b><math>\Delta I</math> 96.4 / <math>\Delta Q</math> 95.6</b>	<b><math>I_0</math> -20.0 / <math>Q_0</math> +31.2</b>	*
9	$\Delta I$ 98.8 / $\Delta Q$ 102.6	$I_0$ -10.2 / $Q_0$ -3.3	

Table 13. Tabulated AD8347 phase characteristics (boards marked \* are incorporated in the two-element demonstrator array).

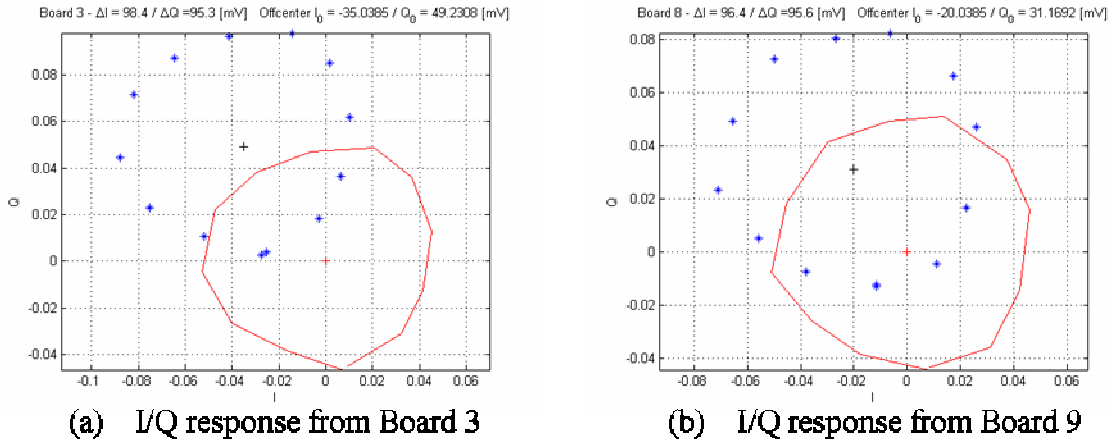


Figure 39. Characteristics of the two selected AD8347 demodulator boards.

The RF input signal to the AD8347 demodulator passes through two stages of variable gain amplifiers prior to two double-balanced Gilbert-cell mixers. One feature of a Gilbert-cell mixer is an improved suppression of spurious mixer products, since all even order products of the LO and RF signals are suppressed [49].

One concern in any receiving sub-system is to provide a sufficient image rejection filtering in the demodulator. The balanced nature of this mixer application guarantees proper performance in terms of RF/LO to baseband rejection, and no further filtering is required.

## 9. Voltage Controlled Oscillator

In the initial two-element demonstration array, a hard-wired voltage controlled oscillator (VCO) will serve as the distributed LO signal. Z-Communications, Inc. V800ME10 is the incorporated component, which is available from a previous project in the Microwave Lab.

The VCO chip is shown mounted on an evaluation board in Figure 40. The oscillator is adjustable between 2,400–2,485 MHz [50]. The output frequency is linearly dependent on the dc tuning voltage (specified for a range of 0.5–4.5 V<sub>dc</sub>) and on the ambient temperature (specified for –35 to +85 °C). The device will not be internal to the T/R module but rather will provide the demonstration setup hard-wired LO signals. The cable lengths can be controlled and kept equal for coherent operation.

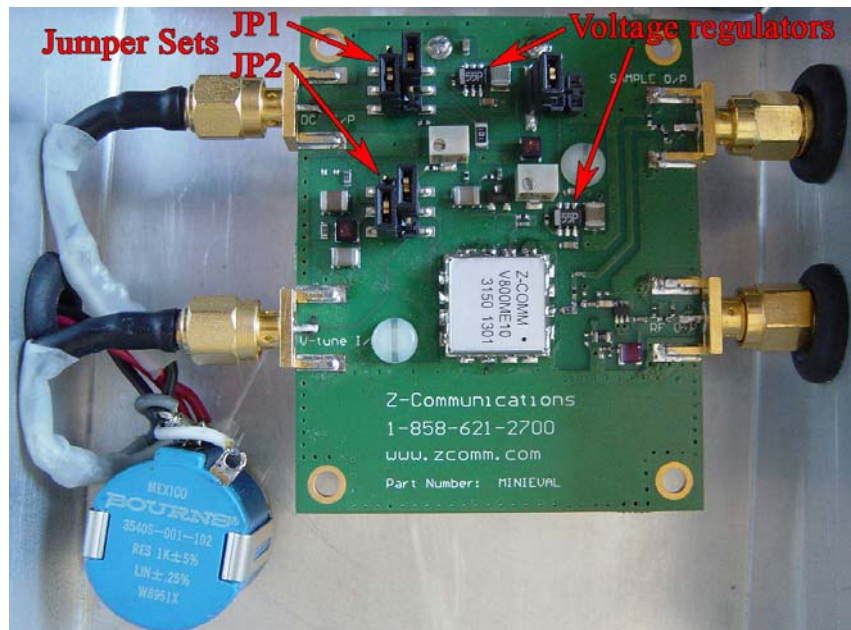


Figure 40. Z-Comm VCO V800ME10 mounted in a MINIEVAL evaluation board.

The jumpers on the MINIEVAL board for this application are set as described in Table 14 [51].

Jumper set	Connecting pins	Configuration
JP1	2&3	Supply Voltage: External biased operation
	5&6	Voltage Regulator: On board voltage regulator enabled
JP2	2&3 and 5&6	Tuning Voltage and Loop Filter: On board tuning voltage filter disabled

Table 14. VCO evaluation board configuration.

The operation of the VCO was verified using the frequency counter and the power meter listed in Table 1. The supply voltage is specified at 5 V dc nominally, where the oscillator output power should be  $5 \pm 2$  dBm [50]. However, when 5 V dc was applied to the VCO mounted in the evaluation board, the output power was measured at  $-1$  dBm. A reference to Z-Comm's product information established that the incorporated voltage regulators, shown in Figure 40, limit the supply voltage to +5.5 V dc for all input voltages up to 16 V. By feeding the setup +6 V, the device was operating in a more optimal state and was able to deliver +3 dBm (i.e., an increase of 4 dB compared to the lower supply voltage).

When the VCO provides two T/R modules with an LO signal, the oscillator output signal must be split 1:2, providing a signal level to each T/R module of 0 dBm. In the module itself, the LO signal is split again to feed both the modulator (transmit side) and the demodulator (receive side). Hence, each of the Analog Devices boards would experience a LO drive level of about  $-3$  dBm. The T/R module setup utilizing the V800ME10 VCO as an LO source has to be preceded by an analysis to establish a proper operating condition for the modulator and demodulator boards.

The AD8346 modulator requires an LO drive level between  $-6$  dBm and  $-12$  dBm [37]. For optimal performance, a drive level of  $-10$  dBm is recommended by the

manufacturer, although a level of  $-6$  dBm will result in more stable temperature performance. Therefore, the modulator LO input needs 3–7 dB of attenuation in this case.

The AD8347 demodulator is recommended for operation with a LO drive level of  $-8$  dBm [45]. This component requires about 5 dB of attenuation of the LO signal for proper operation conditions, given that an LO drive level of 0 dBm is fed to the T/R module.

#### **D. SUMMARY**

This chapter discussed some design considerations for a demonstration T/R module. Eventually, the LO distribution will be distributed wirelessly to all the modules, but for development purposes a hard-wired LO distribution is deemed adequate. Figure 12 displays the expected T/R module block diagram using commercially available RF components and hard-wired LO signals.

One of the key measuring instruments, the Hewlett–Packard VNA together with S-parameter Test Set, was characterized in terms of output power in Section C. Subsequently, all the commercial components being used in the initial demonstration T/R module were validated.

Chapter IV will cover the development of a demonstration array utilizing the T/R modules described above. Initially, the focus will be on a two-element array to validate the coherent operation of multiple modules. Eventually, an eight-element linear demonstration array will be developed.

THIS PAGE INTENTIONALLY LEFT BLANK

## **IV. DESIGN AND DEVELOPMENT OF A DEMONSTRATION ARRAY OPERATING AT 2.4 GHZ**

The proposed full-scale radar system will use the concept of an opportunistic array of surface-integrated elements. The operating frequency will be around 300 MHz in order to render the necessary radar performance, such as detection range and clutter mitigation. In order to validate some selected radar properties of the full-scale radar architecture, demonstration arrays will be developed and tested. The demonstration arrays will operate at 2.4 GHz and will utilize COTS based T/R modules described in the previous chapter.

Conceptual array properties of a radar system edified by separate T/R modules will eventually be verified using an eight-element linear array. Prior to this, an array of two elements will initially be designed and tested for proper and reasonable T/R module operation. The primary objective is to integrate the transmit and receive channels so that they are synchronized and exchange data in a coordinated manner in real time. The demonstration arrays are discussed in this chapter.

The chapter moreover covers some demonstration array simulations and analysis in terms of antenna patterns and is concluded by reviewing results of preliminary measurements using the two-element array demonstration array.

### **A. PROPOSED SYSTEM LEVEL ARCHITECTURE**

The proposed WNODAR realization is described in Chapter II. The radar system will occupy all available surfaces of the platform with individual T/R modules forming an opportunistic aperstructure. A CAD model of a ship with 1,200 elements is displayed in Figure 6, and the anticipated T/R module architecture is shown in Figure 7.

In the WNODAR, a central beamformer and controller unit computes beamforming data (amplitude weights and phase) together with applicable radar waveform parameters. The beamforming information, accompanied by the LO and synchronization signals, is distributed wirelessly to each active array element.

At each T/R module, the received control data forms the digital baseband signal in the DDS, the signal is then converted to analog, directly up-converted to the operating frequency band by the LO signal, power amplified and finally transmitted. On receive the RF signal is low-noise amplified, down-converted to baseband and digitalized. The digitized in-phase ( $I$ ) and quadrature ( $Q$ ) data is returned to the central beamformer and controller for signal processing.

## B. DEMONSTRATION ARRAY DESIGN

The efforts with demonstration arrays operating at 2.4 GHz aim to confirm some of the principles of the T/R module approach. An electrical and mechanical design concept was developed based on the components described in Chapter III. A coarse comparison can be made between the sought-after full-scale radar system shown in Figure 41 and the initial demonstration array shown in Figure 42, where both the similarities and the differences between the two architectures are apparent.

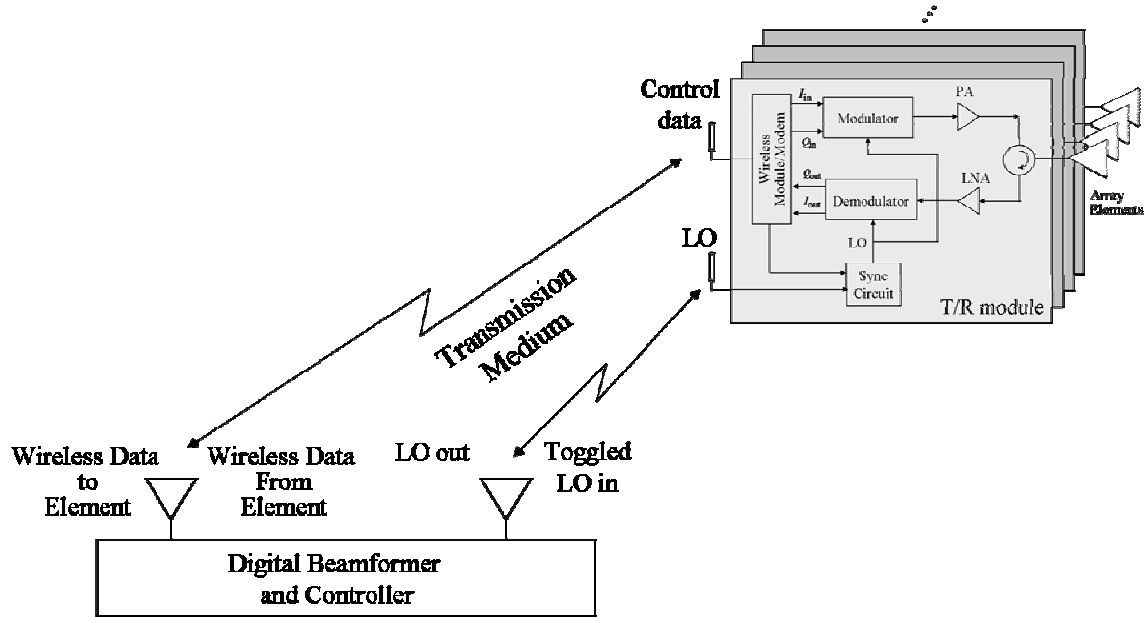


Figure 41. System level architecture for the full-scale WNODAR (After [20]).



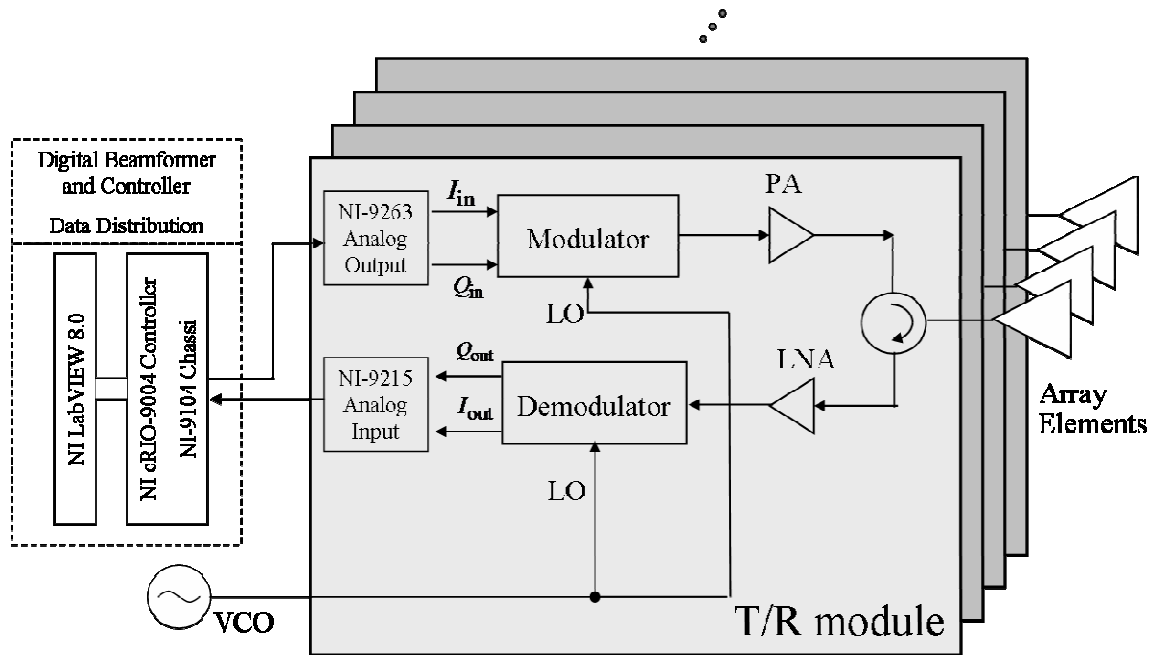


Figure 42. System level architecture for the demonstration array (After [20]).

The major differences between the demonstration array and the full-scale array (other than the frequency) are:

1. The number of elements is reduced, and they are periodically spaced in a linear array,
2. Low-power is used,
3. A wired LO distribution is used, and,
4. In the demonstration array, NI FPGA devices are used as the controller and waveform generator (there is no DDS).

### 1. Demonstration T/R Module Mechanical Design

The electrical design of the demonstration T/R module is presented in Figure 11 in Chapter III. The demonstration array will initially contain a linear array for simplified and straightforward evaluation of the results. The characterized components will be mounted in a demonstration T/R module enclosure. The enclosure must provide sufficient physical space to incorporate necessary internal wirings and connectors, satisfy

electromagnetic compatibility (EMC) issues (i.e., provide shielding), as well as optimize the inter–element spacing.

As a general guideline, the element spacing in a linear array should not exceed one half wavelength, with the aim of avoiding grating lobes when the antenna main–lobe beam is steered off broadside [52]. The demonstration frequency is at 2.4 GHz, which corresponds to a wavelength,  $\lambda$ , of 0.125 m in free space. The maximum element spacing, hence, would be 0.0625 m or 62.5 mm.

For a compact mechanical layout, some components must be stacked vertically, but due to the anticipated power dissipation and heat generation in the module, the components need internal space for air flow. A suitable enclosure was found at Digi–Key Corporation with side dimensions of 2 x 4 x 8 [in<sup>3</sup>]. This enclosure would accommodate the lowest possible element spacing at 2 in (50.8 mm). However, since the T/R module enclosure also serves as a heat sink for the internally dissipated power, the inter–element spacing must also allow for an air gap for adequate cooling. There is an existing eight–element ground plane for the dipoles from a previous project that has an element spacing of 65 mm (2.56 in). Using the existing ground plane for this project would yield an air gap of 0.56 in between the T/R modules, a distance deemed sufficient for cooling.

Figure 43 exhibits a first iteration of the components mounted in a 2 x 4 x 8 [in<sup>3</sup>] enclosure. For proper operation, some of the component connections were made outside of the enclosure, for instance, the demodulator board (see Figure 43, right hand side).

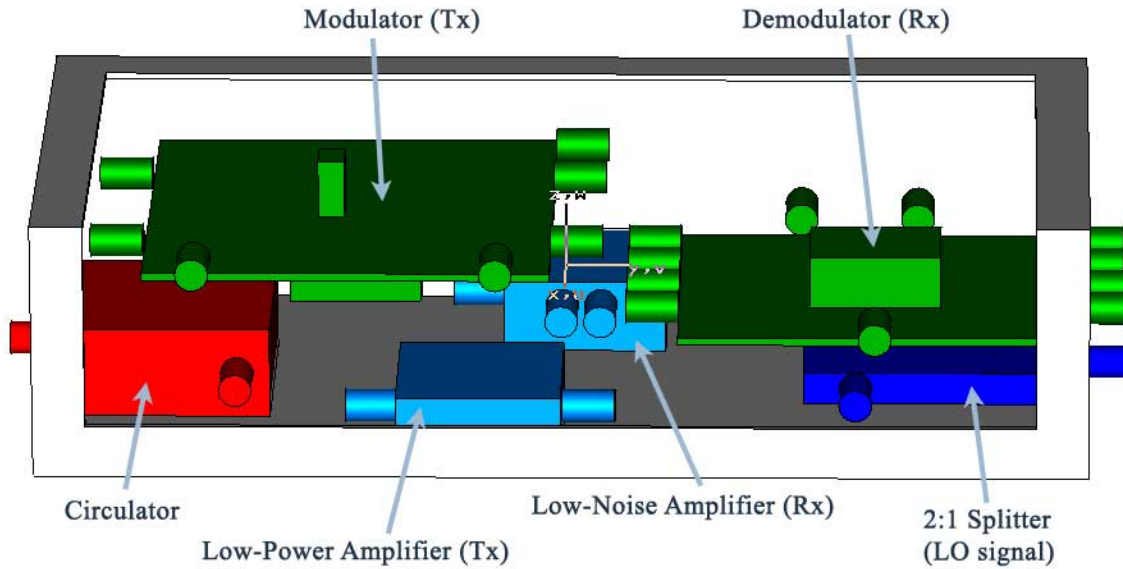


Figure 43. CAD model of a demonstration T/R module mechanical layout inside a 2 x 4 x 8 [in<sup>3</sup>] enclosure.

To verify the layout, a mock-up was built. After fitting the components with connectors and wiring, the conclusion was that a larger enclosure was needed. The same vendor provides a 2 x 5 x 9.5 [in<sup>3</sup>] box, which exceeds all dimensions except for depth, maintaining minimum element spacing.

The revised demonstration T/R module mechanical layout is presented in Figure 44. For clarity reasons, the module is shown without internal cabling. When wired, the enclosure will be sealed using a custom-made lid provided by the same vendor (Digi-Key Corporation).

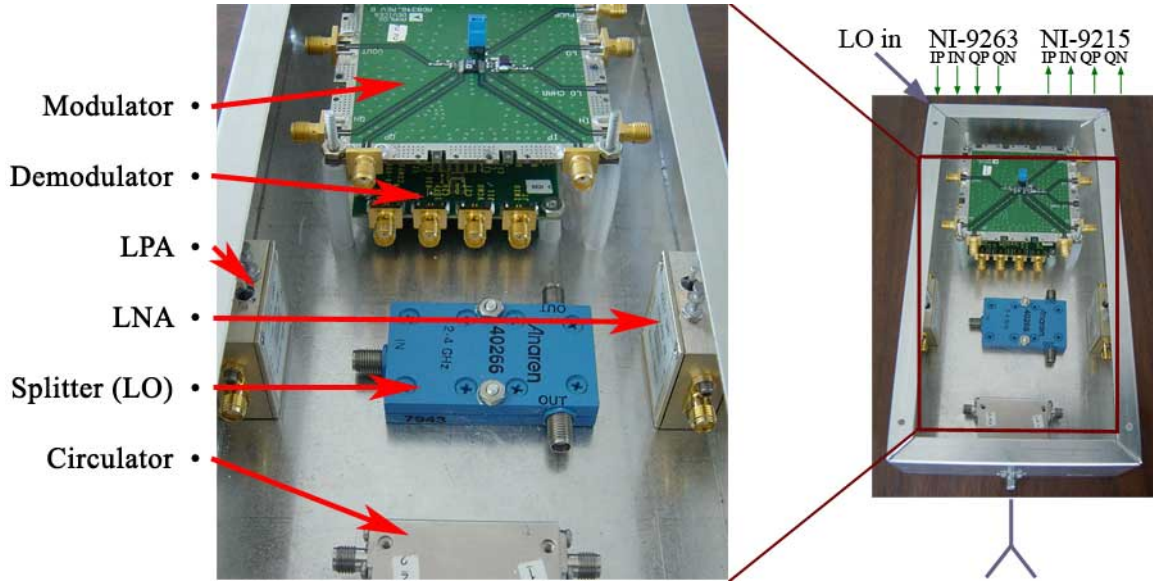


Figure 44. Final demonstration T/R module mechanical layout (unwired).

The material of the module enclosure is aluminum, which is a good electrical and thermal conductor. The electrical conduction guarantees a suitable EMC environment between the array elements. The chassis joints and apertures for the various cables are not electrically sealed; however, the frame minimizes any negative effects associated with EMI and coupling between adjacent T/R modules and cables.

Note in Figure 44 that the two largest power consumers in the module (the two amplifiers) are mounted directly to the sides of the enclosure, on opposite sides, to optimize internal heat dissipation.

## 2. Eight-element Array

As previously mentioned, an eight-element linear demonstrator will be used to verify some theoretical properties of the WNODAR. The number of elements is large enough to facilitate the proof of concept of a radar system consisting of separate T/R modules. Moreover, an eight-element array consists of a total of 16 NI modules (eight NI cRIO-9263 Analog Output and eight NI cRIO-9215 Analog Input modules) fully occupying two NI-9104 eight-slot chassis. The demonstration array will be linear, resulting in valid comparisons with the full-scale array performance.

The projected demonstration array is depicted in Figure 45. The eight elements are controlled by two NI cRIO-9004 real-time controller units each with a NI-9104 eight-slot reconfigurable embedded chassis. The controller conveys information from, and to, the NI PXI-1044, which executes the LabVIEW virtual instrument (vi). A PCI eXtensions for Instrumentation (PXI) is the open, multi-vendor standard for measurement and automation and claims to deliver more performance than older measurement and automation architectures [53].

Figure 45 shows the complete demonstration eight-element T/R module array incorporating NI cRIOs, AD modulators/demodulators, RF Bay LPAs/LNAs, DiTom circulators and printed circuit dipole antennas. The representation of one T/R module is circled in **red**. The LO distribution is shown as wired; however, the cables can be replaced with antennas at both the NI FPGA chassis and LO output. Thus, wireless distribution to two four-element subarrays can be demonstrated.

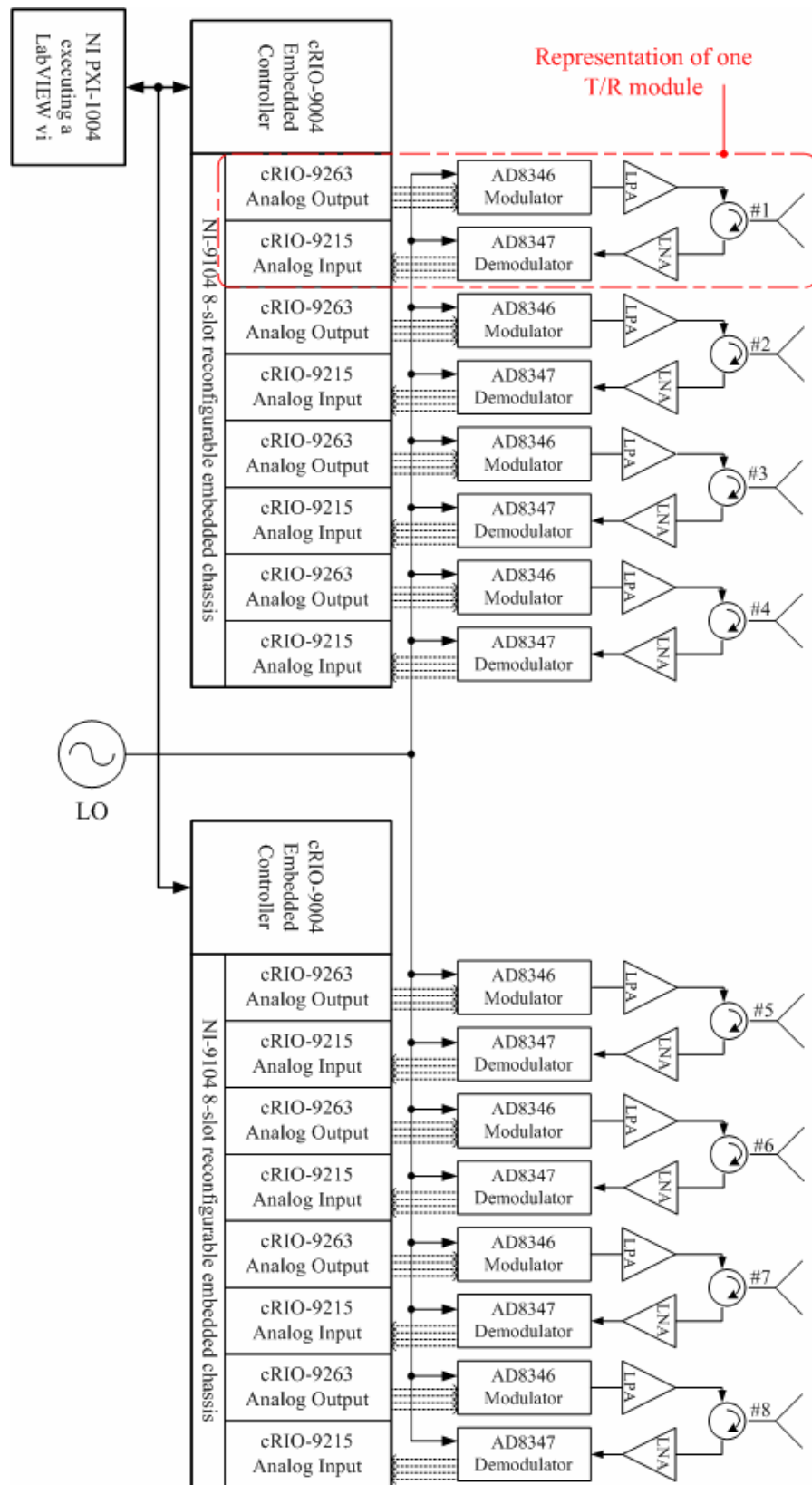


Figure 45. Block diagram of eight-element demonstration array.

### 3. Initial Two-element Setup

In preparation for building the eight-element array, the T/R module will be validated using a benchtop two-element array. A basic block schematic of the setup is shown in Figure 46.

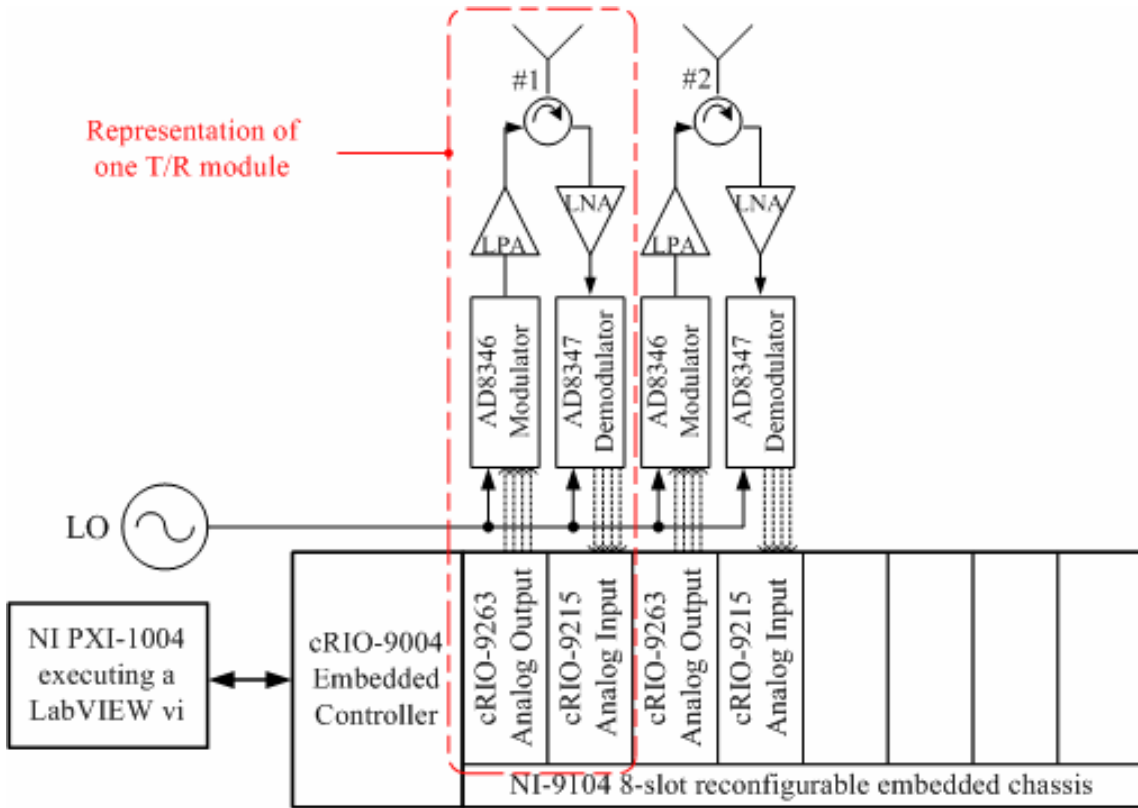


Figure 46. Block diagram of initial two-element demonstration array.

One goal with this setup is to develop a LabVIEW virtual instrument (VI) that will be able to control both the transmit (analog output module) as well as the receive (analog input) sides. The two-element array is convenient for bench testing in the lab. It will have all of the functionality of the full demonstration array. A major challenge is to concurrently provide output signals to modulators and receive input signals from demodulators, which are functions represented by two different kinds of modules. The

consequent synchronizations, as well as processor power allocation, are issues that will be resolved in future research.

### C. DEMONSTRATION ARRAY ANALYSIS

After bench testing the two-element array, the larger eight-element demonstration array will be constructed and tested in the anechoic chamber.

One reason for conducting initial measurements with a T/R module setup using a 1-D linear array is to receive realistic data, which can be compared with simple analysis. The power levels will be scaled down from the full-scaled system, but they must be sufficient to get reliable data in the chamber. A link analysis was performed to assure that the received and transmitted powers will be above the required thresholds.

#### 1. Power Budget for Measurements

The demonstration array will be measured in the NPS anechoic chamber, which is situated on the roof of Spanagel Hall, room Sp-604. Figure 47 displays a diagram of the chamber with dimensions [54].

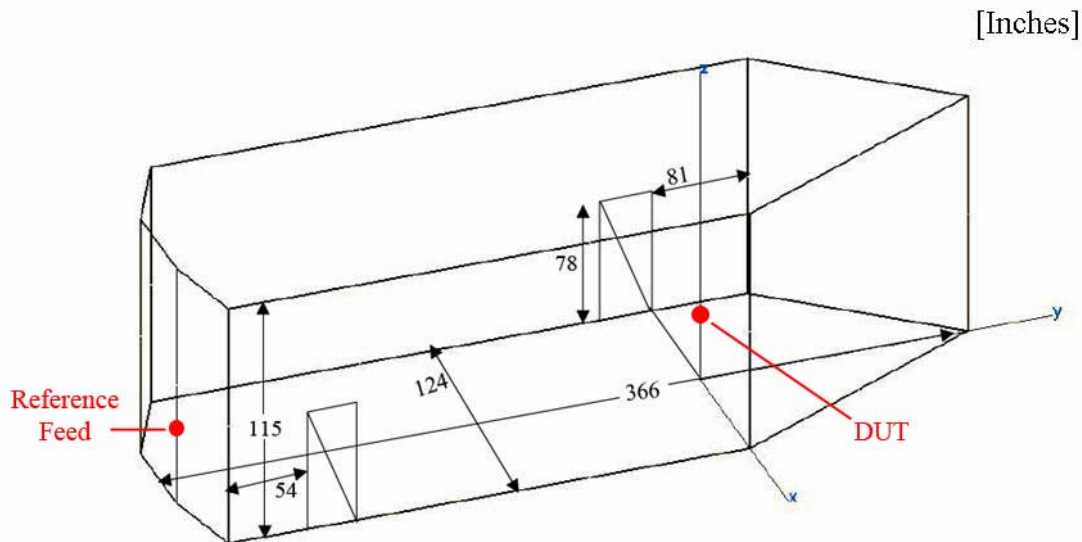


Figure 47. Sketch of the NPS anechoic chamber (From [54]).



The anechoic chamber measures about 19 ft, or 5.8 m, between the reference feed horn antenna and the DUT. The transmit and receive channels will be tested separately by receiving and transmitting, respectively, signals at the reference feed horn.

In order to estimate the received power by the demodulator, a link budget analysis was executed. The purpose of this effort was to establish whether the current demonstration array setup contained enough amplification on the receive side to be able to gather useful measured data using the NPS anechoic chamber.

The measurement setup in the anechoic chamber will be similar to Figure 48. The reference horn antenna will be fixed, while the demonstration array antenna will be rotated on a pedestal at a distance of 5.8 m.

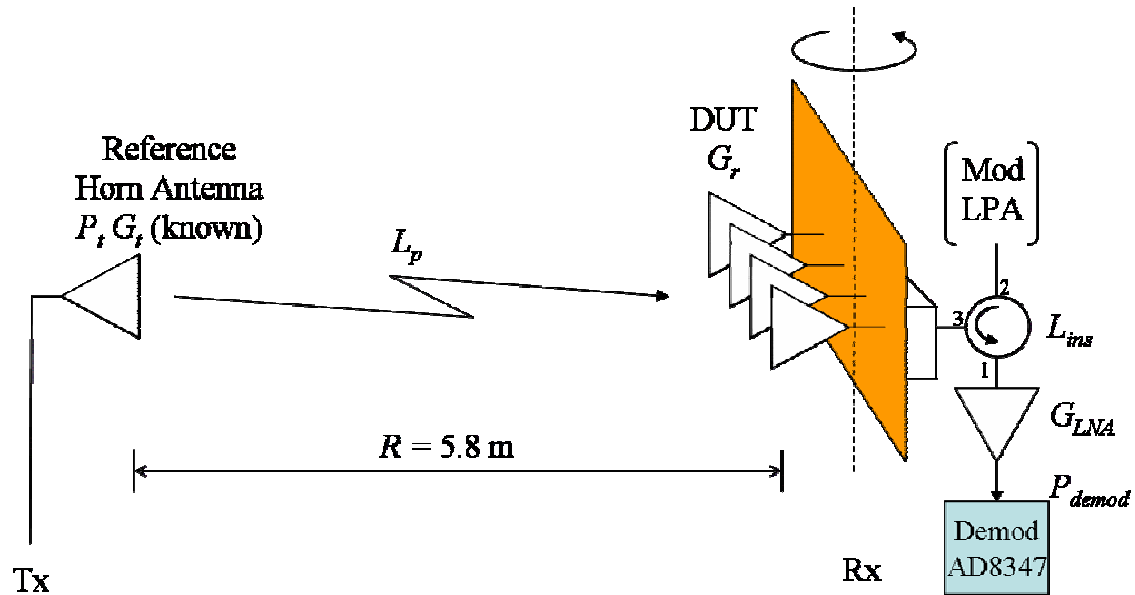


Figure 48. Fundamental Rx measurement setup in the anechoic chamber.

$P_{demod}$  is the delivered power [dBm] to the AD demodulator board. Of interest for this work is the RF signal level that can be expected for the device. The AD8347 specification does not clearly state a minimum RF input power, as mentioned earlier. A graph in [45] indicates a demodulator linear response to a RF input level down to  $-70$  dBm. However, for optimal operation of the demodulator board, the RF input level should not be smaller than  $-30$  dBm [45].

The received power at the demodulator RF input is given by (see Figure 48)

$$P_{demod} = P_t + G_t - L_p + G_r - L_{ins} + G_{LNA} \quad [\text{dBm}], \quad (13)$$

where

- $P_{demod}$  is the RF power [dBm] delivered to the AD8347 demodulator board,
- $P_t$  [dBm] +  $G_t$  [dB] is the reference horn antenna effective isotropic radiated power (*EIRP*) expressed in [dBm],
- $L_p$  is the free space propagation loss [dB] defined in Equation (14) below,
- $G_r = G_{dipole}$  is the element gain [dB],
- $L_{ins}$  is the insertion loss [dB] in the circulator between ports 3 and 1, and
- $G_{LNA}$  is the low-noise amplifier power gain [dB].

The power into the reference horn antenna,  $P_t$ , was measured in the chamber at 23 dBm using a HP power meter. The gain of the reference horn antenna,  $G_t$ , was established at 17.12 dB in Figure 30. The transmit *EIRP*, hence, is  $23 + 17.12 = 40.12$  dBm.

The free space propagation loss, which depends on the distance between the antennas, is

$$L_p = 10 \log_{10} \left[ \left( \frac{4\pi R}{\lambda} \right)^2 \right] = 20 \log_{10} \left( \frac{4\pi R f}{c} \right), \quad (14)$$

where  $\lambda$  is the wavelength [m],  $c$  is the speed of light [m/s], and  $f$  is the RF frequency [Hz]. Since the transmit–receive distance,  $R$ , is 5.8 m, the propagation loss is 55.3 dB.

The element gain,  $G_r = G_{dipole}$ , was calculated in Chapter III as 6.55 dB.

The circulator insertion loss between ports 3 and 1 on the device,  $L_{ins}$ , was measured earlier and is presented in Table 6. For the two–element demonstration array, the circulators at hand imply an insertion loss of 0.40 dB and 0.46 dB, respectively.

The  $G_{LNA}$  was characterized in terms of S-parameters in Chapter III. The forward transmission coefficient,  $S_{21}$ , was given at 24.8 [dB] and 24.0 [dB], in that order for the two specimens at hand.

The resulting expected power level (using worst case among the available devices) at the individual demodulator input is thus given by

$$P_{demod} = 23 + 17.12 - 55.3 + 6.55 - 0.46 + 24.0 = +14.9 \text{ [dBm]}, \quad (15)$$

which is more than sufficient to drive the demodulators. There will be no need for further LNA stages.

In a system consisting of non–ideal components, there are many possible sources of error to consider. In this case, an essential one is the transmit leakage due to insufficient circulator isolation between ports 2 and 1 and signal reflections due to antenna element mismatch. The upper power level limit into the demodulator is given by the LNA. The device is specified for a P1 compression value of +10 dBm, which equals the AD8347 demodulator maximum rating value, see Tables 7 and 12, respectively.

In this case, the calculated power level at the demodulator input lies above the specified P1 output level of the LNA. Depending on how large any miscellaneous losses in the real system are, the test range might have to attenuate the power into the reference horn antenna,  $P_t$ .

A corresponding analysis was made to also verify sufficient amplification on the transmit side. While conducting the measurements in the anechoic chamber, a set-up equivalent to the diagram shown in Figure 49 will be used.

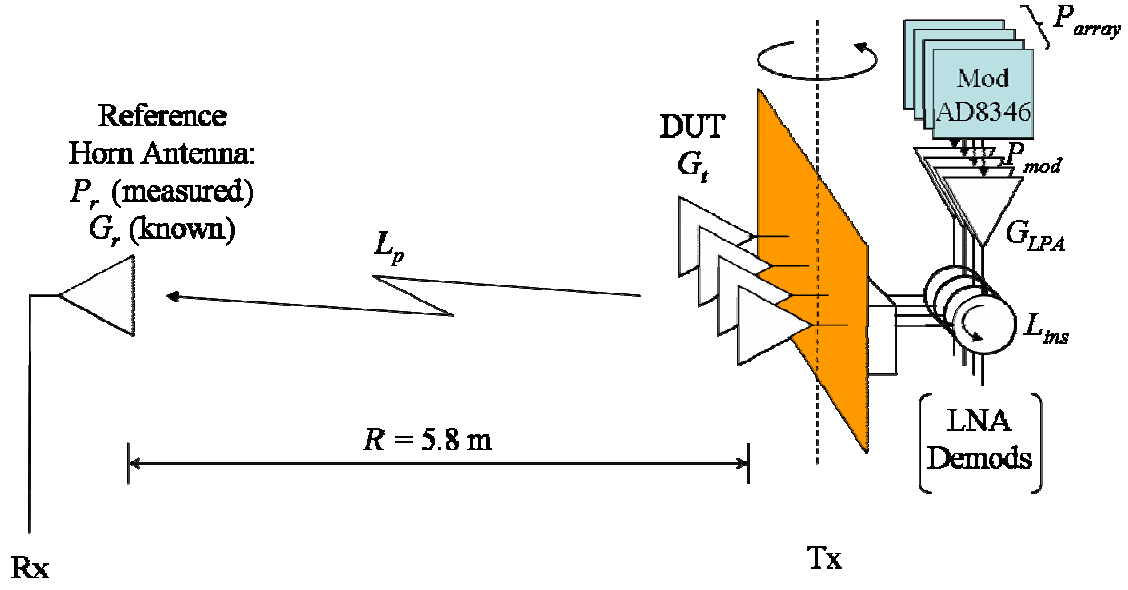


Figure 49. Block diagram of the array transmission measurement in the anechoic chamber.

The received power at the reference horn is given by

$$P_r = P_{array} + G_{LPA} - L_{ins} + G_t - L_p + G_r \quad [\text{dBm}], \quad (16)$$

where

- $P_r$  is the RF power [dBm] out of the reference antenna,
- $P_{array}$  [dBm] is the combined modulator output power in the array,
- $G_{LPA}$  is the low-power amplifier power gain [dB]
- $L_{ins}$  is the insertion loss [dB] in the circulator between ports 2 and 3,
- $G_t = G_{array} = G_{dipole} + AF_8$  is the combined array antenna gain [dB], which is a function of the individual element gain and the eight-element combined array factor,  $AF_8$ ,
- $L_p$  is the free space propagation loss [dB] previously calculated, and

- $G_r$  is the reference horn antenna gain [dB].

The combined modulator output power in the array represents all power generated in the array, i.e.,  $P_{array} [\text{mW}] = N [\text{elements}] \times P_{mod} [\text{mW/element}]$ . The modulator AD8346 was previously characterized in terms of generated output power in Chapter III, Section C3. Assume an operating point for the modulator boards, where I/Q differential amplitude is set to 2.0 V, and the LO level is at 6 dBm. Using these settings, the modulator output power,  $P_{mod}$ , is approximately  $-7$  dBm (see Figure 21). In an eight-element demonstration array, the combined modulator output power is increased by 6 dB (since a factor of 8 corresponds to 9 [dB]), i.e.,

$$P_{array} [\text{dBm}] = P_{mod} [\text{dBm/element}] + 9 [\text{dB}] = -7 + 9 = +2 [\text{dBm}]. \quad (17)$$

All T/R-modules in the demonstration array are furnished with identical low-power amplifiers and circulators, respectively, hence  $G_{LPA} = 17.3$  dB (see Table 4), and between circulator port 2 and 3,  $L_{ins} = 0.46$  dB (see Table 6).

The gain of the linear array is  $N \cdot G_{dipole}$  which corresponds to about 15.6 dB, based on the measured data. However, a simulation of the eight-element demonstration array incorporating models of the printed circuit board dipole antenna has been conducted with the software tool CST Microwave Studio. The broadside pattern is shown in Figure 50. Neglecting antenna losses,  $G_{array}$  equals the array directivity, and from Figure 50,  $G_{array}$  is 16.5 dB. The  $EIRP$  from the demonstration array is expected to be

$$\begin{aligned} EIRP &= P_{array} + G_{LPA} - L_{ins} + G_{array} \\ &= 2 + 17.3 - 0.46 + 16.5 = 35.3 [\text{dBm}] \leftrightarrow 3.39 [\text{W}], \end{aligned} \quad (18)$$

and the corresponding power density,  $P_D$ , at a distance of  $R = 5.8$  m is

$$P_D = \frac{EIRP}{4\pi \cdot R^2} = \frac{3.39}{4\pi \cdot 5.8^2} \left[ \frac{\text{W}}{\text{m}^2} \right] = 8.02 \left[ \frac{\text{mW}}{\text{m}^2} \right]. \quad (19)$$

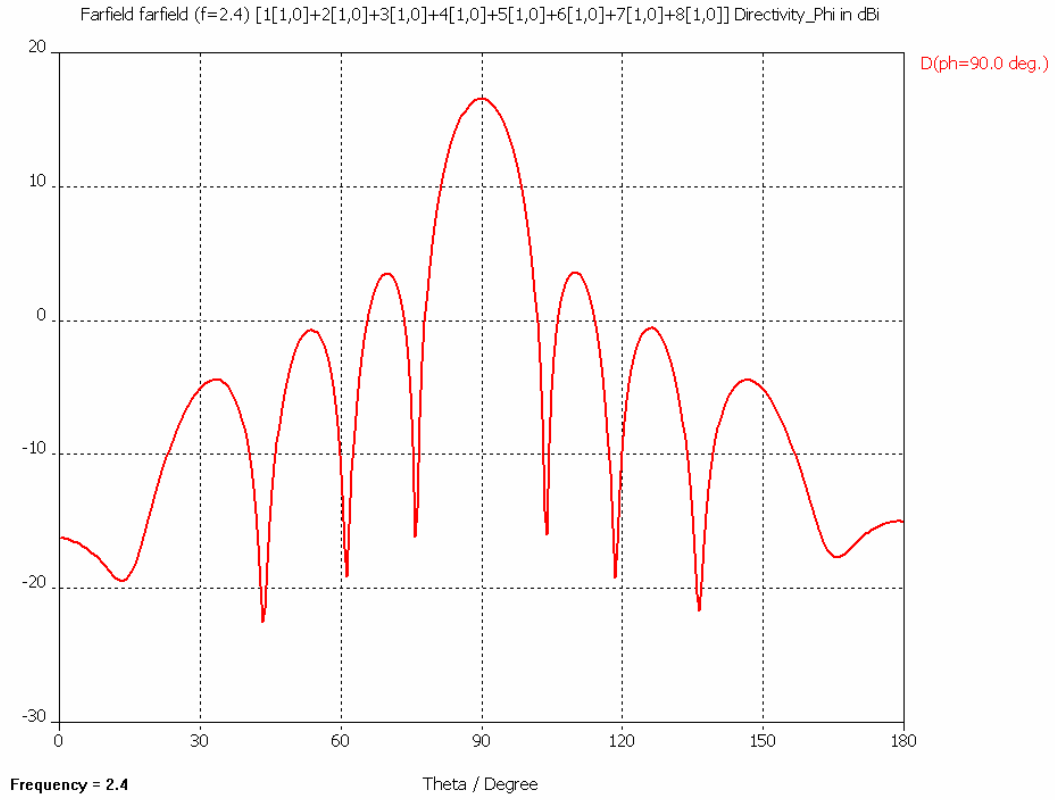


Figure 50. Simulated directivity of the eight–element demonstration array.

Considering the free space propagation loss  $L_p = 55.3$  dB and the gain of the reference horn antenna,  $G_t = 17.12$  dB (see Figure 30), the expected received power at the output of the reference antenna from an eight–element demonstration array transmitting mainlobe–to–mainlobe is

$$P_r = 2 + 17.3 - 0.46 + 16.5 - 55.3 + 17.12 = -2.84 \text{ [dBm]}. \quad (20)$$

Both the calculated power density at the reference horn antenna (at  $8.02 \text{ mW/m}^2$ ), and the expected received power ( $-2.84 \text{ dBm}$ ) are well within the working specification of the power measurement circuitry in the anechoic chamber. No need of further amplification is foreseen for the initial measurements of the T/R module transmission measurements.

## 2. Ground Plane Dimensions

One issue in the demonstration array analysis was to determine ground plane design criteria in terms of minimum dimensions. The element spacing was discussed in the previous chapter and selected at 2.56 in or 65 mm. The chosen T/R module enclosure depth is 2 in, which leaves 0.56 in or about 14 mm to allow sufficient air flow between the modules. Figure 51 presents a sketch of the eight-element array situated over a copper foil ground plane.

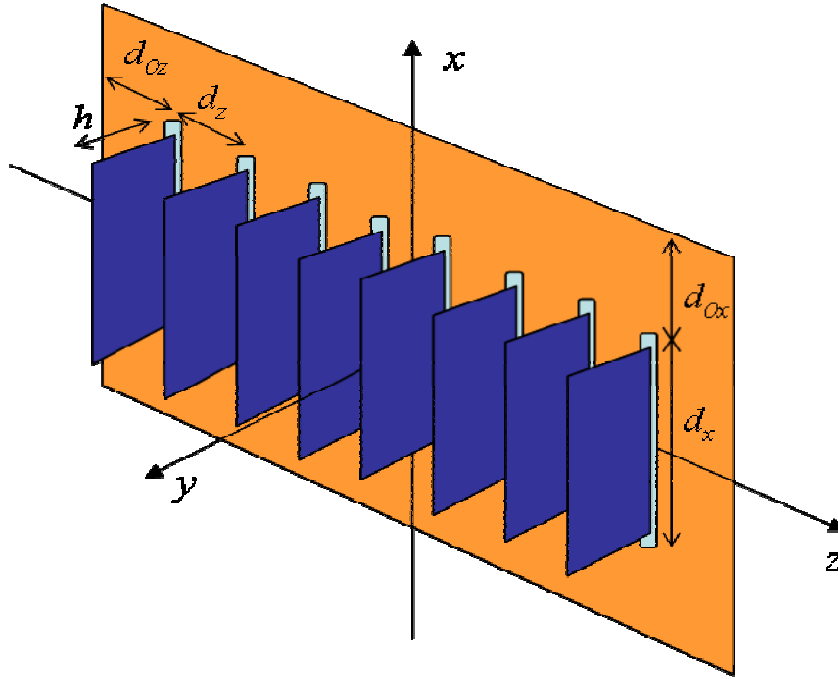


Figure 51. Eight-element array over a ground plane.

After discussions [39], it was concluded that distances according to Table 15 would suffice in order to avoid edge effects and to accommodate beam steering of up to 45°. Along the  $z$ -axis, the element-to-edge distance should not be less than  $\lambda/2 = 62.5$  mm. The corresponding value along the  $x$ -axis is  $\lambda/4 = 31.25$  mm.

Dimension	Element size (x,y)/spacing (z)	Edge distance	Ground plane dimension
$x$	$d_x = 89$ mm	$d_{0x} = \frac{\lambda}{4} = 31.2$ mm	$d_x + 2 \times d_{0x} = 151.5$ mm
$y$	$h = \frac{\lambda}{4} = 31.2$ mm	N/A	N/A
$z$	$d_z = 2.56'' = 65$ mm	$d_{0z} = \lambda/2 = 62.5$ mm	$7 \times d_z + 2 \times d_{0z} = 580$ mm

Table 15. Minimum ground plane dimensions.

The minimum ground plane for the eight-element demonstration array is estimated at  $580 \times 152$  [mm<sup>2</sup>]. The existing ground plane meets this requirement.

#### D. DEMONSTRATION ARRAY SIMULATIONS

Simulations were conducted regarding an expected antenna pattern for an eight-element array. One purpose of the analysis was to determine whether the intended element spacing would be able to avoid grating lobes when scanning the array. Another goal was to create simulated pattern information in order to have something to eventually compare with the measured data from the anechoic chamber.

The element spacing was established at 2.56 in (i.e., 65 mm, or  $0.52\lambda$  at 2.4 GHz) for mechanical reasons. The selected element spacing is slightly larger than  $\lambda/2$ , which is acceptable because the beam is not being scanned to endfire. This simulation is aimed at verifying that no grating lobes will occur with the chosen spacing, when the array beam is scanned out to an angle of 45° [39].

Any antenna array gain consists of an element factor combined with an array factor [52]. In this case, dipole elements are situated  $h = \lambda/4$  above a ground plane with



an inter–element spacing of  $0.52\lambda$ . Dipole elements over a ground plane can be regarded as subarrays along the  $y$ -axis, which in turn constitute the elements in the larger array along the  $z$ -axis. Figure 51 shows an eight–element array with the dipole height of  $\lambda/4$  over the ground plane along the  $y$ -axis and the element (i.e., the subarray) spacing of  $d_z = 0.52\lambda$  along the  $z$ -axis. Due to the symmetry of the system, the origin is situated in center of the array, at the ground plane.

A uniform array is a notation for an array of identical elements with a progressive phase. Initially, the analysis of the demonstration array will involve operating the array uniformly (i.e., with an identical magnitude for all elements). Later on, more complex amplitude settings will be used.

The expected antenna pattern was simulated twice. A first–cut, coarse simulation using the theoretical relations presented in [52] and assuming an infinite ground plane was executed in MATLAB. The second simulation utilized the software tool CST Microwave Studio.

## 1. MATLAB Simulations

For the MATLAB simulations, the relations given in [52] were transferred into the code. With the current modeled array arrangement, the element factor ( $EF$ ) consists of an approximated dipole pattern. The subarray (i.e., the individual dipoles mirrored in a ground plane, assumed to be a perfect electric conductor, PEC) implies an array factor for a two–element array ( $AF_2$ ) along the  $y$ -axis. Finally, the dipole elements aligned along the  $z$ -axis in a linear array constitute an eight–element array ( $AF_8$ ).

### a. Element Factor

When oriented according to Figure 51, the printed circuit dipole element lies on the protruding edge of the card parallel to the  $x$ -axis. The element pattern is

$$EF = \sqrt{1 - \sin^2 \theta \cdot \cos^2 \phi} . \quad (21)$$

**b. Dipole over PEC**

The dipole and its image form a two-element array along the  $y$ -axis (see Figure 51). The dipole is mirrored in the PEC, creating an image with opposite sign but with identical phase excitation at a distance of  $d_y = 2h = 2 \cdot \frac{\lambda}{4} = \frac{\lambda}{2}$  [m]. The direction cosine along the  $y$ -axis is

$$\begin{aligned}\cos \gamma &= \hat{y} \cdot \hat{r} \\ &= \hat{y} \cdot (\hat{x} \sin \theta \cos \phi + \hat{y} \sin \theta \sin \phi + \hat{z} \cos \theta) \\ &= \sin \theta \sin \phi.\end{aligned}\tag{22}$$

With this two-element array centered at the ground plane, the expression for the array factor results in

$$\begin{aligned}AF_2 &= (+1)e^{+j(kh \cdot \cos \gamma)} + (-1)e^{-j(kh \cdot \cos \gamma)} \\ &= 2j \cdot \sin \left( \frac{\pi}{2} \cdot \sin \theta \sin \phi \right),\end{aligned}\tag{23}$$

where  $k = \frac{2\pi}{\lambda}$ . When plotting the pattern, however, only the magnitude is of interest:

$$|AF_2| = \left| 2j \cdot \sin \left( \frac{\pi}{2} \cdot \sin \theta \sin \phi \right) \right|.\tag{24}$$

**c. Eight-element Array Factor**

For an  $N$ -element linear array, the  $N$  elements have uniform spacing and are excited with uniform amplitude (set  $a_n = 1$ ). An array along the  $z$ -axis experiences a direction cosine given by

$$\begin{aligned}
\cos \gamma &= \hat{z} \cdot \hat{r} \\
&= \hat{z} \cdot (\hat{x} \sin \theta \cos \phi + \hat{y} \sin \theta \sin \phi + \hat{z} \cos \theta) = \cos \theta
\end{aligned} \tag{25}$$

and the resulting  $N$ -element array factor is [52]

$$AF_N = \sum_{n=1}^N e^{j \frac{2n-(N+1)}{2} \cdot kd_z \cdot \cos \theta + \beta}, \tag{26}$$

where  $\beta = kd_z \cos \theta_s$ , and  $\theta_s$  is the scan angle.

The eight-element demonstration array is situated along the  $z$ -axis and centered at origin of the coordinate system in Figure 51. Using the relation in Equation (26), the array factor can be expressed as

$$\begin{aligned}
AF_8 = & e^{-j \frac{7}{2} (kd_z \cdot \cos \theta + \beta)} + e^{-j \frac{5}{2} (kd_z \cdot \cos \theta + \beta)} + e^{-j \frac{3}{2} (kd_z \cdot \cos \theta + \beta)} + e^{-j \frac{1}{2} (kd_z \cdot \cos \theta + \beta)} \\
& + e^{+j \frac{1}{2} \cdot kd_z \cdot \cos \theta + \beta} + e^{+j \frac{3}{2} \cdot kd_z \cdot \cos \theta + \beta} + e^{+j \frac{5}{2} \cdot kd_z \cdot \cos \theta + \beta} + e^{+j \frac{7}{2} \cdot kd_z \cdot \cos \theta + \beta},
\end{aligned} \tag{27}$$

which, using  $d_z = 0.52\lambda$  and basic trigonometric relations, simplifies to

$$AF_8 = 2 \cdot \sum_{m=1}^4 \cos \left[ \frac{2m-1}{2} (1.04\pi \cdot \cos \theta + \beta) \right]. \tag{28}$$

#### ***d. Total Array Pattern***

The total array pattern is achieved when multiplying the element factor with the array factors [52]. Using Equations (21), (24) and (28), we get

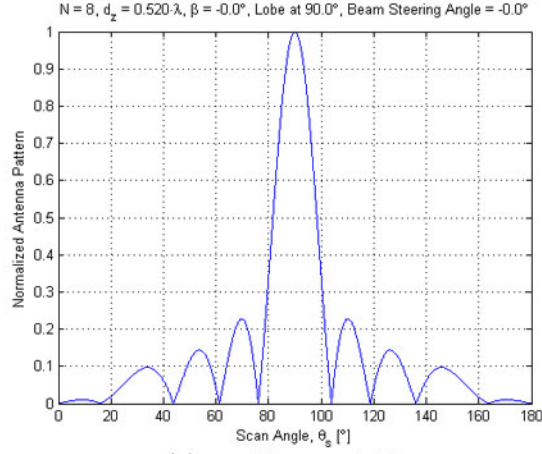
$$\begin{aligned}
|E_{total}| &= |EF \cdot AF_2 \cdot AF_8| \\
&= \left| \sqrt{1 - \sin^2 \theta \cdot \cos^2 \phi} \cdot \left[ 2 \sin \left( \frac{\pi}{2} \cdot \sin \theta \sin \phi \right) \right] \right. \\
&\quad \left. \cdot 2 \cdot \sum_{m=1}^4 \cos \left[ \frac{2m-1}{2} (1.04\pi \cdot \cos \theta + \beta) \right] \right|.
\end{aligned} \tag{29}$$

***e. MATLAB Coding and Plots***

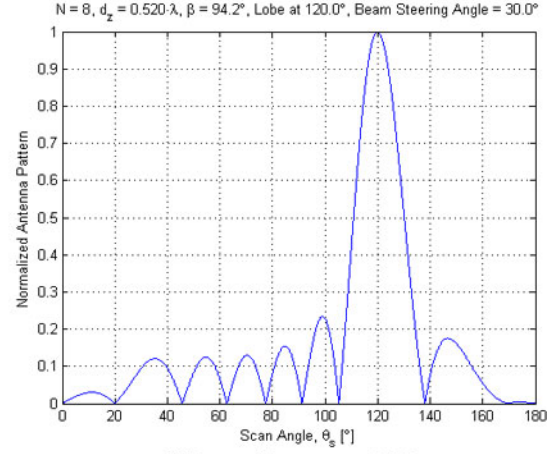
Equation (29) was programmed into a MATLAB script, and a simulation suite was executed. By changing the element incremental phase excitation,  $\beta$ , the array beam can be steered off the array broadside. Figure 52 presents a series of plots where the antenna array main beam is steered from  $0^\circ$  to  $50^\circ$  with an increment of  $10^\circ$ .

Evident from the plots in Figure 52, the antenna pattern beamwidth will widen and the relative sidelobe level will increase as the main beam is steered away from array broadside. This is because the array gain drops as the beam is steered off broadside. The simulations show no signs of grating lobe occurrence within this beam steering range (out to  $50^\circ$ ).

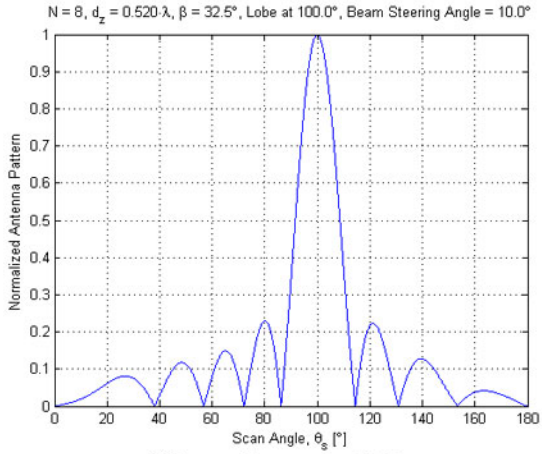
The plots in Figure 52 are generated using the MATLAB script *AntennaPattern.m* which can be found in Appendix A.



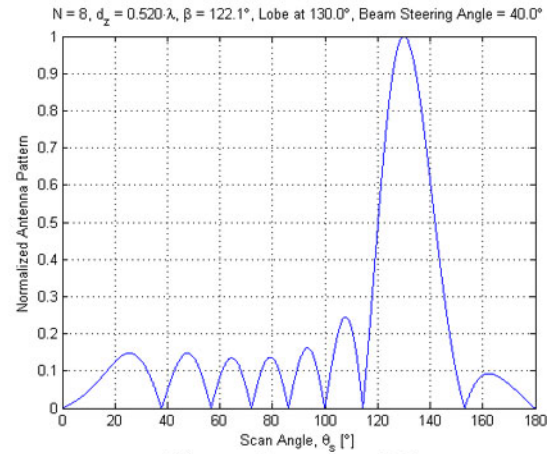
(a) Beam at  $0^\circ$



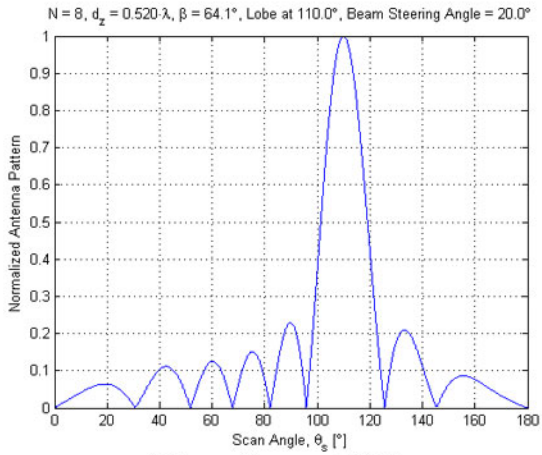
(d) Beam at  $30^\circ$



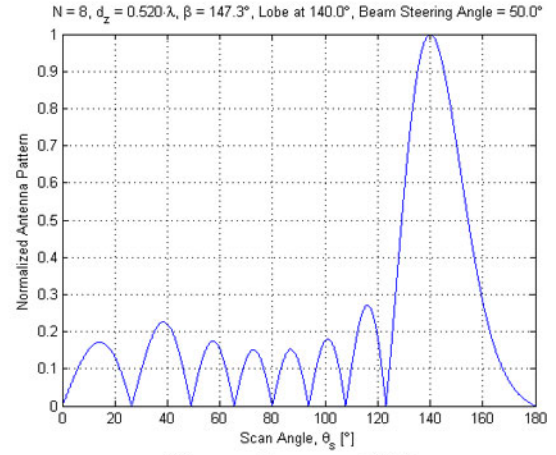
(b) Beam at  $10^\circ$



(e) Beam at  $40^\circ$



(c) Beam at  $20^\circ$



(f) Beam at  $50^\circ$

Figure 52. MATLAB plots of simulated antenna array beam steering.

## 2. CST Microwave Studio Simulations

CST Microwave Studio® (CST MWS) is an RF engineering tool for the fast and accurate 3D EM simulation of high frequency applications [55]. The simulation tool is based on the general finite integration technique (FIT), which can be used both in the time and frequency domains.

An existing model of an array using the printed circuit dipole elements over a ground plane was modified in terms of element spacing and ground plane characteristics, and a series of simulations was conducted.

Figure 53 shows the model for this project, where the eight dipole elements are placed in a ground plane. The coordinate system is the same as displayed in Figure 51 above, with the ground plane in the  $x$ - $z$  plane and the normal along the positive  $y$ -axis.

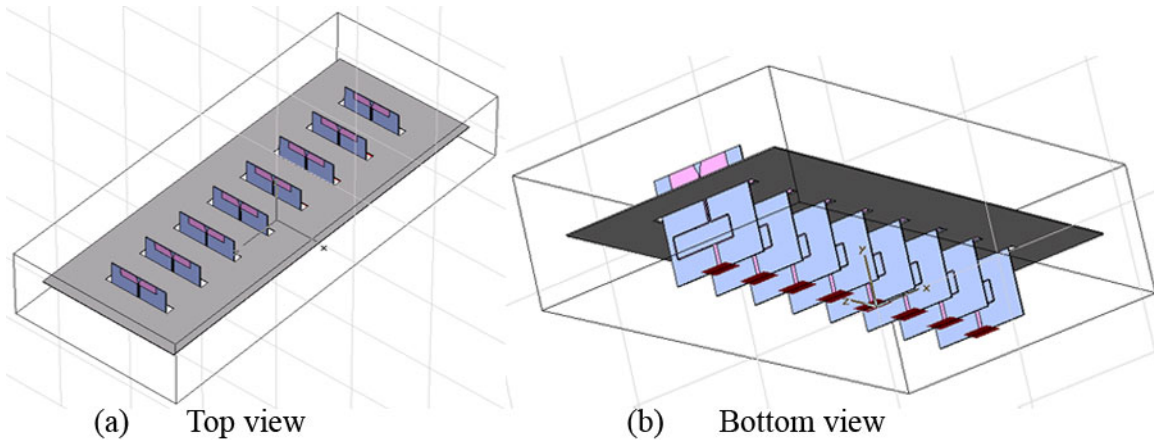


Figure 53. CST Microwave Studio model of eight dipole elements over a ground plane.

CST MWS simulates and calculates the contribution of each element and the inter-element mutual coupling, as well as the ground plane edge diffraction. Figure 54 presents the simulated results of the sum pattern with the array beam at broadside (i.e., with constant phase excitation among the elements) and with the array main beam scanned  $40^\circ$  off the array normal. The simulation verified that there were no grating lobes or scan blindness occurring.

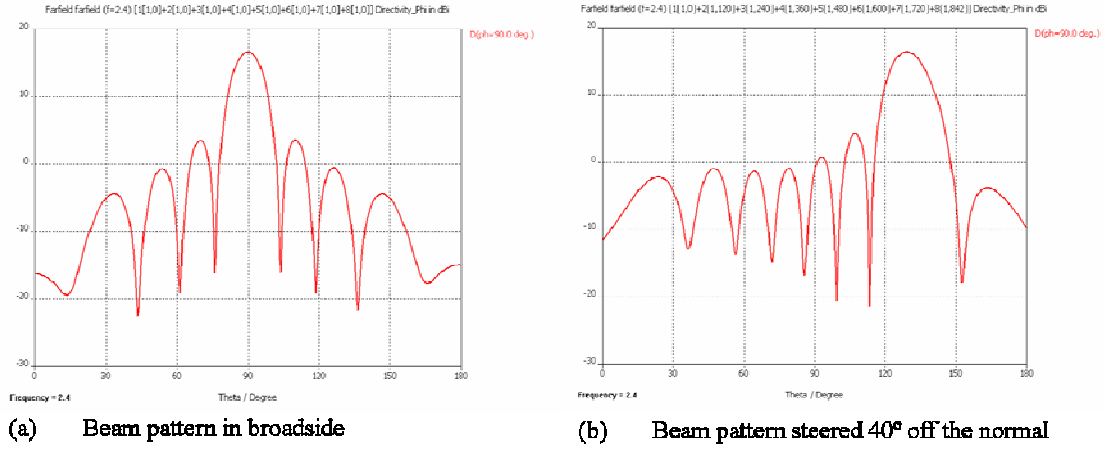


Figure 54. CST Microwave Studio simulated sum patterns (eight–element array).

### 3. Comparison MATLAB — CST MWS Simulations

In order to validate the coarse MATLAB script and simulations, a comparison between the results obtained from the two software tools was conducted. Contrary to the MATLAB results, CST MWS offers a quantitative outcome of the antenna array directivity. Previously in this chapter, it was found that, neglecting losses,  $G_{array} = 16.5$  dB.

To furnish a comparison of the simulated results, the MATLAB script was modified to provide the antenna pattern data expressed in dB and normalized to fit with the CST MWS maximum read–outs. Figures 55 and 56 show the sum patterns from the two simulation software applications for beam scanning angles of 0° and 40°, respectively. The patterns show good agreement for both scan angles.

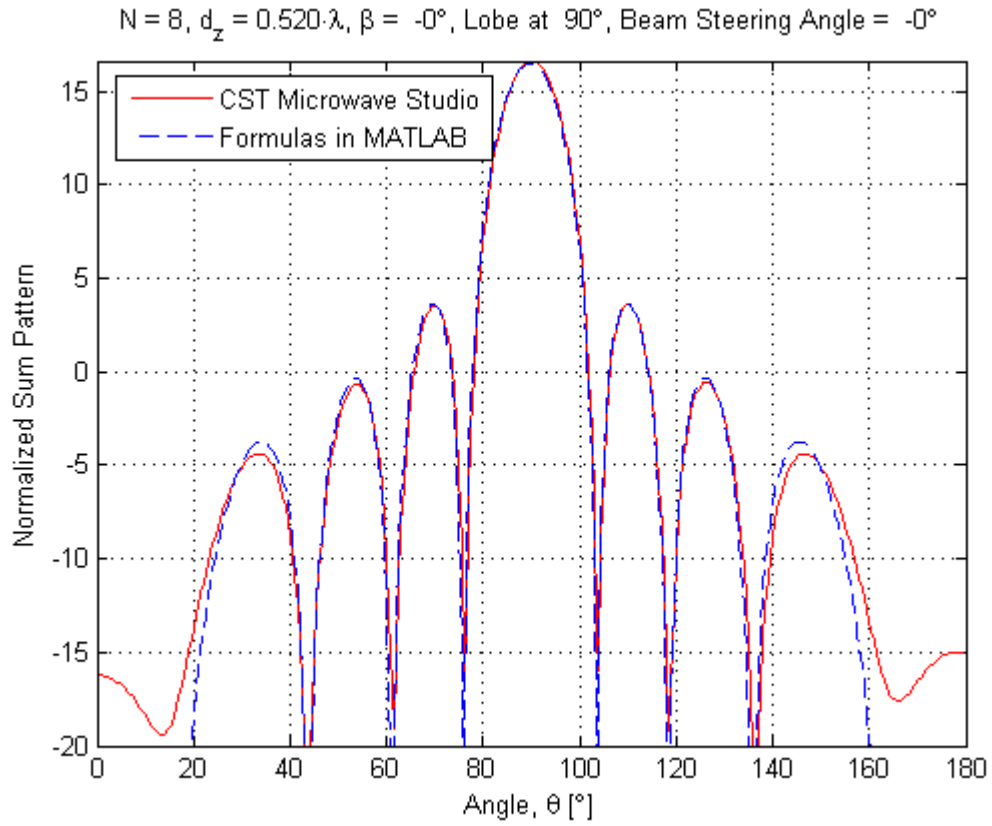


Figure 55. Comparison between simulated results from CST MWS and MATLAB ( $\theta_s = 0^\circ$ ).



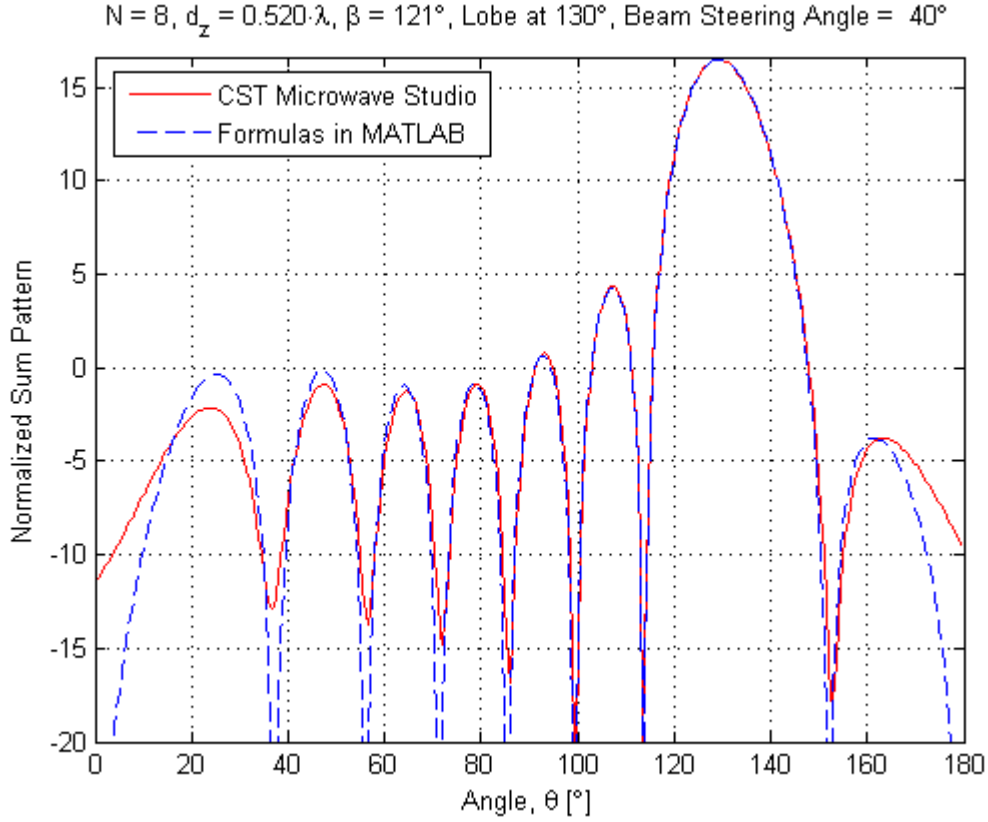


Figure 56. Comparison between simulated results from CST MWS and MATLAB ( $\theta_s = 40^\circ$ ).

## E. SUMMARY

This chapter is devoted to the design and development of demonstration arrays operating at 2.4 GHz. A mechanical layout of the demonstration T/R module was developed and realized using the previously characterized components. Demonstration arrays were designed incorporating NI FPGA devices and software functions to represent the beamformer and controller unit in the final WNODAR application. The transmitter and receiver sides have been operated separately using LabVIEW.

The demonstration array was analyzed in terms of power budget calculations for both receive and transmit modes. One reason for this particular analysis was to establish the need of additional amplification, if any. According to the analysis results, it appears

as if there is no need for supplementary amplification in the system; the power levels in transmit as well as in receive should suffice.

An analysis regarding the ground plane dimensions was conducted, and it showed that the existing eight-element ground plane, with an element spacing of  $d_z = 0.52\lambda$ , fulfills the theoretical requirements.

The chapter was concluded with two simulation runs one using a MATLAB code representing antenna array properties and another using a more complex model using CST Microwave Studio. The two simulation results showed good agreement.

Conclusions to the work as well as recommendations for future work are found in the next chapter.

## **V. CONCLUSIONS AND RECOMMENDATIONS**

### **A. CONCLUSIONS**

The opportunistic phased array and aperstructure concepts offer exciting possibilities for military radar applications. Placing separate T/R modules at available locations covering the whole superstructure and hull of a naval vessel provides a combined large-scaled antenna configuration. The large antenna dimensions imply that a frequency band (VHF/UHF) can be used and still achieve excellent radar characteristics such as angular resolution. Integrating the elements in the form of low-profile patch antennas in the structure of the ship, in addition, improves the stealth properties of the platform.

The WNODAR is an ongoing project at NPS, where the opportunistic and wireless concepts are examined. Each element has its own transmitter and receiver combined into a T/R module. The WNODAR application is essentially a sensor network where the beamformer and controller network uses wireless transmission.

One objective of this thesis was the design and development of demonstration T/R modules for verification of WNODAR concepts. The emphasis of this research has been the ISM-band component evaluation and characterization, and at the hardware development and design. A demonstration T/R module was electrically and mechanically designed using the characterized commercial components.

Previously, in this ongoing research project, quadrature modulator and demodulator devices had been studied separately. In this thesis the process was begun to integrate them into a common T/R module. The module is controlled using LabVIEW and an FPGA. Analog input and output modules were used to control the Analog Devices demodulator and modulator, respectively. The demodulator boards were calibrated so that offsets in the I/Q circles can be removed by receive signal processing.

The operation of a demonstration array consisting of eight linearly spaced modules was analyzed in terms of a power budget and the antenna ground plane dimensions. The analysis results were that no additional power amplification is foreseen on the transmit or receive branches for the expected measurement of the eight-element

demonstration array in the NPS anechoic chamber. Furthermore, for the expected operations of the array, the dimensions and properties of an existing array ground plane were deemed adequate.

Another objective of the thesis was to conduct a simulation of the demonstration array beamforming capabilities. The eight–element linear array was modeled in both MATLAB and CST Microwave Studio and showed good agreement between the two software tool results.

## **B. RECOMMENDATIONS FOR FUTURE WORK**

### **1. Two–element Array**

The work with the two–element bench testing set-up must be completed, measured and analyzed. One of the major purposes of the continuing research is to establish means for LabVIEW to fully control the demonstration T/R module transmit and receive sides simultaneously. Basic measurements can be conducted in the lab to prove the concepts of the system prior to an extension to the eight–element study in the anechoic chamber.

### **2. Eight–element Array**

After validating the initial two–element array, the next phase is to extend the demonstration array into an eight–element linear one. There are hardware and software improvements to be made to the demonstration modules and the LabVIEW virtual instrument prior to the construction of the array. By applying phase offsets to the array elements, the effects of amplitude weighting can be examined. The eight–element demonstration array should be measured in the anechoic chamber, and the array property analysis of the results should include a comparison with theoretical values, like those from CST Microwave Studio simulations.

### 3. RF Leakage Cancellation

The individual T/R modules are affected by RF leakage between the transmit and receive sides. The RF leakage consists of leakage in the circulator from port 2 into port 1 (see Figure 27) and of RF reflections due to mismatch between the  $50\ \Omega$  cables and the printed circuit dipole element, as apparent in Figure 57.

Some radar systems have a software solution to RF leakage. An analysis must be made in order to determine whether a coherent transmit subtraction can be used to improve the transmit/receive isolation. In this technique, a delayed replica of the transmit signal cancels leakage in the receiver.

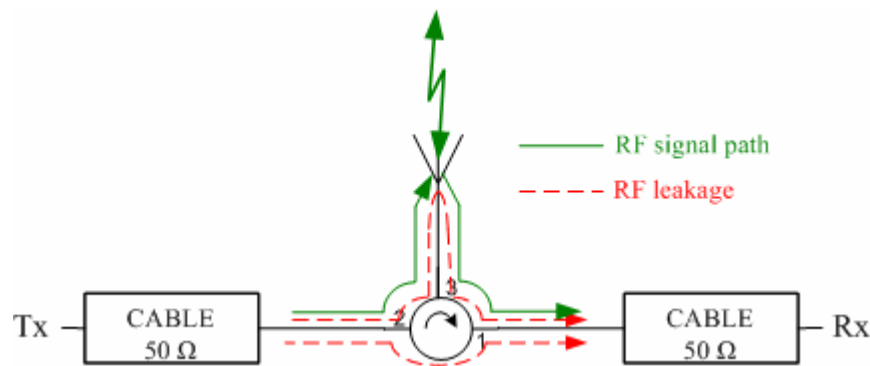


Figure 57. RF leakage contributions (dashed lines).

### 4. Wireless LO and Data Distribution

The demonstration array should be operated using a wirelessly distributed LO signal and must include a signal power level break-down and element synchronization. For the full-scale radar system, an analysis also covering the total data flow from the central control unit to the elements, channel interference and fading effects in a ship multipath environment should be conducted. Another task is to investigate software solutions that can be supplemented in LabVIEW to compensate LO synchronization for different path lengths in an array.

THIS PAGE INTENTIONALLY LEFT BLANK

## APPENDIX A. MATLAB SIMULATION PROGRAM

This appendix contains the MATLAB code that computes and plots the eight-element array pattern presented in Figure 52.

```
% Thesis Analysis - ANTENNA PATTERN
% Gert Burgstaller, August 2006

% Eight uniformly spaced Dipole Elements over a GROUND PLANE:
% * i.e., "a two-element sub-array" in y
% * Linear Array with UNIFORM SPACING & NON-UNIFORM AMPLITUDE in z
% * N = 2*M (an even number of elements
% * symmetric excitation around Array Center
clear all; close all; clc;

% FUNDAMENTALS
% =====
f=2.4e9;           % Frequency [Hz]
lambda=3e8/f;      % Wavelength [m]
k=2*pi/lambda;     % Wave Number
h=lambda/4;        % Dipole height over Ground Plane
resolution=1e4;    % No. plot points

% SCANNING ANGLES
% =====
phi=90;            % Pattern in y-z plane (i.e., no "elevation")
sin_ph=sin(phi*pi/180);
cos_ph=cos(phi*pi/180);

theta=linspace(0,pi,resolution);
theta_degr=theta*180/pi;
sin_th=sin(theta);
cos_th=cos(theta);

% DIPOLE ELEMENTS
% =====
ElemPatt=sqrt(1-sin_th.^2*cos_ph^2);

% IMAGING ("Two-Element Array" along y-axis, opposite sign, same phase)
% =====
AF_2=2*sin(k*h*sin_th*sin_ph);

% LINEAR ARRAY (Even Number Array along x-axis)
% =====
N=8;               % No. Antenna Elements
dz_lambda=0.52;    % Element Spacing along x-axis [wavelengths]
dz=lambda*dz_lambda;
ampl_coeff=[1 1 1 1]; % Element Ampl Coeff (here: max 8 elements)

% ALTERNATIVE 1: Desired (theoretical) Scan Angle [degr] input
beam_steer=0;
scan_th=beam_steer+90;
```

```

beta=-1.04*pi*cos(scan_th*pi/180);
beta_degr=beta*180/pi;

% ALTERNATIVE 2: Desired Incremental Phase Excitation [degr] input
%beta_degr=100;
%beta=beta_degr*pi/180; % [degr] --> [rad]

% Exponential Argument
psi=k*dz.*cos_th+beta;

% AF_N Summation
AF_N=zeros(1,resolution);
for m=1:N/2 % I.e., an even number
    AF_N=AF_N+2*ampl_coeff(m)*cos((2*m-1)/2.*psi);
end

% OVERALL ANTENNA PATTERN
% =====
AntPatt=ElemPatt.*AF_2.*AF_N;

abs_AntPatt=abs(AntPatt);
norm_AntPatt=abs_AntPatt/max(abs_AntPatt);

[maxvalue,index]=max(norm_AntPatt);
lobe_pos=theta_degr(index);
spacing=sprintf('%4.3f',dz_lambda);
incr_angle=sprintf('%4.1f',beta_degr);
position=sprintf('%4.1f',lobe_pos);
steering=sprintf('%4.1f',lobe_pos-90);

figure(1)
plot(theta_degr,norm_AntPatt);
grid;
xlabel('Scan Angle, \theta_s [\circ]')
ylabel('Normalized Antenna Pattern')
axis([0 180 0 1])
title(['N = ',num2str(N),', d_z = ',spacing,'\cdot\lambda, \beta = ',...
    incr_angle,'\circ, Lobe at ',position,'\circ',...
    ', Beam Steering Angle = ',steering,'\circ'])

break

figure(2)
polar(theta,norm_AntPatt)
title(['N = ',num2str(N),', d_z = ',spacing,'\cdot\lambda, \beta = ',...
    incr_angle,'\circ, Lobe at ',position,'\circ',...
    ', Beam Steering Angle = ',steering,'\circ'])

```



## LIST OF REFERENCES

- [1] Federation of American Scientists (fas.org), “National Missile Defense,” <http://www.fas.org/spp/starwars/program/nmd/>, last retrieved August 2006.
- [2] Monterey Herald (montereyheralds.com), “Missile Defense under Scrutiny,” <http://www.montereyherald.com/mld/montereyherald/news/nation/14999798.htm>, last retrieved August 2006.
- [3] The Library of Congress, (icreport.loc.gov), “Public Law 106–38-July 22, 1999,” [http://frwebgate.access.gpo.gov/cgi-bin/getdoc.cgi?dbname=106\\_cong\\_public\\_laws&docid=f:publ038.106.pdf](http://frwebgate.access.gpo.gov/cgi-bin/getdoc.cgi?dbname=106_cong_public_laws&docid=f:publ038.106.pdf), last retrieved August 2006.
- [4] Puttré, M and McKenna, T, “From the Ground Up,” *The Journal of Electronic Defense*, Vol. 28, No. 12, December 2005, pp. 40–47.
- [5] Air Force Link (af.mil), “PAVE PAWS Radar System fact sheet,” <http://www.af.mil/factsheets/factsheet.asp?fsID=168>, last retrieved August 2006.
- [6] Raytheon Products and Services (Raytheon.com), “AN/FPS-108 Cobra Dane Radar System,” [http://www.raytheon.com/products/cobra\\_dane/index.html](http://www.raytheon.com/products/cobra_dane/index.html), last retrieved August 2006.
- [7] Federation of American Scientists (fas.org), “AN/SPY-1 Radar,” <http://www.fas.org/man/dod-101/sys/ship/weaps/an-spy-1.htm>, last retrieved August 2006.
- [8] Navy Fleet Photo Gallery (navy.mil), “Ships Photo Gallery,” [http://www.navy.mil/view\\_gallery.asp?category\\_id=5](http://www.navy.mil/view_gallery.asp?category_id=5), last retrieved August 2006.
- [9] Program Executive Office — Ships (peoships.crane.navy.mil), “DDG 1000,” <http://peoships.crane.navy.mil/DDG1000/default.htm>, last retrieved August 2006.
- [10] Naval Technology (naval-technology.com), “Zumwalt DD(X) Class - Multimission Destroyer: Advanced Technology Surface Combatants, USA,” <http://www.naval-technology.com/projects/dd21/>, last retrieved August 2006.
- [11] Johnson, A. P., et al, “Ship Anti-Ballistic Response (SABR),” Master Thesis Technical Report, Wayne E. Meyer Institute of Systems Engineering, Naval Postgraduate School, June 2006.
- [12] Esswein, L. C., “Genetic algorithm design and testing of a random element 3-D 2.4 GHz phased array transmit antenna constructed of commercial RF microchips,” Master’s Thesis, Naval Postgraduate School, Monterey, California, June 2003.

- [13] Eng, C. S., "Digital antenna architectures using commercial off the shelf hardware," Master's Thesis, Naval Postgraduate School, Monterey, California, December 2003.
- [14] Ong, C. S., "Digital phased array architectures for radar and communications based on off-the-shelf wireless technologies," Master's Thesis, Naval Postgraduate School, Monterey, California, December 2004.
- [15] Ong, W., "Commercial off the shelf direct digital synthesizers for digital array radar," Master's Thesis, Naval Postgraduate School, Monterey, California, December 2005.
- [16] Tong, C. H., "System study and design of broad-band U-slot microstrip patch antennas for aperstructures and opportunistic arrays," Master's Thesis, Naval Postgraduate School, Monterey, California, December 2005.
- [17] Yong, Y. C., "Receive channel architecture and transmission system for digital array radar," Master's Thesis, Naval Postgraduate School, Monterey, California, December 2005.
- [18] Loke, Y., "Sensor synchronization, geolocation and wireless communication in a shipboard opportunistic array," Master's Thesis, Naval Postgraduate School, Monterey, California, March 2006.
- [19] Global Security.org, "AN/FPS-108 COBRA DANE," [http://www.globalsecurity.org/space/systems/cobra\\_dane.htm](http://www.globalsecurity.org/space/systems/cobra_dane.htm), last retrieved August 2006.
- [20] Jenn, D. C., Program review, "Update on Aperstructures, Opportunistic Arrays and Position Location Work," Naval Postgraduate School, July 2005 (unpublished).
- [21] Wai, C. C., "Distributed Beamforming in Wireless Sensor Networks," Master's Thesis, Naval Postgraduate School, Monterey, California, December 2004.
- [22] Sklar, B., *Digital Communications*, 2<sup>nd</sup> edition, Prentice Hall P T R, New Jersey, pp. 3–13, 2001.
- [23] Jenn, D. C., Program review, "Wirelessly networked opportunistic digital array radar," Naval Postgraduate School, January 2006 (unpublished).
- [24] Doan C. H., et al, "Design Considerations for 60 GHz CMOS Radios," *IEEE Communications Magazine*, pp. 132–140, December 2004.
- [25] University of Cambridge, "The INtelligent Airport (TINA)," <http://www.cl.cam.ac.uk/~jac22/talks/tina-overview.ppt>, last retrieved August 2006.

- [26] gow.EPSRC.ac.uk, "Engineering and Physical Sciences Research Council," <http://gow.epsrc.ac.uk/ViewGrant.aspx?GrantRef=EP/D076803/1>, last retrieved August 2006.
- [27] Coy, P. and Gross, N., "21 ideas for the 21st century," *Business Week*, Issue No. 3644, pp. 33–49, August 30, 1999.
- [28] Chong, C.-Y. and Kumar, S. P., "Sensor networks: evolution, opportunities and challenges," *Proceeding of the IEEE*, Vol. 91, No. 8, pp. 102–114, 2003.
- [29] National Instruments (ni.com), "CompactRIO," <http://www.ni.com/compactrio/>, last retrieved in August 2006.
- [30] National Instruments (ni.com), "LabVIEW: 20 Years of Innovation," [http://www.ni.com/labview/presskit\\_awards.htm](http://www.ni.com/labview/presskit_awards.htm), last retrieved in August 2006.
- [31] National Instruments (ni.com), "LabVIEW FPGA," <http://www.ni.com/fpga/>, last retrieved in August 2006.
- [32] National Instruments (ni.com), Data Sheet, "CompactRIO – Real-Time Embedded Controllers, NI cRIO–900x," [http://www.ni.com/pdf/products/us/6358\\_crio\\_rt\\_controllers.pdf](http://www.ni.com/pdf/products/us/6358_crio_rt_controllers.pdf), last retrieved in August 2006.
- [33] National Instruments (ni.com), Data Sheet, "CompactRIO Reconfigurable Chassis, NI cRIO–910x," [http://www.ni.com/pdf/products/us/cat\\_crio\\_9104.pdf](http://www.ni.com/pdf/products/us/cat_crio_9104.pdf), last retrieved in August 2006.
- [34] National Instruments (ni.com), Data Sheet, "C Series Analog Output Modules, NI–9263," [http://www.ni.com/pdf/products/us/c\\_series\\_ao.pdf](http://www.ni.com/pdf/products/us/c_series_ao.pdf), last retrieved in August 2006.
- [35] National Instruments (ni.com), Data Sheet, "C Series Analog Input Modules, NI–921x," [http://www.ni.com/pdf/products/us/c\\_series\\_ai.pdf](http://www.ni.com/pdf/products/us/c_series_ai.pdf), last retrieved in August 2006.
- [36] Analog Devices (analog.com), Data Sheet, "AD8346 - 2.5 GHz Direct Conversion Quadrature Modulator," <http://www.analog.com/en/prod/0%2C2877%2CAD8346%2C00.html>, last retrieved in August 2006.
- [37] Analog Devices (analog.com), Data Sheet revision A, "AD8346 0.8 GHz to 2.5 GHz Quadrature Modulator," [http://www.analog.com/UploadedFiles/Data\\_Sheets/240325465AD8346\\_a.pdf](http://www.analog.com/UploadedFiles/Data_Sheets/240325465AD8346_a.pdf), last retrieved in August 2006.

- [38] Analog Devices (analog.com), Data Sheet, “AD8346 Evaluation Board,” [http://www.analog.com/UploadedFiles/Evaluation\\_Boards/Tools/223525842AD8346EB.pdf](http://www.analog.com/UploadedFiles/Evaluation_Boards/Tools/223525842AD8346EB.pdf), last retrieved in August 2006.
- [39] Jenn, D. C., private discussions at NPS ECE Microwave Lab, July 2006.
- [40] RF Bay, Inc. (rfbayinc.com), Data Sheet, “LPA–4–14,” <http://rfbayinc.com/LPA/LPA-4-14.pdf>, last retrieved in August 2006.
- [41] DiTom Microwave Inc. (ditom.com), Data Sheet, “D3C2040 2.00 – 4.00 GHz SMA–Female Circulator,” <http://www.ditom.com/images/D3C2040.pdf?osCsid=969c6706edd78fde7250d0fea4033987>, last retrieved in August 2006.
- [42] Cheng, D. K., *Field and Wave Electromagnetics*, 2nd edition, pp. 449–471, Addison–Wesley, Reading, MA, 1992.
- [43] Naval Air Warfare Center (NAWC), EW and Radar Systems Engineering Handbook, “Voltage Standing Wave Ratio (VSWR) / Reflection Coefficient / Return Loss / Mismatch Loss,” <https://ewhdbks.mugu.navy.mil/VSWR.htm>, last retrieved in August 2006.
- [44] RF Bay, Inc. (rfbayinc.com), Data Sheet, “LNA–2700,” <http://rfbayinc.com/LNA/LNA-2700.pdf>, last retrieved in August 2006.
- [45] Analog Devices (analog.com), Data Sheet, “AD8347 0.8 GHz to 2.7 GHz Direct Conversion Quadrature Demodulator,” [http://www.analog.com/UploadedFiles/Data\\_Sheets/230407246AD8347\\_a.pdf](http://www.analog.com/UploadedFiles/Data_Sheets/230407246AD8347_a.pdf), last retrieved in August 2006.
- [46] Analog Devices (analog.com), Data Sheet, “AD8347 Evaluation Board,” [http://www.analog.com/UploadedFiles/Evaluation\\_Boards/Tools/471840006AD8347EB\\_0.pdf](http://www.analog.com/UploadedFiles/Evaluation_Boards/Tools/471840006AD8347EB_0.pdf), last retrieved in August 2006.
- [47] Gezer, B. L., “Multi–beam digital antenna for radar, communications, and UAV tracking based on off-the-shelf wireless technologies,” Master’s Thesis, Naval Postgraduate School, Monterey, California, September 2006.
- [48] Filtronic plc (filtronic.co.uk), Data Sheet, “Phase Shifter DC to 2, 4 and 8 GHz, Coaxial,” [http://www.filtronic.co.uk/pdf/phase\\_shifters/6X08.pdf](http://www.filtronic.co.uk/pdf/phase_shifters/6X08.pdf), last retrieved in August 2006.
- [49] Silver, J. P., “Gilbert Cell Mixer Design Tutorial,” [http://www.odysseus.nildram.co.uk/RFIC\\_Circuits\\_Files/MOS\\_Gilbert\\_Cell\\_Mixer.pdf](http://www.odysseus.nildram.co.uk/RFIC_Circuits_Files/MOS_Gilbert_Cell_Mixer.pdf), pp. 3–5, last retrieved in August 2006.

- [50] Z-Communications, Inc., Data Sheet, "V800ME10 Voltage Controlled Oscillator," Revision A1,  
<http://www.zcomm.com/PDFs/datasheets/V800ME10.pdf>, last retrieved in August 2006.
- [51] Z-Communications, Inc., "MINIEVAL, SMVEVAL and USSPEVAL Evaluation Boards," <http://www.zcomm.com/Products/Minieval.htm>, last retrieved in August 2006.
- [52] Balanis, C. A., "Arrays: Linear, Planar, and Circular" in *Antenna Theory – Analysis and Design*, pp.204-282, Harper & Row, Publishers, Inc., New York, 1982.
- [53] National Instruments (ni.com), "PXI," <http://www.ni.com/pxi/>, last retrieved in September 2006.
- [54] Erenoglu, B., "Naval Postgraduate School Anechoic Chamber Evaluation," Master's Thesis, Naval Postgraduate School, Monterey, California, September 2004.
- [55] Computer Simulation Technology (cst.com), "CST Microwave Studio ®," <http://www.cst.com/Content/Products/MWS/Overview.aspx>, last retrieved in September 2006.

THIS PAGE INTENTIONALLY LEFT BLANK

## INITIAL DISTRIBUTION LIST

1. Defense Technical Information Center  
Ft. Belvoir, Virginia
2. Dudley Knox Library  
Naval Postgraduate School  
Monterey, California
3. Chairman, Code EC  
Naval Postgraduate School  
Monterey, California
4. Mr. James King  
Office of Naval Research  
Arlington, Virginia
5. Mr. Steven Russell  
Office of Naval Research  
Arlington, Virginia
6. Prof. David Jenn  
Department of Electrical & Computer Engineering  
Naval Postgraduate School  
Monterey, California
7. Prof. Clark Robertson  
Department of Electrical & Computer Engineering  
Naval Postgraduate School  
Monterey, California
8. Prof. Richard Adler  
Department of Electrical & Computer Engineering  
Naval Postgraduate School  
Monterey, California
9. Prof. Michael Melich  
Wayne E. Meyer Institute of System Engineering  
Naval Postgraduate School  
Monterey, California
10. Prof. Rodney Johnson  
Wayne E. Meyer Institute of System Engineering  
Naval Postgraduate School  
Monterey, California

11. Prof. Bill Solitario  
Wayne E. Meyer Institute of System Engineering  
Naval Postgraduate School  
Monterey, California
12. Mr. Eng Choon Yeo, Code PH533  
Naval Postgraduate School  
Monterey, California
13. LT Martin Holguin, Code EC590  
Naval Postgraduate School  
Monterey, California
14. CDR Gert Burgstaller  
Swedish Joint Forces Head Quarters  
Stockholm, Sweden